Design, Characterisation and Optimisation of a SAW Correlator Driven, Wireless, Passive Microvalve For Biomedical Applications

by

AJAY CHANDRA TIKKA

Master of Engineering,
RMIT University, Australia 2004.

Thesis submitted for the degree of

Doctor of Philosophy

in

School of Electrical and Electronic Engineering
The University of Adelaide, Australia

October, 2009

Contents

Abstract

The culmination of rapid advances made in the areas of microelectromechanical systems (MEMS), nonregenerative power sources, nanotechnology, and biomedical engineering have resulted in the expansion of their horizons in modern medicine for the deployment of a wide array of implantable devices. However, the lifetime and remote interrogability of implants, specifically used for drug delivery applications, has been an issue of contention, as their deployment period is limited by the battery life and the device size. Furthermore, not much research effort is directed towards remotely controlled flow manipulation using passive components. These shortcomings are addressed in this thesis by employing surface acoustic wave (SAW) technology to design a novel RF powered, secure coded, active microvalve with fully passive components. By combining the complex signal processing capabilities of the acoustic wave correlator with the electrostatic actuation of the microchannel, the advantages of both the mechanisms are incorporated into a novel microvalve design. Fluid pumping can be achieved at ultrasonic frequencies by electrostatically actuating the edge clamped microchannel, placed in between the compressor interdigital transducer's (IDT's) of two identical SAW correlators. The ability to wirelessly administer doses of drug accurately, for an extended period of time, at an inaccessible target location, through an implanted microvalve has the potential to revolutionise health care for long-term, controlled drug release applications.

Three specific and diverse areas within MEMS, the new device builds on, are investigated by taking a comprehensive design, modelling, optimisation and experimental validation approach for majority of the research endeavors in the thesis. The first area corresponds to SAW technology followed by microfluidics, and body-centric communications; driven by the ultimate goal to demonstrate the operational feasibility of a human implanted, wirelessly controlled microvalve. The proposed specialised design necessitated a thorough understanding of the multiple coupled physics phenomena at the process level, before fabrication, for the critical investigation and refinement of the individual microvalve components. A comprehensive finite element modelling technique, where the complete set of partial differential equations are solved, was used to design these microvalve components with low level of abstraction to enable an automatic inclusion of the majority of the second order effects.

As a starting point for the FEM modelling of SAW devices, an infinite periodic grating was modelled to analyse the freely propagating eigenmodes and eigenvalues with modal analysis; and electrically active waves and electrical admittance with harmonic analysis. A curve fitting technique was employed to extract the COM/P-matrix model parameters from these FEM results. Furthermore, an experimental validation of the parameters extracted using this novel combination of FEM and fitting techniques was carried out by fabricating a number of delaylines and comparing the physical structure response with the formulated P-matrix model. On the other hand, the modelling of a 2 and 3-dimensional, 5×2-bit Barker sequence encoded acoustic wave correlator was demonstrated using FEM. The correlator's response was quantified in terms of harmonic analysis, to obtain the electrical admittance and output voltage profile, and transient analysis, to study the acoustic wave propagating characteristics and correlation pulses. The validation of these simulation results was carried out by fabricating the SAW correlators using optical lithographic techniques. A good agreement between the numerical and experimental results highlighted the feasibility and potential of using FEM for application specific modelling of SAW correlators.

The complexity involved in combining the electroacoustic correlation and electrostatic actuation mechanisms, necessitated a systematic design and optimization of the novel microvalve which is best possible with FEM. In this thesis, the emphasis was on the design and optimisation of a novel microfluidic structure through the deflection analysis, both, to verify the functionality of the concept and to investigate the working range of the structure. Secure interrogability of the microvalve was demonstrated by utilising finite element modelling of the complete structure and the quantitative deduction of the code dependent, harmonic and dynamic transient microchannel actuation. A numerical and experimental analysis of the biotelemetry link for the microvalve was undertaken in the vicinity of numerical and physical human body phantoms, respectively. To accurately account for the path losses and to address the design optimisation, the receiver coil/antenna was solved simultaneously with the transmitter coil/antenna in the presence of a human body simulant using 3-dimensional, high frequency electromagnetic, FEM modelling. The received relative signal strength was numerically and experimentally derived for a miniature (6×6×0.5 mm), square spiral antenna/coil when interrogated by a hand-held 8×5×0.2 cm square spiral antenna/coil in the near field. Finally, the experimental results confirmed well with the FEM analysis predictions and hence ascertained the applicability of the developed system for secure interrogation and remote powering of the newly proposed microvalve.

Statement of Originality

Name: Ajay Chandra Tikka Program: Doctor of Philosophy (PhD)

This work contains no material which has been accepted for the award of any degree or diploma in any university or other tertiary institution and, to the best of my knowledge and belief, contains no material previously published or written by another person, except where due reference has been made in the text.

I give consent to this copy my thesis, when deposited in the University Library, being made available for loan and photocopying, subject to the provisions of the Copyright Act 1968.

I also give permission for the digital version of my thesis to be made available on the web, via the University's digital research repository, the Library catalogue, the Australasian Digital Theses Program (ADTP) and also through web search engines, unless permission has been granted by the University to restrict access for a period of time.

26th October, 2009

Signed **Date**

This page is blank

Acknowledgments

As I ponder over my research endeavors for the past 3.5 years, it does not take much time to realise that this dissertation materialised mainly due to the guidance and support of numerous individuals.

First and foremost, I would like to thank my supervisor Dr. Said Al-Sarawi for reposing trust in me, introducing me to various multi-disciplinary projects, willingness to discuss everything under the sun, and being a bedrock of support and assurance. I am indebted to you for tirelessly reviewing all our publications including this thesis. It has been an honor and a pleasure working with you. I express my gratitude to my co-supervisor Professor Derek Abbott for his unwavering support and guidance. You never cease to amaze me with your unbound energy and omnipresent capabilities!

I gratefully acknowledge the funding agency Australian Research Council (ARC) Discovery for the generous grant which facilitated this research. Furthermore, I extend my sincere thankfulness to Dr. Igor Switala and his team from the Defence Science and Technology Organisation (DSTO), for the useful discussions and assistance with the fabrication of SAW devices and miniature antennas. Your abundant enthusiasm and patience have made an immense difference. I would also like to thank Mr. Leonard Green from Adelaide Microscopy for his support with microanalysis of the structures. I had the privilege of holding several discussions and later visiting Professor Vijay K. Varadan (University of Arkansas, USA). I hold him in the highest esteem for inspiring me with his vision for smart structures and emerging technologies.

I would like to express my appreciation for all the fellow researchers at the University of Adelaide for creating a conducive environment. In particular, Don for your friendship and support in both good times and hard times. It would have been a rough ride without you. Ben and Akhilesh for the useful discussions and assistance with setting up the test equipment.

Lastly, I would like to thank my family for always being there: Mom and Dad for their unconditional love and support and Vinay, my brother, for encouraging me to pursue a PhD. Thank you all!

This page is blank

Abbreviations and Symbols

Abbreviations

AC	**A**lternating **C**urrent
BAW	**B**ulk **A**coustic **W**ave
BEM	**B**oundary **E**lement **M**ethod
BPSK	**B**inary **P**hase **S**hift **K**eying
COM	**C**oupling **O**f **M**odes
DC	**D**irect **C**urrent
DIL	**D**ual **I**n **L**ine
DOF	**D**egress **O**f **F**reedom
EM	**E**lectro**m**agnetic
FDS	**F**requency **D**omain **S**ampling
FDTD	**F**inite **D**ifference **T**ime **D**omain
FEM	**F**inite **E**lement **M**ethod
FM	**F**requency **M**odulation
HFEM	**H**ybrid **F**inite **E**lement **M**ethod
IDT	**I**nter**d**igital **T**ransducer
LSAW	**L**eaky **S**urface **A**coustic **W**ave
MEMS	**M**icro**e**lectro**m**echanical **S**ystems
MLS	**M**aximum **L**ength **S**equence
MR	**M**etallization **R**atio
PBC	**P**eriodic **B**oundary **C**ondition
Q-factor	**Q**uality **F**actor
RF	**R**adio **F**requency
RFID	**R**adio **F**requency **Id**entification
RTO	**R**emote **T**urn **O**n
SAW	**S**urface **A**coustic **W**ave
SDA	**S**pectral **D**omain **A**nalysis
SEM	**S**canning **E**lectron **M**icroscope
STW	**S**urface **T**ransverse **W**ave
TDS	**T**ime **D**omain **S**ampling
UV	**U**ltra **V**iolet

Symbol	Name	Unit
$\mathbf{a}$	displacement vector	m
A	delayline admittance matrix	mixed
A_0	overlapping area	m^2
B	bandwidth	Hz
$B(f)$	susceptance	S
c	loaded wavenumber	rad/m
c	stiffness	N/m^2
C	capacitance	F
C_n	normalised capacitance	F
C_p	periodic capacitance	F
D	electrical flux	C/m^2
DR_o	dispersion relation for open circuit grating	-
DR_s	dispersion relation for short circuit grating	-
d	distance	m
E	electric field	V/m
E_c	electromechanical coupling energy	J
E_k	electric field vector	V/m
e	piezoelectric stress constant	C/m^2
F	force	N
F_E	electrostatic force	N
F^E	nodal electrostatic force	N
F_N	noise figure	dB
$\mathbf{F}^N$	nodal force vector	N
$\mathbf{F}^{TH}$	thermal force vector	N
f_c	center frequency	Hz
f_B	bit rate	Hz
f_{M+}	anti-symmetric SAW modal frequency	Hz
f_{M-}	symmetric SAW modal frequency	Hz
G	gain	-
$G(x)$	Green's function	mixed
$G(f)$	conductance	S
$G(f)$	transfer function	mixed
$[G]$	strain-displacement matrix	mixed
g	spacing between coil turns	m
H	magnetic field strength	A/m

Symbol	Name	Unit
I	current	A
$[I]$	identity matrix	-
j	unit imaginary number	-
K	Boltzmann's constant	-
$[K]$	structural stiffness matrix	mixed
$[K_d]$	dielectric permittivity matrix	mixed
L	IDT length	m
L	inductance	H
L_{eff}	effective inductance	H
l_{avg}	average diameter of the square spiral	m
l_{tot}	total length of the square spiral	m
M	mutual inductance	H
$[M]$	mass matrix	mixed
$[N]$	structural shape function	mixed
$[N_E]$	electrical shape function	mixed
N_B	binary bits	-
n	normalised wavenumber	-
n	number of coil turns	-
P	power	W
$P(f)$	P-matrix	mixed
p	period of the grating	m
p_a	radiation pressure	Pa
Q	quality factor	-
q	complex charge of the electrodes	C
q_n	nodal charge density	C/m
R	resistance	Ω
$\mathbf{R_s}$	residual vector of elastostatic field	-
$\mathbf{R_e}$	residual vector of electromechanic field	-
S	strain	-
S_{12}	insertion loss	dB
S_{P}	power density	W/m^2
SNR	signal-to-noise ratio	-
T	stress	N/m^2
T_C	temperature	°C
T_B	bit time	sec

Symbol	Name	Unit
t_s	substrate thickness	m
u	particle displacement	m
V	voltage	V
v_i	nodal electrical potential	V
W	width of the coil	m
Y	admittance	S
Z	impedance	Ω
ω	angular frequency	rads^{-1}
μ	propagation constant	-
μ_0	permeability of vacuum	Vs/Am
λ	wave length	m
λ_t	wave length in lossy medium	m
ν	Velocity	m/s
δ	normalised COM wavenumber	-
κ	COM reflection	-
γ	COM attenuation parameter	Nep/m
α	COM transduction parameter	$\Omega^{-1/2}\mathrm{m}^{-1}$
ϵ	permittivity	F/m
ϵ_r	relative dielectric constant	-
ϵ_t	complex permittivity	F/m
ρ	mass density	$\mathrm{kg/m}^3$
ϕ	electrical scalar potential	V
σ	conductivity	$\mathrm{S/m}^2$
∇	gradient of a scalar field	m^{-1}
$\nabla.$	divergence of a vector field	m^{-1}
Θ_D	diffraction angle	-
σ^M	Maxwell stress vector	$\mathrm{N/m}^2$
δ_p	penetration depth	m
æ	fill ratio	-
δ_c	skin depth	m

Publications

Book Chapter Publications

1. TIKKA-A., AL-SARAWI-S., AND ABBOTT-D. (2009). Loading analysis of a remotely interrogatable passive microvalve, *Recent Advances in Sensing Technology - Lecture notes in Electrical Engineering Series*, Springer-Verlag, Accepted for Publication.

Journal Publications

2. TIKKA-A., AL-SARAWI-S., AND ABBOTT-D. (2008). Modelling a surface acoustic wave based remotely actuated microvalve, *Smart Materials & Structures*, 18, p. 045014.

3. TIKKA-A., AL-SARAWI-S., AND ABBOTT-D. (2008). Acoustic wave parameter extraction with application to delay line modelling using finite element analysis, *Sensors and Transducer Journal*, 95(8), pp. 26-39.

Referred Conference Publications (full paper)

4. TIKKA-A., AL-SARAWI-S., AND ABBOTT-D. (2009). Contactless energy transfer for a SAW based implanted microvalve, *Proc. of IEEE Regional Symposium on Micro and Nano Electronics*, pp. 513-517.

5. TIKKA-A., AL-SARAWI-S., AND ABBOTT-D. (2008). Wireless telemetry system for a SAW based microvalve, *Proc. of SPIE Biomedical Applications of Micro- and Nanoengineering IV Conference*, Vol. 7270, p. 727018.

6. TIKKA-A., AL-SARAWI-S., AND ABBOTT-D. (2008). A remotely interrogatable passive microactuator using SAW correlation, *Proc. of 3rd International Conference on Sensing Technology*, pp. 46-51.

7. TIKKA-A., AL-SARAWI-S., AND ABBOTT-D. (2008). Finite element analysis of a 3-dimensional acoustic wave correlator response for variable acoustic modes, *Proc. of SPIE Modeling, Signal Processing, and Control for Smart Structures Conference 2008*, Vol. 6926, p. 692603.

8. TIKKA-A., AL-SARAWI-S., AND ABBOTT-D. (2007). Finite element modelling of SAW correlator, *Proc. of SPIE BioMEMS and Nanotechnology III Conference*, Vol. 6799, p. 679915.

9. TIKKA-A., AL-SARAWI-S., AND ABBOTT-D. (2007). SAW parameter extraction using finite element analysis, *Proc. of 2nd International Conference on Sensing Technology*, pp. 393-398.

10. TIKKA-A., AL-SARAWI-S., ABBOTT-D., WONG-M., AND SCHUTZ-J. (2006). Improving the security and actuation of wireless controlled microvalve, *Proc. of SPIE Smart Structures, Devices, and Systems Conference*, Vol. 6414, p. 64130D.

11. DISSANAYAKE-D., TIKKA-A., AL-SARAWI-S., AND ABBOTT-D. (2006). A radio frequency controlled microvalve for biomedical applications, *Proc. of SPIE Smart Materials IV Conference*, Vol. 6413, p. 64140U.

Referred Conference Publications (abstract)

12. DISSANAYAKE-D., TIKKA-A., AND AL-SARAWI-S. (2006). Use of ANSYS in design and analysis of piezoelectrically actuated microvalves for biomedical applications, *Proc. of ANSYS Australasian User Conference*.

13. DISSANAYAKE-D., TIKKA-A., AND AL-SARAWI-S. (2006). Biomedical applications of a wireless controlled microvalve, *Proc. of The Australian Health and Medical Research Congress*, Abs. 1059.

List of Figures

This page is blank

List of Tables

This page is blank

Chapter 1

Introduction

The current thesis is devoted to MEMS engineering research with application to novel microfluidic devices. The motivation for the research, including a brief review of conventional microvalves and wireless SAW technology is outlined in Section 1.1. The research objectives are described in Section 1.2. Section 1.3 highlights the research undertaken to address the objectives, and the resulting specific research contributions of the author. Finally, a description of the thesis structure is provided in Section 1.4.

1.1 Motivation

Miniaturisation appears to be the buzzword that is driving modern innovations. The advent of microscale fabrication techniques, from the mid of the past century, have heralded a new era of devices in the semiconductor industry. As a result, the earlier perception of bigger the system the better its performance, has been put to rest. The unrelenting quest to make devices smaller without compromising their performance is driven by both the market demand and the lure of opening up novel applications. This has led to the adaptation of miniaturisation techniques to multiphysics areas such as sensors and actuators. As the size of the system is independent of it's data gathering and information processing efficiency, microsensors have attained a high level of maturity and market penetration over the past few decades. However, the same could not be professed about the microactuator development. This can be attributed to the complex and expensive fabrication processes involved and the predominance of the second order effects, such as stiction, electro-osmosis, electrophoresis, streaming potential, and dielectrophoresis, due to the increased surface-to-volume ratio, in the micro scale (Thielicke and Obermeier 2000, Haraldsson 2005, Liu and Bar-Cohen 1999). These second order effects invalidate the straightforward applicability of many multiphysics principles used in the macro scale designs. Microfluidic devices are an extension of microactuators which, mostly, employ one of these

secondary effects or the standard actuation techniques for fluid manipulation in the range of picoliters to microliters. The general advantages offered by the microfludic devices, without indulging in application specificity, are improved throughput of samples, reduced power consumption, increased sensitivity, portability, and lower analysis costs (Gravesen *et al.* 1993, de Jong *et al.* 2006). All these advantages come at the expense of high manufacturing costs and the lack of a generic design approach.

In recent times extensive research and development efforts are globally directed towards fluid diagnostics and flow manipulation by adopting advances made in other expansive fields such as MEMS, micromachining and material sciences. Novel miniature microfluidic pumps, valves, mixers and controllers have reached a level of sophistication to make deep inroads into both civilian and military markets (Nguyen and Wereley 2002). As per market studies, the microfluidic component market is projected to reach $4.2 billion by 2014 (Micro fluid management technology - Yole development). It is also reported that the trend towards function integration would drive the demand for the next generation of microfluidic applications such as portable medical devices, micro fuel cells, and micro chemical reactors (Whitesides 2006). As a step in that direction, the development of novel and innovative microvalves has witnessed a rapid growth in the recent times. Most of the research in this area, as will be discussed in detail in the latter part of this section, is focused on developing novel structures through the optimisation of the existing design specifications by targeting features such as flow rate, leakage flow, power consumption, response time and disposability. However, the constant expansion of the application domain of these devices into fields as diverse as life sciences and chemistry applications is placing new demands on the existing models. One among these new design requirements is the remote interrogability of the microfluidic devices. The capability to wirelessly control fluid flow can emerge as an attractive technology enabling various biomedical applications. Furthermore, most of the existing microfluidic devices in biomedical implants are either battery powered or have external pump modules that are connected to a patient by means of a passive port (Gomez 2008, Cao *et al.* 2000, Geipel *et al.* 2006). The use of a battery would place additional constraints on the device size and would require an electronic circuitry module. Hence, the development of an active microvalve with fully passive components, enabling wireless control of fluid flows, is a key task in the realization of compact high performance biomedical implants. Numerical applications can be envisaged as such a device is light, reliable, chemically stable, enables high patient mobility, and not limited by the lifetime of the battery. In addition to eliminating the degradation of the drug,

because of its interaction with body's various defence systems, such a device would provide a freely programmable, time-modulated, controlled-release formulation to ensure patient safety and comfort in long-term treatment. For example, diabetes, which is a major cause of vascular diseases in the developed world, necessitates a mechanism to stabilise the fluctuations in the glucose levels through controlled and sustained *in vivo* dosing of insulin. A device, such as the proposed microvalve, has the capability to revolutionise the treatment of such a disease.

Surface Acoustic Wave (SAW) devices, apart from being inherently rugged and reliable, can provide bi-phase coding and processing gain by varying the electrodes geometry (Ostermayer 2001, Malocha *et al.* 2004, Moeller *et al.* 1999). Thus, SAW devices can be used as wirelessly interrogatable and completely passive devices. However, the aspect of employing SAW technology for wireless powering of actuators in a secure manner has not been investigated. The use of SAW technology for such applications has the potential to open up many new possibilities. The main advantage is that SAW devices, being inherently passive and robust, are not severely impacted by possible hostile conditions. Furthermore, with the ability to wirelessly power and control these devices they can be placed in remote locations. Hence, the concept of using electoacoustic correlation for secure actuation of the wirelessly controlled microvalve needs a thorough investigation, which is the cornerstone of this thesis. To achieve this objective, an analysis of the current status of microvalves and wireless SAW devices is mandatory, and hence will be outlined in the rest of this section.

1.1.1 Conventional Microvalves

Microvalves can be classified into two broad categories namely active and passive. While the the fluid flow in passive microvalves is controlled by the fluid pressure, the active microvalves are triggered by an external signal irrespective of the fluid dynamics. Active microvalves have emerged as the predominant form of microfluidic components currently being employed for a wide array of applications ranging from on/off switching to fluid flow control and isolation (Oh and Ahn 2006, Nguyen *et al.* 2002). Innovations in this area are normally aimed at developing novel devices with optimising characteristics such as valve closing dynamics, response time, power consumption, leakage, flow resistance and reusability (Felton 2003). The four general application domains of the microvalves are outlined in the Table. 1.1. All four domains contain devices featuring active components and passive components. The device specifications

Table 1.1. Current application domains of microvalves.

Field	Specifications	Literature
Consumer electronics	small form factor, high flow rate, short response time.	Messner *et al.* (2006) Yobas *et al.* (2003)
Biomedical	high reliability, low heat generation, controlled flow rate, low leakage, tight material & geometric constraints.	Goettsche *et al.* (2005) Reynaerts *et al.* (1997)
Chemical analysis	chemically tolerant, controlled flow rate, high particle tolerance, short response time.	Oh *et al.* (2005) Ohori *et al.* (1998)
Aerospace	high pressure, low power, thermally insensitive, low leakage, limited susceptibility to vibration & radiation.	Yang *et al.* (2004) Chakraborty *et al.* (2000)

described in Table. 1.1 is not an attempt by the author to strictly narrow down the device characteristics for each domain, but rather to group features that are generally common for the corresponding domain.

A further categorisation of the microvalves can be carried out based on the actuation principle they employ. The commonly used actuation mechanisms, as shown in Table. 1.2, are: piezoelectric, electrostatic, electromagnetic, bimetallic, thermopneumatic, shape memory alloy and hydrogel. The choice of an actuation technique is determined by the advantages offered by the individual actuation principle for the target application and the ease of integrating a miniature actuator with the microvalve components. A comprehensive review of microvalves, their actuation techniques, and microactuators was carried out by Oh and Ahn (2006), Hesketh *et al.* (2003), and Thielicke

Table 1.2. Microvalve actuation principles.

Actuation principle	Advantages	Literature
Piezoelectric	large force, fast response time.	Zhao *et al.* (2005) Roberts *et al.* (2003)
Electrostatic	ease of miniaturisation, very fast response time.	Van der Wijngaart *et al.* (2002) Bae *et al.* (2007)
Electromagnetic	large displacement, good reliability.	Sutanto *et al.* (2006) Fu *et al.* (2003)
Thermal (bimetallic)	simple design, large force.	Barth (1995) DeVoe (2002)
Thermopneumatic	large displacement, high versatility.	Henning (2006) Rich and Wise (2003)
Shape Memory Alloy (SMA)	large force, geometric flexibility.	Piccini and Towe (2006) Kohl *et al.* (2000)
Hydrogel	low cost, energy scavenging ability.	Baldi *et al.* (2006) Eddington and Beebe (2004)

and Obermeier (2000), respectively. Of all the actuation mechanisms outlined in Table. 1.2, electrostatic actuation is the most frequently applied method for microfluidic devices. Electrostatic actuators utilise the induced forces between closely placed conducting plates/electrodes that are energised by different potentials. In addition to relying on a simple and versatile technology, the electrostatic actuators offer the benefits of fast response time, low power consumption, ease of integration, compatibility with other fabrication technologies and independency on the ambient temperature (Batra *et al.* 2007, Sounart *et al.* 2005).

The crucial choice of actuation mechanism for microvalves is normally guided by the design specifications. In recent years, there is an increased focus on the development of design methodologies and optimisation methods for smart structures using hybrid techniques (Frecker 2003). By combining two or more actuation principles, the specific design considerations of microstructures can be addressed. Hybrid actuators combining two or more acutation principles such as piezoelectric-magnetic, pyroelectric-piezoelectric, thermal-electrostatic, and electromagnetic-electrostatic have been reported in the literature (Fu 2005, Duggirala and Lal 2005, Robert *et al.* 2003, Bosch *et al.* 1993). The design of a normally closed, remotely actuated, secure coded, batteryless, active microvalve using fully passive components cannot be carried out

with any of the actuation mechanisms given in Table. 1.2. This is because, given the variety of actuation techniques that have been analysed for microvalves, the requirements for secure coding and complete passivity cannot be met by employing just one of them. Even though electrostatic actuation appears to be a suitable actuation principle, it falls short in addressing the wireless powering and secure coding requirements. These drawbacks are addressed in this research by combining the complex signal processing capabilities of acoustic wave correlator with the electrostatic actuation of the microchannel. This synergetic approach incorporates the advantages of both the mechanisms into the microvalve design.

1.1.2 Wireless SAW Technology

SAW devices have expanded into a multitude of products and applications in fields as diverse as microelectromechanical systems (MEMS), telecommunications, chemical sensing, and biotechnology (Mamishev *et al.* 2004, Hashimoto 2000, Springer *et al.* 1999). Acoustic wave devices are so called because they use acoustic or mechanical waves for signal processing. Surface acoustic wave devices are not only small, rugged and reliable; they can also be used for wirelessly interrogable and completely passive devices for many hostile environments. Since the acoustic energy is confined to near the surface of the solid, the wave can be tapped or modified while it is propagating (Reindl *et al.* 1998). SAW filters and sensors have been widely researched over the past few decades as they offer many advantages including reliability, high filter selectivity, robustness, wireless, passive operation, efficient, low cost, and ease of large-volume production. Furthermore, the SAW devices do not require any DC power and there is no junction voltage to overcome as in radio frequency identification (RFID) tags and semiconductor electronics. The senors are being used for measuring physical, chemical and biological quantities in harsh environments, whereas the filters are predominantly being utilised in consumer electronics such as mobile phones and televisions. While the development of SAW sensors is driven by the ever increasing demand for environmental monitoring, the SAW filters development is driven by the explosive evolution of the telecommunication industry.

Surface acoustic waves are generated and detected on the free surface of a piezoelectric material with the help of a series of interwoven, metallic comb structures called IDTs (interdigital transducers). An application of a time varying voltage to an IDT, as shown in Fig. 1.1, generates the acoustic wave on the input side due to inverse piezoelectric

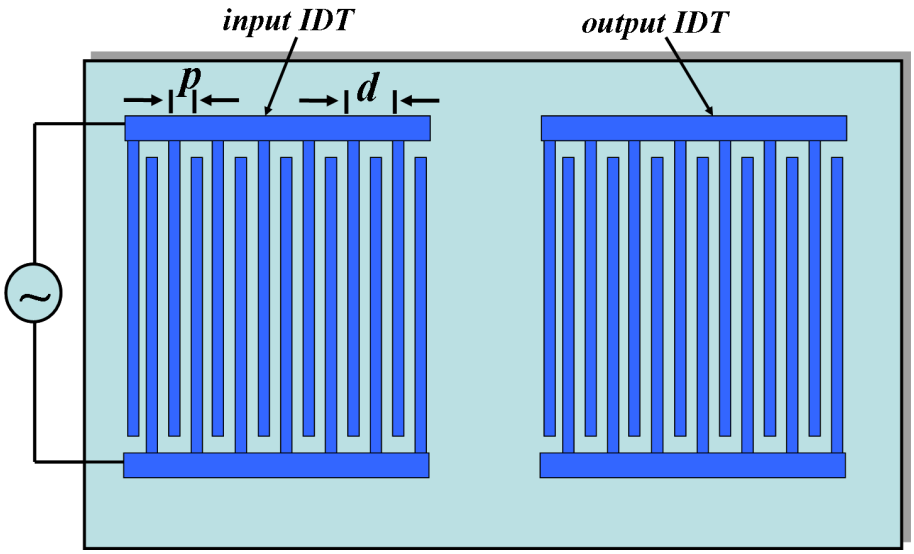

Figure 1.1. A two-port SAW delayline with an input and output IDT.

effect. In the basic configuration there is an input IDT and an output IDT. The acoustic wave generated by the input IDT travels through the space called the delay region, or sensing region for sensors, and reaches the output IDT. The mechanical displacements due to the acoustic waves create a voltage difference between the output IDT fingers due to piezoelectric effect. The operation of the device relies on a full constructive interference of the surface acoustic waves. This is achieved by ensuring the spacing between alternating electrodes, d, is equal to the surface acoustic wavelength λ ($\lambda = v/f$) and periodicity of the electrodes p is equal to $\lambda/2$ (Campbell 1998, Drafts 2001). Here, v is the SAW velocity (m/s) and f is the frequency (Hz) of the incoming electromagnetic wave. A SAW device has the potential to be an ideal remote turn on (RTO) component. Given a controlled set of communication conditions, a SAW device enables RF energy to be converted to electrical energy. The overall efficiency of the RTO system is determined by the energy conversion efficiency of the RF signal into an electrical signal.

Interrogation systems for measuring changes in either amplitude, frequency or phase as a function of input stimuli are widely employed for wireless SAW sensors and identification tags. A comprehensive review of measurement systems including measuring parameters, radio frequency (RF) interrogation using time domain sampling (TDS) and frequency domain sampling (FDS) has been provided by Pohl (2000). Furthermore, Gardner *et al.* (2001) have given a detailed description of the three electronic

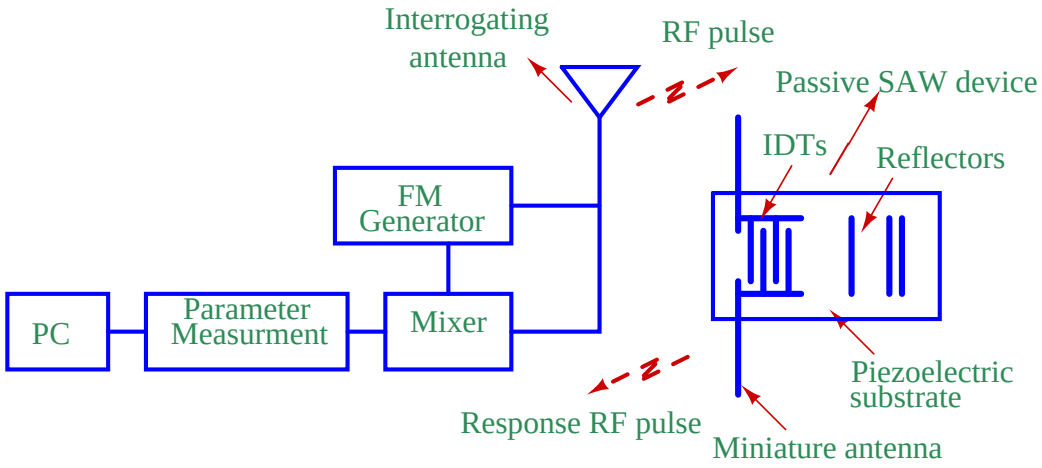

Figure 1.2. Schematic diagram of a wireless interface between the interrogating system and a passive SAW device (Gardner *et al.* 2001) (Note: Figure not to scale).

configurations for measuring the three parameters, including the network analyser setup and calibration. Based on these advances, radio interrogatable passive SAW devices have attained a wide spread acceptance as tags for automobile identification, and sensors for humidity, temperature, pressure, acceleration, magnetic field, electric current, and torque measurement (Scholl *et al.* 2003, Stelzer *et al.* 2008).

A schematic diagram, employed by Gardner *et al.* (2001), to describe the basic operating principle of SAW sensors with a wireless communication interface is depicted in Fig. 1.2. It is based on the principle that the targeted sensing quantity varies the travelling time of the acoustic waves between the IDT and the reflectors. Here, the output IDT has been be replaced by reflectors with unique bar code for multiple access applications. The interrogating electromagnetic waves at the transmitter section are generated with the help of a transmitter antenna connected to a frequency modulated (FM) signal generator. The IDT of the passive SAW sensor is directly connected to an antenna. Here, the electromagnetic waves transmitted by the interrogating unit are transduced by the IDT into SAWs and vice-versa. The SAWs propagates on the surface of the piezoelectric crystal, toward the reflectors. The reflectors reflect back part of the incoming wave towards the IDT as echoes, that are characterised by the the SAW velocity and IDT-reflector spacing dependent delay times. These echoes are transduced back to electromagnetic waves by the IDT-antenna pair, and picked up by the transmitter antenna at the interrogating unit. The differentiation between the transmitted and received signal is carried out with the help of a mixer and the changes in delay times of the echo signals is analysed by employing spectrum analysis techniques.

Thus, the interrogation unit evaluates changes in the amplitude, frequency, and time of the received signal and hence determines the identification number or the sensor value (Reindl *et al.* 1998, Stelzer *et al.* 2004). This approach has low interference effect as all environmental echoes are attenuated by the time the signals corresponding to SAW echoes reach the interrogation unit, due to the low velocity of SAWs.

The application domain of one type of SAW filters, the SAW correlators, is not as wide as the other embodiments such as delay lines and resonator-based filters. This could be attributed to the lack of accurate fabrication techniques required for the mass production of these devices operating at GHz frequencies. Moreover, the programmability of the SAW correlators is arduous due to the predetermination of the code in the manufacturing stage and hence do not lend themselves for commercial acceptance. However, these drawbacks have be addressed recently with the advent of piezoelectric substrates with high electromechanical coupling coefficients, advanced lithographic techniques and programmable SAW correlators (Brocato *et al.* 2003, Kosinski 2000). The use of SAW technology in general and correlation in particular bestows several benefits to the microvalve structure. Microvalves are often powered by small batteries. If the microvalve is placed in a remotely inaccessible location, the life time of a battery supplied device becomes critical. In that case, the wireless microvalve can be powered by using techniques similar to ones commonly used in RFID technology (Finkenzeller 2003), where low power circuits can obtain their power from an electromagnetic field. The contributions of SAW filter technology include small size, passivity, low cost, reliability, robustness, compact packaging, relatively stable performance over temperatures, ease of device fabrication for both low and high volume production. Furthermore, the use of SAW correlation provides remote discrete code addressability, low loss and sharp signal suppression from resonance to rejection band (high Q-factor).

1.2 Objectives

Most of the human implantable MEMS devices which are as diverse as pacemakers, retinal and cochlear implants, physiological recording devices, muscle stimulaters, and drug delivery devices (Mokwa 2007, Loizou 1999, Mercanzini *et al.* 2005, Russold and

Jarvis 2007), employ nonregenerative power sources; i.e they are powered through batteries or impeded power sources, thus restricting their mobility, compactness and lifespan (Li *et al.* 2007a, Grayson *et al.* 2004, Amer and Badawy 2005, Geipel *et al.* 2007, Cook-Chennault *et al.* 2008). Furthermore, not much research effort is directed towards remotely controlled flow manipulation using passive components. Such a technology has the potential to pave way for the next generation of microfluidic devices, and hence is the research area of interest in this thesis. The possible applications of a remote controlled, fully passive microvalve are boundless, especially for drug delivery applications in the biomedical domain. The ability to wirelessly administer accurate doses of drug, for an extended period of time, at an inaccessible target location, through an implanted microvalve can revolutionise the way diseases such as cancer and diabetes are treated. The current thesis summaries the work towards a RF powered, secure coded, SAW correlator driven, passive microvalve. The need to optimise and verify individual components of the microvalve in order to achieve the desired performance of the integrated assembled system is clearly evident. Hence, the research objectives are:

- As the design of the wireless, passive microvalve using SAW technology represents a fundamental departure from the conventional approach of using active circuitry for signal processing, it demands a thorough analysis of existing SAW device modelling techniques, both to optimise the design and reduce the reliance on fabricated test structures.

- It is necessary to employ a versatile modelling technique where the piezoelectric behaviour of the SAW devices are discretized to a low level of abstraction and numerically computed. Moreover, the simulation procedure must be capable of automatically including the majority of the second order effects to gain deeper insight into the physics of SAW devices. Initial investigation suggests that the computationally intensive Finite Element Method (FEM) would be idle for the accurate modelling of SAW test structures and hence for the extraction of the complete set of parameters of the traditionally used phenomenological models such as Coupling-of-modes (COM) and P-matrix.

- All the SAW correlator modelling techniques discussed in the literature provide only an abstract insight into the analysis of certain design aspects of the device. However, for the comprehensive analysis of the behaviour of the correlator and investigation of its suitability for integration with a microvalve structure, a full

scale modelling and experimental validation of this device is demanded both in the frequency and time domains.

- The fabrication of microfluidic devices is time consuming, expensive and complex. The lack of a generalised architecture, especially for a specialised design such as the one proposed in the current research, necessitate a thorough understanding of the multiple coupled physics phenomenon at the process level, before fabrication. With the use of FEM based multiphysics modelling, the interactions between electromagnetic, piezoelectric, electroelastic and fluid fields needs to be analysed to get a better understanding of the operation and functioning of the microvalve.

- Optimum design of the contactless powering and wireless telemetry for the microvalve, being unique to the device specifications, requires a thorough understanding of the electromagnetic propagation around and inside the human body. This includes the modelling, characterisation and development of a reliable communication link specific to the device dimensions, surrounding environment, substrate material and, electrical and mechanical conformity with the structure.

1.3 Research Focus

The current work is a MEMS engineering research with application to novel microfluidic devices. With an overall goal to create new applications through the integration of existing technologies, a comprehensive design, modelling, optimisation and experimental validation approach is taken. Due to the multi-field nature of the project three specific and diverse areas within MEMS are studied. The first area corresponds to SAW technology followed by microfluidics, and body-centric communications; driven by the ultimate goal to demonstrate the operational feasibility of a human implanted, and wirelessly controlled microvalve.

Until recently, a considerable amount of effort for precise SAW filter characterisation, especially correlators, was focused heavily on experimentation, fabrication and processing. The dependence on fabricated test structures can be reduced considerably if the design optimization, new material evaluation and mode propagation characterisation of the device is carried out accurately using simulation tools. An ideal

technique for simulating a SAW device is numerically equivalent to solving the complete system of coupled partial differential equations driven by electric and mechanical fields, in a geometry consisting of a piezoelectric substrate with electrode gratings. Finite element analysis appears to be an attractive technique, which comes closest to comprehensive modelling of a complete acoustic correlator with minimal assumptions. This versatile technique automatically takes into account the effects of piezoelectric perturbation, mechanical perturbation, diffraction, backscattering, energy storage caused by non-radiating bulk waves, and electric flux leakage from the substrate surface (Hasegawa *et al.* 2001, Matthews 2007). Even though FEM is an established and widely accepted technique for mechanical engineering applications, the SAW device design community, in the past, was reluctant to tap its potential in the direct form. This can be attributed to the following two reasons:

- Traditionally, SAW devices were designed to operate in the MHz frequency range, mainly due to the limits placed by optical lithographic techniques on the line width. At these frequencies the electrode thickness is small compared to the SAW wavelength and hence was considered as negligible. For such an assumption, phenomenological models such as equivalent circuit or P-matrix model can be deemed sufficient to characterize the physics of SAW propagation. This was the main factor that discouraged the designers from employing computationally intensive and time consuming FEM. However, with the advent of X-ray lithography and the increasing demand for SAW devices operating in the GHz range, the electrode thickness is no longer a negligible parameter. Moreover, the impact of second effects, outlined above, on the device response is significant and cannot be subjected to simplifications and assumptions imposed by the phenomenological models. Hence, there is an increase in interest towards the use of FEM for SAW device modelling in recent years.

- The velocity of the propagating acoustic waves and the line width of electrodes being the two parameters impacting the operating frequency of SAW device ($f = v/\lambda$), an increase in velocity leads to a corresponding raise in the operating frequency of the SAW device. This has led to a shift in research focus from low velocity Rayleigh waves to high velocity leaky SAWs (LSAW) and surface transverse waves (STW). In addition to electrode thickness, the shear horizontal and bulk displacement components are crucial parameters of higher order modes.

The need for accurate and versatile characterisation of these parameters has further prompted the use of FEM.

In the current thesis, the requirements placed by microchannel length of the novel Microvalve structure necessitated the FEM modelling of SAW devices operating in MHz range, but not in GHz range. Nonetheless, the same modelling approach including the boundary and load conditions can be extended to devices with even nanometer linewidths.

Finite element methods have been developed in the past for modelling periodic structures and simple devices with few IDT electrodes (Xu 2000, Atashbar *et al.* 2004, Sankaranarayanan *et al.* 2007). However, the need to take advantage of versatility of FEM and to accurately account for the second order effects, supplemented by the availability of computational resources at reasonable cost, have prompted and enabled the novel modelling of a 3-dimensional SAW correlator with embedded pulse compression code in this research. Furthermore, the FEM multiphysics provides a rapid and inexpensive design evaluation, geometry independent resolution and the ability to seamlessly incorporate multiple materials and different loading conditions in microfludics. A comprehensive nonlinear transient loading and dynamic frequency characteristics of the microfluidics can be obtained with the inclusion of parameters such as structural spring force, squeeze film damping, fringing field, and intrinsic residual stresses, to simulate the practical test conditions. Moreover, these FEM results are easier to interpret as they reflect the characteristics of the physical structure. On the other hand, the numerical analysis of the microvalve biotelemetry link in the vicinity of a human body simulant is mandatory before indulging in fabrication. This is best possible through a 3-dimensional, high frequency electromagnetic, FEM modelling approach where the receiver antenna can be solved simultaneously with the transmitter antenna in the presence of a human body simulant. Thus, an accurate evaluation of the effect of lossy human tissue, radiation and parasitic reactance is feasible with this versatile technique. Moreover, the strong dependence of the loosely coupled power transmission link's performance on the trace metal thickness, line width, substrate material, number of turns, spacing between turns, impedance of the load, and the operating frequency provides a realistic prediction of the telemetry systems response when subjected to a RF signal excitation. A brief summary of the research efforts, to address the prior mentioned objectives, and the resulting research contributions of the author are outlined below.

1.3.1 SAW Parameter Extraction Using Finite Element Analysis

A standard SAW device modelling approach is to use phenomenological, scalar, approximate analytical models like Coupling-of-modes (COM) or P-matrix for the design. However, the validation of these design choices is normally carried out using computationally intensive, non-periodic, low level of abstraction numerical models. The propagation, interaction and coupling parameters in the scalar models are phenomenologically introduced. Thus, the heavy dependence of the scalar models on the accurate determination of parameters is evident. The parameter extraction is normally performed by manufacturing a test structure, which is time consuming and expensive. On the other hand, numerical models based on perturbation method, Finite Element Method-Spectral Domain Analysis (FEM/SDA), Finite Element Method-Boundary Element Method (FEM/BEM) are being employed for parameter extraction (Hasegawa *et al.* 2001, Ballandras and Bigler 1998, Hashimoto *et al.* 1999, Ventura *et al.* 1998, Thoma 1999). In the commonly used FEM/BEM and FEM/SDA models, the finite elements are used to account for the electrode shapes while the boundary elements or spectral domains are used to define the substrate type. Even though this results in a reduced computational time, the effects of deposited material's elastic properties, diffraction, and wave guiding are not taken into consideration in the above models. Moreover, the analytical handling of singularities in the Green's function and spectral domain formulations makes it hard to model complex SAW structures. In consideration of the advantages offered by FEM and the ever increasing demand for SAW devices operating at UHF and SHF bands, switching from FEM/BEM or FEM/SDA analysis to the versatile direct finite element method (FEM) modelling appears to be a logical choice, where the device is modelled by considering all the partial differential equations.

In this research, FEM was used to model an infinite periodic grating, which is equivalent to a long synchronous one-port resonator. The freely propagating eigenmodes and eigenvalues are analysed with modal analysis; where as the electrically active waves and electrical admittance are analysed using harmonic analysis. A curve fitting technique was employed to extract the COM/P-matrix model parameters from these FEM results. This approach is important as it facilitates the usage of approximate analytical models like COM or P-matrix in parallel, both to understand the basic physical behaviour and to model a complete SAW device (Wang *et al.* 2007, Li *et al.* 2008, Solal *et al.* 2003). Hence, a P-matrix model of a delayline filter is designed from the FEM

extracted parameters. Furthermore, experimental validation of the extracted parameters is carried out by fabricating the delayline and comparing the physical structure's response with the P-matrix model.

Research Contribution

FEM has been previously employed for the modelling of SAW and Leaky-SAW (LSAW) periodic structures and analysis of freely propagating eigenmodes, dispersion curves and second order effects (Hofer *et al.* 2002, Yong 2001, Xu 2000). Nonetheless, the parameter extraction with this approach, so far, is limited to instances where only freely propagating eigenmodes or dispersion curves are considered in the absence of excitation, when only two quantities were obtained (Rosler *et al.* 1995). However, the extraction of the complete set of COM parameters from the electrical admittance obtained from the finite element analysis of infinite periodic grating has not been addressed in the literature. This gap is addressed in this thesis by the finite element analysis of infinite periodic grating and extraction of the complete set of COM/P-matrix parameters from the electrical admittance using a fitting technique as discussed in Chapter. 2.

1.3.2 Finite Element Method Modelling of SAW Correlator

Precise characterisation of acoustic mode propagation determined by the encoded code sequence, device geometry and material characteristics is crucial for designing a SAW correlator. Existing SAW correlator modelling approaches, mostly based on the delta function and equivalent circuit models, are currently being employed to optimize the design process (Brocato 2004, Lee *et al.* 2002, Yu 2004). The reduction in computational time of these models is at the expense of assumptions or simplifications that are often invalid for actual designs (Ballandras *et al.* 2003).

In this research, the modelling of a 2 and 3-dimensional, 5×2-bit Barker sequence encoded acoustic wave correlator using a direct finite element model is demonstrated. The effect shear horizontal wave component has on the performance of a 5×2-bit Barker sequence encoded correlator was investigated using 3-D modelling. The correlator's response can be quantified in terms of harmonic analysis, to obtain the electrical admittance and output voltage profile, and transient analysis, to study the acoustic wave propagating characteristics and correlation pulses. Also, the dynamic responses of the device (such as displacement, and electric potential) when interrogated by different coded signals are examined and presented as a function of frequency. It should

be emphasised that while the objective of this research is to achieve finite element modelling of an acoustic wave correlator, it approaches the objective from a design optimisation viewpoint. That is, the aim is to determine how the dimensions, materials and harmonic acoustic modes influence the device response, and subsequently use these results to optimise the response. The validation of the simulation results is carried out by fabricating the SAW correlators using optical lithographic technique. A good agreement between the numerical and experimental results highlights the feasibility and potential of using FEM for application specific modelling of SAW correlators.

Research Contribution

Modelling of SAW correlators is not as straightforward as modelling other commonly used SAW devices due to the non-periodic nature of the device and the large problem domain. Hence, the modelling of these structures cannot be carried out with the same basic software tools that are commercially available for modelling SAW filters and resonators. To aid the correlator design process, a few modelling techniques were developed previously (Brocato 2004, Campbell 1998, Hashimoto 2000), where the second order effects such as backscattering, diffraction, charge distribution and mechanical loading (Matthews 2007, Xu 2000) are neglected. However, these approaches do not provide a comprehensive analysis of the correlators response, determined by variable structural dimensions and material types. The use of finite element techniques for predicting the response of a complete device is still in its infancy. This is mainly due to the reluctance of the design community to trade the device fabrication and testing approach or the use of phenomenological modelling with the computationally intensive FEM approach. However, with the availability of software packages with large node handling capability and the growing need to account for the impact of the majority of the second order effects on the device response, the use of FEM for numerical simulation of a SAW correlator, which has not been attempted before, appears to be efficient. On the other hand, shear horizontal and other higher order mode characterisation using FEM has been well addressed, in the past using small models (Sankaranarayanan *et al.* 2007, Hofer *et al.* 2002, Makkonen *et al.* 2006). However, quantitatively understanding the effect these modes have on the processing gain and the electromechanical coupling of a full scale acoustic device remained to be a challenging problem in FEM. This aspect is addressed in this research with the complete modelling of SAW correlator by neglecting features that contribute diminutively to the final output as described in Chapter. 3.

1.3.3 A SAW Based Remotely Actuated Microvalve Modelling

A normally closed, remotely actuated, secure coded, electrostatically driven, active microvalve using passive components is presented. This is carried out by utilising the complex signal processing capabilities of two identical, 5×2-bit Barker sequence encoded, acoustic wave correlators. A microchannel, comprising of two conducting diaphragms as the top and bottom walls, is placed in between the compressor IDT's of the two correlators. Fluid pumping can be achieved at ultrasonic frequencies by electrostatically actuating the edge clamped microchannel. Successful wireless operation of this device hinges on the precise occurrence of fluid flow when interrogated by a correlating BPSK signal. The microvalve is normally closed and is opened by temporarily deforming the microchannel by using electrostatic effect. The risk of high leakage and valve clogging is addressed by employing both diffuser elements and check valves in the structure.

Small device dimensions make it typically complicated or even impossible to perform measurements of the physical conditions inside microdevices. Due to the complexity involved in combining the electroacoustic and electrostatic mechanisms, a systematic design and optimization of the active microvalve is best possible with finite element method (FEM) modelling. Furthermore, coupled field simulations are vital for capturing the non-linear effects that are inherent in MEMS devices. In the current research, the emphasis is on the design and optimisation of the novel microfluidic structure through deflection analysis, both, to verify the functionality of the device and to investigate the working range of the structure. Secure interrogability of the microvalve is demonstrated using finite element modelling of the complete structure and the quantitative deduction of the code dependent, harmonic and transient microchannel actuation.

Research Contribution

Microfluidic devices using acoustic streaming phenomenon have been investigated in the past (Demirci 2006, Wixforth 2004). These devices use surface acoustic waves or flexural plate waves to cause fluid motion, through hydrodynamic coupling, on the planar surface of the piezoelectric material. Acoustic streaming based microfluidic devices have several advantages such as low fluidic impedance of the channel, simple structure and low sensitivity to the electrical and chemical properties of the fluid. However, acoustic streaming based wireless, fully passive microfluidic device has not

been reported so far. Even if developed, by employing recent innovations such as focusing of acoustic power with horns, lenses and focused transducers (Frampton *et al.* 2004, Yu *et al.* 2006), the secure actuation of such a device is limited only to frequency addressability rather than discrete code addressability, which would render it inefficient for remote interrogation applications. This constraint is resolved in this research by employing a synergetic approach which would combine electroacoustic correlation and electrostatic mechanisms. The correlator's response is utilised to impart ultrasonic energy on the conducting diaphragms using electrostatic actuation. Thus combining the high frequency operation of the ultrasonic, secure code embedded, acoustic correlator with low power, fast response time, and reliability of electrostatic actuation.

1.3.4 Wireless Telemetry System for the Implanted Microvalve

As the demand for miniaturisation grows, inductive coupling of energy could be a strong candidate for meeting the power and bi-directional data communication requirements of future implants (Jovanov and Raskovic 2006). The benefits offered by this approach such as, the elimination of battery or feed through wires, ease of implementation, increased portability, and higher chemical stability, have the potential to unfold many innovative biomedical applications. There are a number of design considerations for a telemetry link which are strongly determined by the application (Budinger 2003). Here, for the wireless actuation of a SAW correlator driven microvalve the important ones are the mechanical and electrical conformity with the SAW correlator, complications imposed on the implanted microvalve and reproduction of operating environment. Designing such a telemetry system is challenging as the small size of the device needs to be matched by a miniature antenna. In addition to the restriction imposed by the application on the receiving antenna size, factors such attenuation due to lossy human tissue and antenna efficiency determine the practicability of the remotely powered implant system.

The numerical and experimental analysis of the biotelemetry link for the microvalve is undertaken, in this research, in the vicinity of numerical and physical human body phantoms, respectively. To accurately account for the path losses and to address the design optimisation, the receiver coil/antenna is solved simultaneously with the transmitter coil/antenna in the presence of human body simulant using 3-dimensional, high frequency electromagnetic, FEM modelling. This modelling approach, which accounts for the radiation properties of the antennas and signal attenuation by the human body,

is feasible because of the short distance between the reader and implanted antennas. The insertion loss (S_{12}) of the coils is analysed from the simulated telemetry link both to maximise the transmitted power at the implanted coil, through the optimisation of mutual inductance, and to figure out an appropriate transmitter-receiver coil layout. Furthermore, to validate numerical calculations, the miniature antenna is fabricated on a 128° YX $LiNbO_3$ piezoelectric substrate where as the reader antenna is fabricated on a FR-4 substrate. The received relative signal strength is numerically and experimentally derived for a miniature ($6\times6\times0.5$ mm), square spiral antenna/coil when interrogated by a hand-held $8\times5\times0.2$ cm square spiral antenna/coil in the near field. This investigation is performed at a 10-100 MHz range when the two antennas are separated by a human body phantom of 5 cm thickness. Furthermore, the study of the variation in power transfer capabilities due to the changes in the orientation of the coils is important for moving loads. This is carried out by tilting the transmitter coil and analysing the drop in received relative signal strength, influenced by the reduced flux linkage between the misaligned coils. Finally, the experimental results confirm well with the FEM analysis predictions and hence ascertain the applicability of the developed system for secure interrogation and remote powering of the microvalve.

Research Contribution

The power is at a premium in the implants and hence its mandatory to design and develop a contactless powering system specific to the implant functionality. The choice of the size and layout of the implant antenna is guided by the aim to attain mechanical and electrical conformity with the microvalve structure. Moreover, the design of the body-centric communication system for the microvalve necessitates a thorough understanding of the electromagnetic wave interactions with the human tissues. Wireless transfer of power based on inductive coupling has been extensively investigated in the past (Lu *et al.* 2007, Si *et al.* 2008, Basset *et al.* 2007, Wang *et al.* 2004). However, most of these systems are incompatible with the proposed microvalve due to their large physical dimensions and the use of piezoelectric substrate in the current model. Furthermore, the use of integrated electronics technology in previous designs would not comply with the passivity requirement of the implanted microvalve. Hence, there is a need to custom design a receiver coil with high coupling sensitivity for the reception of sufficient power.

The modelling of inductive coupling between the transmitter and receiver coil is mathematically equivalent to the computation of all the electromagnetic field equations for

a given excitation and separation. The various inductive powering design approaches in the literature seem not to fully address the modelling of transmitter coil and the receiver coil simultaneously. The common approach of treating the receiver and transmitter coils separately or using empirical rules for design optimization cannot be applied to the current model (Neagu *et al.* 1997, Renauda *et al.* 2002, Vergara *et al.* 2007, Kim and Rahamat-Samii 2006, Theodoridis and Mollov 2005). This is because the generation of magnetic field pattern and the power coupling through the media representing human tissue are significant for holistic link budgeting. Hence, a novel microvalve specific, comprehensive 3-dimensional FEM modelling and optimisation of the biotelemetric link is carried out in the presence of human body simulant.

1.4 Thesis Structure

The structure of the thesis is as follows:

In Chapter 2, the COM/P-matrix parameter extraction and experimental validation is presented. The COM and P-matrix models are described in Section 2.2 & 2.3 respectively for SAW device modelling. The parameters needed by these models and the various parameter extraction techniques are outlined in Section 2.4. Then, in Section 2.5, the use of FEM for the simulation of a infinite periodic grating and analysis of eigenmodes and electrical admittance is described. The extraction of COM/P-matrix parameters using a curve fitting technique is discussed in Section 2.7. Section 2.8, presents the modelling of a P-matrix delay line filter using the extracted parameters and comparison with physical measurements.

Chapter 3 presents the modelling of a 2 and 3-dimensional, 5×2-bit Barker sequence encoded acoustic wave correlator using FEM. In Section 3.2, the SAW correlator operation, the various pulse compression coding schemes and signal processing functionality of the correlator are discussed. The various correlator modelling approaches are described in Section 3.3. Then in Section 3.4, the FEM SAW correlator design including the dimensions of the structure, materials used, and boundary conditions are discussed. After the description of the fabrication process flow in Section 3.5, both the simulation and experimental results are discussed in Section 3.6. This includes the harmonic analysis, transient analysis, the investigation of shear horizontal wave component and mismatched code correlator response.

In Chapter 4, the design and simulation of a 3-dimensional, remotely interrogatable, active microvalve is presented using two 5×2-bit Barker sequence encoded SAW correlators. In Section 4.2, the use of SAW devices for microfluidic applications including acoustic streaming is outlined. The principle of operation, the transmitter receiver architecture, electrostatic actuation and the finite element formulation is discussed in Section 4.3. Then in Section 4.4, the microchannel electrostatic model, including the dimensions of the structure and materials are described. The results of the comprehensive harmonic and transient deflection analysis of the microvalve for variable acoustic modes and different input interrogating code sequences are presented in section 4.5.

Chapter 5 presents the design and experimental validation of an inductive power transmission link for a wireless controlled microvalve. The requirements placed on the telemetric link due to the mechanical and electrical conformity with the SAW correlator, biomedical application and reproduction of the operating environment, are discussed in Section 5.2. Then in Section 5.3, the description of the transmitter receiver architecture of the microvalve is provided. Then in Section 5.4, the inductive link design including the layout and geometry of the hand-held and implant inductors, equivalent circuit and FEM modelling is presented. The simulation and measurement results comprising the quality factor, effective inductance, and relative signal strength in the frequency domain are outlined in the Section 5.5. Furthermore, the variation of the power transfer capabilities due to the tilting of the antennas is also discussed in the same section.

Finally, Chapter 6 provides the conclusion and a discussion on the possible future work.

This page is blank

Chapter 2

SAW Parameter Extraction Using Finite Element Analysis

2.1 Introduction

SAW devices have expanded into a multitude of products and applications in fields as diverse as microelectromechanical systems (MEMS), telecommunications, chemical sensing, and biotechnology (Mamishev *et al.* 2004, Pohl 2000, Gardner *et al.* 2001). A standard SAW device modelling approach is to use phenomenological, scalar, approximate analytical models like Coupling-of-modes (COM) or P-matrix for the design and to validate those design choices with computationally intensive, non-periodic, low level of abstraction, and numerical models. The propagation, interaction and coupling parameters in these scalar models are phenomenologically introduced. Thus, the heavy dependence of the scalar models on the accurate determination of parameters is evident. Hence, precise characterization of SAW parameters based on the device geometry and material characteristics is crucial for designing a SAW device.

The parameter extraction is normally performed by manufacturing a test structure, and then extract the needed parameters from measurements (Kondratiev *et al.* 2001). Such approach is both time consuming and expensive as each device optimisation would require fabricating a test structure. On the other hand, numerical models based on perturbation method, Finite Element Method-Spectral Domain Analysis (FEM/SDA), Finite Element Method-Boundary Element Method (FEM/BEM) are being employed for parameter extraction (Hasegawa *et al.* 2001, Ballandras and Bigler 1998, Hashimoto *et al.* 1999, Ventura *et al.* 1998, Thoma 1999). In commonly used FEM/BEM model, the finite elements are used to account for the electrode shapes while the substrate is modelled as boundary elements. This is carried out by replacing the differential equations

in the piezoelectric substrate by an integral equation at the boundary using Green's functions. Even though this results in a reduced computational time, the effects of deposited material's elastic properties, diffraction and, wave guiding are not simultaneously taken into consideration (Solal *et al.* 2004). Moreover, the analytical handling of singularities in the Green's function and spectral domain formulations makes it hard to model complex structures.

An ideal technique for simulating a SAW device is numerically equivalent to solving the complete system of coupled partial differential equations driven by electric and mechanical fields, in a geometry consisting of a piezoelectric substrate with electrode gratings. Considering the numerous advantages offered by FEM and the ever increasing demand for SAW devices with nanometer line widths, switching from FEM/BEM to the versatile direct finite element method (FEM) modelling appears to be a logical choice, where the device is modelled by considering all the partial differential equations. Nonetheless, the direct FEM has been previously employed for the modelling of SAW and Leaky-SAW (LSAW) periodic structures and analysis of freely propagating eigenmodes, dispersion curves and second order effects (Hofer *et al.* 2002, Yong 2001, Xu 2000). However, the parameter extraction with this approach was limited only to two quantities in the absence of excitation. Furthermore, a comprehensive modelling of an infinite periodic grating necessitates a close semblance to the experimental situation through the investigation of electrically active eigenmodes and electrical admittance. This approach is taken in this research where the complete set of SAW parameters are extracted in the presence of an excitation. Moreover, these FEM results are easier to interpret as they reflect the characteristics of the physical structure.

In this chapter, FEM is used to model an infinite periodic grating, which is equivalent to a long synchronous one-port resonator. The freely propagating eigenmodes and eigenvalues are analysed with modal analysis; where as the electrically active waves and electrical admittance are analysed using harmonic analysis. A curve fitting technique is employed to extract the COM/P-matrix model parameters from these FEM results. However, it is important to keep using approximate analytical models like COM or P-matrix in parallel, both to understand the basic physical behaviour and to model a complete SAW device (Wang *et al.* 2007, Li *et al.* 2008, Solal *et al.* 2003). Hence, a P-matrix model of a delayline filter is designed from the FEM extracted parameters. Furthermore, the experimental validation of the extracted parameters is carried out by fabricating the delayline and comparing the physical structure's response with the

P-matrix model. Even though this parameter extraction technique has not been latter employed for the design and optimisation of the microvalve, it serves as a precursor to establish the accuracy and versatility of the FEM technique.

In this Chapter, the COM and P-matrix models are described in Section 2.2 & 2.3 respectively, for SAW device modelling. The parameters needed by these models and the various parameter extraction techniques are outlined in Section 2.4. Then, in Section 2.5, the use of FEM for the simulation of a infinite periodic grating and analysis of eigenmodes and electrical admittance is described. The extraction of COM/P-matrix parameters using a curve fitting technique is discussed in Section 2.7. Section 2.8, presents the modelling of a P-matrix delay line filter using the extracted parameters and comparison with physical measurements.

2.2 Coupling-of-modes Model

Various numerical approximation techniques, such as, delta-function model, equivalent circuit model, angular spectrum of waves model, and coupling-of-modes model are available for the modelling and analysing of SAW devices. Coupling-of-modes (COM) is an efficient modelling approach where the excitation, propagation and mutual reflection of counter propagating acoustic modes is considered in addition to the acoustoelectric interactions of the electric current with the surface acoustic waves in a continuous medium.

The COM model is based on the Bragg condition, which states that the coupling between the incident wave ($T(x)$) and the reflected wave ($R(x)$), as shown in Fig. 2.1, is strong if the period of the grating, p, is equal or close to half of the wavelength, λ, i.e $p = \lambda/2$. These waves form a stopband by interfering constructively and destructively at two discrete frequencies, where the propagation into the medium is minimum. Only the incident wave and a reflecting wave may be considered in a stopband resulting in a coupling of modes approximation as they have significant amplitudes compared to other harmonics.

The coupling between the forward and backward propagating waves, in the presence of periodic grating, is best represented by the loaded wave equation given by (Plessky and Koskela 2000),

$$\frac{1}{\Delta(x)}\frac{d}{dx^2}(\Delta(x)) = {c_0}^2(\sigma(x) - 1), \tag{2.1}$$

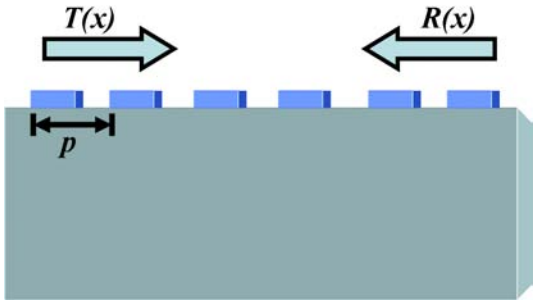

Figure 2.1. Counter propagating waves, $T(x)$ and $R(x)$, satisfying Bragg condition.

where $\Delta(x)$ can be described as stress, displacement, or electric potential normalised to the power flow in the x-direction and $c_0 = \omega/v_0$ is the propagation constant for the free surface. Here, $\sigma(x)$ is the periodic load density determined by the parameters corresponding to uniform loading (σ_0) and periodic loading ($\sigma_1 \& \theta_r$), expressed as

$$\sigma(x) = \sigma_0 - 2\sigma_1 \cos(2\pi x/p - \theta_r). \tag{2.2}$$

The eigenmodes of the load wave equation in Eqn. (2.1) are an infinite set of discrete harmonics consisting of a fundamental harmonic with wavenumber μ and infinite number of scattered harmonics with wavenumbers $\mu_z = \mu + z\frac{2\pi}{p}$; given by

$$\Delta(x) = \sum_{z=-\infty}^{z=+\infty} \Delta_z e^{-j(\mu+2\pi z/p)x}, \qquad \forall z : z \in Z. \tag{2.3}$$

Here Δ_z represents the amplitude of the individual harmonics. These harmonics of the eigenmodes, which are independent of the device geometry and physical nature of the waves in periodic structures, are interdependent. Hence when substituted back in Eqn. (2.1) would result in an infinite set of homogeneous equations (Plessky and Koskela 2000):

$$(\mu_z^2 - c^2)\Delta_z + \sigma_1 c_0^2 (e^{-j\theta_r}\Delta_{z+1} + e^{+j\theta_r}\Delta_{z-1}) = 0, \tag{2.4}$$

where $c = \omega/v$ is the loaded wavenumber under uniform loading.

The are two ways of deriving a finite system of equations from Eqn. (2.4). First is an algebraic approach where a few hundred harmonics are considered and solved using numerical simulations. This is an accurate method as all the strongly interacting harmonics are taken into account. Hence, this approach is used as a theoretical basis for intensively computational SAW modelling techniques, such as FEM, where retention of the physical details of different wave types are desired. We employ this approach in

this work for FEM periodic SAW structures modelling to derive the COM parameters. The other approach is the differential method where the truncated algebraic expressions are transformed into linear differential equations and solved. In the presence of periodic grating, due to Bragg condition, the field is dominated by a few strongly interacting harmonics in and around the central frequency $f_0 = v/2p$. As a result all other harmonics are ignored and only two counter-propagating are considered in the differential approach. This approach can be easily extended to non-uniform finite structures as the amplitude changes of a very limited number of interacting waves is considered. Hence, this differential approach along with the derived parameters from the algebraic approach can be used to model the various types of SAW components and devices.

The propagation constant (μ) close to the centre frequency can be written as a function of the dispersion from the centre frequency n, such as:

$$\mu = \frac{\pi}{p} + n, \qquad n \ll \frac{\pi}{p}. \tag{2.5}$$

As only two counter-propagating modes $(\Delta_-(x)$ & $\Delta_+(x))$ are considered in the differential approach given in Eqn. (2.3) and can be simplified to the form

$$\Delta(x) = \Delta_-(x) + \Delta_+(x) = \Delta_- e^{-jnx} e^{-j\pi x/p} + \Delta_+ e^{-jnx} e^{j\pi x/p}. \tag{2.6}$$

Here, the counter-propagating waves are a combination of fast oscillating factors $e^{\pm j\pi x/p}$ and slow oscillating factors $e^{\pm jnx}$. The slow varying fields in both the waves $\Delta_-(x)$ and $\Delta_+(x)$ can be represented with $K(x)$ and $L(x)$, respectively:

$$\Delta(x) = K(x)e^{-j\pi x/p} + L(x)e^{+j\pi x/p}. \tag{2.7}$$

By substituting the above equation in the loaded wave equation of Eqn. (2.1) and ignoring the high order harmonics, due to weak perturbations, results in two differential coupled wave equations are given by (Plessky and Koskela 2000)

$$\frac{\mathrm{d}K(x)}{\mathrm{d}x} = -j\delta K(x) + j\kappa L(x), \tag{2.8}$$

$$\frac{\mathrm{d}L(x)}{\mathrm{d}x} = -j\kappa^* K(x) + j\delta L(x). \tag{2.9}$$

Where κ is the reflectivity and δ is the detuning parameter given by

$$\delta = \frac{2\pi(f - f_0)}{v}. \tag{2.10}$$

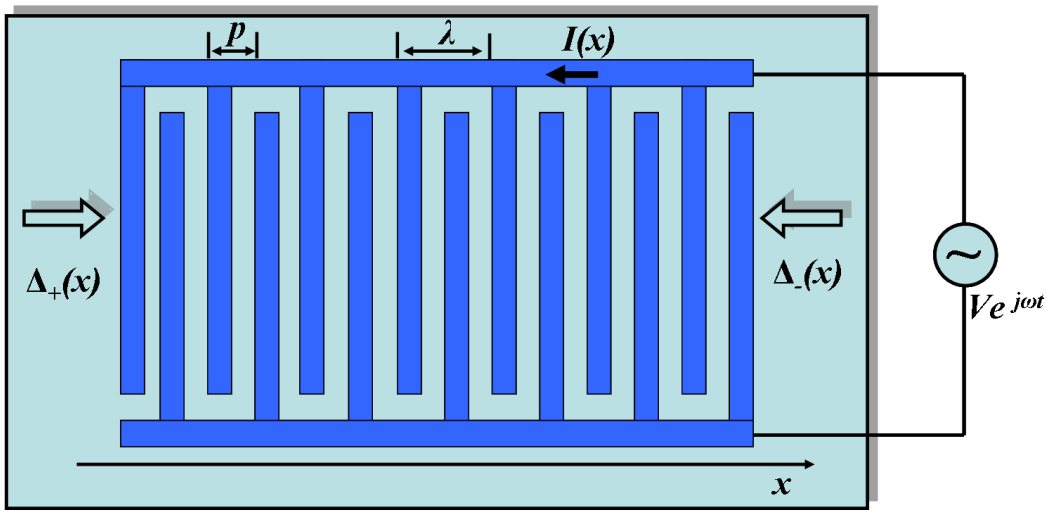

Figure 2.2. A SAW transducer with counter propagating modes $\Delta_+(x)$ and $\Delta_-(x)$, when driven by a voltage V.

In the case of a surface acoustic wave device, due to piezoelectric effect, an external drive voltage excites and propagates waves which in turn induce current in the electrodes. As shown in Fig. 2.2, if $\Delta_+(x)$ and $\Delta_-(x)$ represent the counter propagating modes in the positive and negative x direction of the structure and $I(x)$ is the current caused by the induced charges in the electrodes when the transducer is driven by a voltage V then the first order differential equations given in Eqns. (2.8) and (2.9) are rewritten to provide the coupling-of-modes equations of the form

$$\frac{\mathrm{d}K(x)}{\mathrm{d}x} = -j\delta K(x) + j\kappa L(x) + j\alpha V, \tag{2.11}$$

$$\frac{\mathrm{d}L(x)}{\mathrm{d}x} = -j\kappa^* K(x) + j\delta L(x) - j\alpha^* V, \tag{2.12}$$

$$\frac{\mathrm{d}I(x)}{\mathrm{d}x} = -2j\alpha^* K(x) - 2j\alpha L(x) + j\omega C V, \tag{2.13}$$

and the detuning parameter in Eqn. (2.10) assumes the form

$$\delta = \frac{2\pi(f - f_0)}{\nu} - j\gamma. \tag{2.14}$$

In the above equations the independent parameters κ, α, ν, γ and C are reflectivity due to perturbations, transduction coefficient, SAW velocity, attenuation, and capacitance per unit length, respectively. The asterisk denotes the complex conjugate. These parameters are dependent on the material type, metallization ratio, electrode thickness, crystal cut, aperture and shape of the electrodes and thus have to be generated to be able to perform the required modelling. Therefore, the COM model is as accurate as the technique used to determine the parameters.

The COM parameters are constant for uniform SAW structures. Here, the general solution for the COM equations (Eqns. (2.11) - (2.13)) can be taken as the sum of homogeneous and particular solutions. The homogeneous solution corresponds to the shorted-grating eigenmodes and the particular solution corresponds to the excited field. By excluding the excitation term, i.e by shorting the transducer, the COM equations reduce to the form given in Eqns. (2.8) - (2.9). The eigenmodes and the dispersion relation can be obtained by solving these reduced equations. The dispersion curve provides the relation between the wave number (n) of the slow varying fields of eigenmodes and the frequency, and can be expressed as

$$n = \pm\sqrt{\delta^2 - \kappa^2}. \tag{2.15}$$

Here, the eigenmodes form a stopband in the frequency region, $\delta \leq |\kappa|$, due to strong attenuation in the propagation direction. The magnitude of the reflection coefficient (κ) determines the width of the stopband. The lower and upper frequencies (f_{M-} & f_{M+}) of the stopband can be obtained by considering the zeros of dispersion relation in Eqn. (2.15) and neglecting the attenuation parameter γ (Plessky and Koskela 2000),

$$f_{M-} = (1 - \frac{|\kappa|p}{\pi})f_0 \tag{2.16}$$

$$f_{M+} = (1 + \frac{|\kappa|p}{\pi})f_0. \tag{2.17}$$

In this work the eigenmodes and the stopband edge frequencies are determined using modal analysis in FEM, as will be discussed in Section 2.5.

The particular solution is the excited field caused by the drive voltage V applied to the transducer. The amplitude of the excited field is expressed as

$$\begin{pmatrix} K_E \\ L_E \end{pmatrix} = \frac{1}{\delta^2 - |\kappa|^2}\begin{pmatrix} \delta\alpha + \kappa\alpha^* \\ \delta\alpha^* + \kappa^*\alpha \end{pmatrix} V. \tag{2.18}$$

The amplitudes interfere constructively at one edge of the stopband causing resonance and interfere destructively at the other edge according to the sign of κ. The values of κ and α are real for symmetric structures.

The general solution of the COM equations can thus be expressed as a combination of short-grating eigenmodes and excited fields, such as

$$\begin{pmatrix} K(x) \\ L(x) \end{pmatrix} = M_-\begin{pmatrix} K_-(x) \\ L_-(x) \end{pmatrix} + M_+\begin{pmatrix} K_+(x) \\ L_+(x) \end{pmatrix} + \begin{pmatrix} K_E(x) \\ L_E(x) \end{pmatrix} V. \tag{2.19}$$

Here, M_- and M_+ are the coefficients corresponding to the two short-grating eigenmodes. These coefficients can be solved from the acoustic boundary conditions.

2.3 P-matrix Model

In the design of complex SAW devices, the need might arise to use individual electrodes with varying properties, which may render the COM model ineffective. In such structures P-matrix model, which is an extension of COM model, is an efficient modelling technique where the linear COM equations for each component are expressed as the elements of a matrix called P-matrix. The total response of the device can be determined by the cascading the P-matrices of all the individual components. The cascading is undertaken by considering the output wave amplitude of one component as the input wave amplitude of the neighboring component. This is based on the assumption that there is no change in the polarization of the wave from one component of the device to the other, which is applicable to a wide range of devices. Furthermore, the parameters used in P-matrix model are the same as the one's used in COM model. Hence, the COM parameters can be used to derive the P-matrix of the device. The P-matrix model considers the SAW components as a three port device with two acoustic ports and one electric port, as shown in the Fig. 2.3. The waves arriving from outside such as the drive voltage V and the acoustic amplitudes $\Delta_+(l1)$ and $\Delta_-(l2)$ determine the response of the structure in the form of waves departing from the structure, i.e., the current I and the acoustic amplitudes $\Delta_-(l1)$ and $\Delta_+(l2)$.

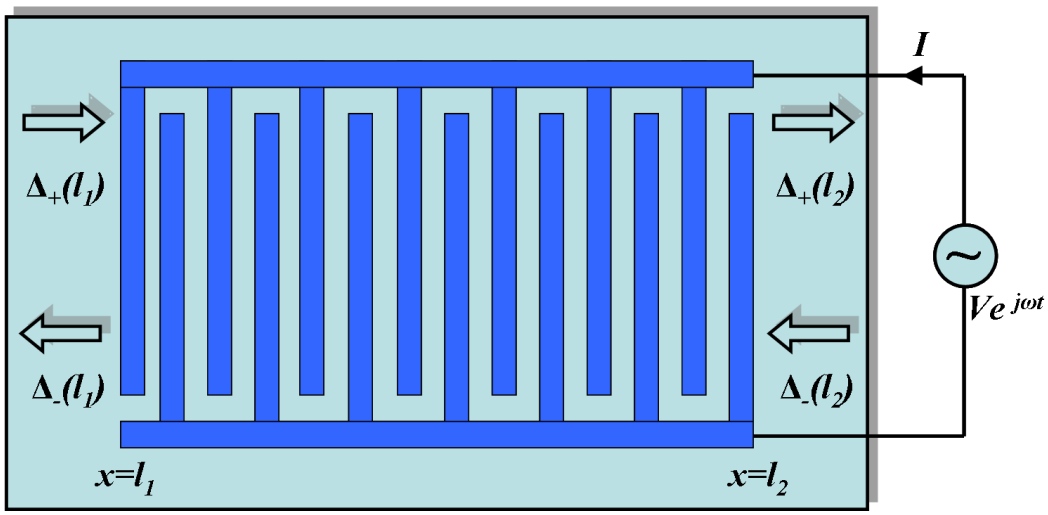

Figure 2.3. P-matrix representation of an IDT with two acoustic ports and one electric port.

The P-matrix for the IDT shown in Fig. 2.3 is given by

$$\begin{pmatrix} \Delta_-(l1) \\ \Delta_+(l2) \\ I \end{pmatrix} = \begin{pmatrix} R_{11}(f) & T_{12}(f) & E_{13}(f) \\ T_{21}(f) & R_{22}(f) & E_{23}(f) \\ I_{31}(f) & I_{32}(f) & A_{33}(f) \end{pmatrix} \begin{pmatrix} \Delta_+(l1) \\ \Delta_-(l2) \\ V \end{pmatrix}. \tag{2.20}$$

Here, the scattering of the waves is characterised by the transmission coefficients T_{12} and T_{21} and the reflection coefficients R_{11} and R_{22}. The scattering elements of the matrix are given by

$$R_{11} = \frac{j\kappa^* \sin(nL)}{n\cos(nL) + j\delta\sin(nL)}, \tag{2.21}$$

$$T_{12} = T_{21} = \frac{(-1)^N n}{n\cos(nL) + j\delta\sin(nL)}, \tag{2.22}$$

$$R_{22} = \frac{j\kappa \sin(nL)}{n\cos(nL) + j\delta\sin(nL)}. \tag{2.23}$$

Here, L is the length of the device and n is the slowly-varying wavenumber of the eigenmode. The excitation efficiency of the IDT in response to the drive voltage is represented by E_{13} and E_{23} as

$$E_{13} = -\alpha L \frac{\sin(nL/2)}{nL/2} \frac{(\delta+\kappa)(\sin(nL/2)) - jn\cos(nL/2)}{n\cos(nL) + i\delta\sin(nL)}, \tag{2.24}$$

$$E_{23} = (-1)^N E_{13}, \tag{2.25}$$

and the current induced by the arriving waves at the acoustic ports is described by the matrix elements I_{31} and I_{32} expressed in the form

$$I_{31} = -2E_{13}, \qquad I_{32} = -2E_{23}. \tag{2.26}$$

One of the important elements of the P-matrix is the admittance (A_{33}), which depicts the electrical behaviour of a uniform bidirectional structure (IDT or a reflector) by relating the current I in the structure to the voltage V and given by (Plessky and Koskela 2000)

$$A_{33} = A_{33}^M + A_{33}^E. \tag{2.27}$$

Here, A_{33}^M is the homogeneous component of the admittance determined by the eigenmodes,

$$A_{33}^M = -\frac{4\alpha^2(\delta+\kappa)}{n^3} \frac{(\delta+\kappa)(1-\cos(nL)) - jn\sin(nL)}{n\cos(nL) + j\delta\sin(nL)}, \tag{2.28}$$

Table 2.1. Normalized COM parameters (Koskela *et al.* 1999)

NOTE:
This table is included on page 32
of the print copy of the thesis held in
the University of Adelaide Library.

Here, A_{33}^{E} is the particular solution component of the admittance caused by the excited field.

$$A_{33}^{E} = -j(\frac{4\alpha^2}{\delta - \kappa}L - \omega LC). \tag{2.29}$$

The A_{33}^{E} component dominates the admittance for long structures. These responses are analysed by using FEM harmonic analysis, as explained in Section 2.6. Furthermore, the admittance curves obtained from the P-matrix model, derived using the extracted COM parameters, and the physical structure are compared.

2.4 COM/P-matrix Parameters and Extraction Techniques

The parameters in the COM equations (Eqn. (2.11) - (2.13)) are determined by the material properties of the structures, crystal cut, shape of the electrodes, metallization ratio and aperture. These parameters, which are reflectivity (κ) due to perturbations, transduction coefficient (α), SAW velocity (v), attenuation (γ), and capacitance per unit length (C), can be normalized to the periodicity ($p = \lambda_0/2$) and aperture (A) of the structure, as shown in Table 2.1. This normalization makes the parameters scale-invariant constants. The accurate determination of these parameters influences the precision of the COM or the P-matrix modelling approach.

The velocity (v) is one of the important parameters of a SAW device as it determines the operating frequency and hence the usability of a device for signal processing and sensing applications. The velocity is in turn dependent on the electrical and mechanical loading of the electrodes and wave guiding capabilities of the piezoelectric material. The normalized reflectivity (κ_p), i.e. the reflection coefficient per period, is influenced by the reflectivity due to piezoelectric loading and mechanical loading. Both these

parameters, velocity and reflectivity, are effected by the width and thickness of the electrodes in addition to the piezoelectric coupling coefficient and can be determined from the edges of the stopband.

The transduction coefficient is a measure of the wave excitation in the structure determined by the piezoelectric coupling coefficient which, is proportional to length of the structure and the square root of the aperture. The normalized transduction coefficient (α_n) is considered to eliminate the dependence on the length and aperture of the structure, as shown in the Table 2.1. The strength of the resonance reflects the value of the transduction coefficient.

SAW attenuation (γ_p) is one of the hardest parameters to extract. This is due to its high sensitivity to the operating frequency, structural geometry and crystal cut. The major factors that contribute to the attenuation are: acoustoelectric interactions, diffraction, coupling with parasitic modes, acoustic losses due to electrodes and wave scattering on the surface of the crystal (Plessky and Koskela 2000). The attenuation determines the quality factor of the resonance.

The capacitance (C_p) is a measure of the electrostatic energy stored in a periodic structure. As it is dependent on the length and aperture of the structure is normalized by those quantities to obtain a scale-invariant constant (C_n). The susceptance level of the admittance curve, away from the stopband, determines the normalized capacitance.

The extraction techniques for the parameters outlined above can be classified into two approaches. The first approach is by the experimental measurements from the test structures using laser probe techniques or by fitting the projections of the COM model on to the test structure response. The other approach is by the theoretical analysis of the structure using analytical techniques such as perturbation method or numerical simulations such as finite element method-spectral domain analysis or finite element method-boundary element method. These two approaches are discussed in detail below.

2.4.1 Test Structures

The measurements from test structure has the advantage of extracting the parameters from a real device for a given technology. The knowledge of the electrode shape and material types is not required as all effects, such as variations in the geometry and material properties, are naturally included. All parameters can be extracted from the

electrical response of the test structure, which is best represented by the admittance measurement (Iriarte *et al.* 2003). The synchronous one-port resonator, as shown in Fig. 2.4, is the widely used test structure (Kondratiev *et al.* 2001). However, the drawback of this approach is that a specific test structure has to be manufactured for designs with different materials, metal shapes, geometry and frequency range. Thus, rendering this approach both time-consuming and uneconomical.

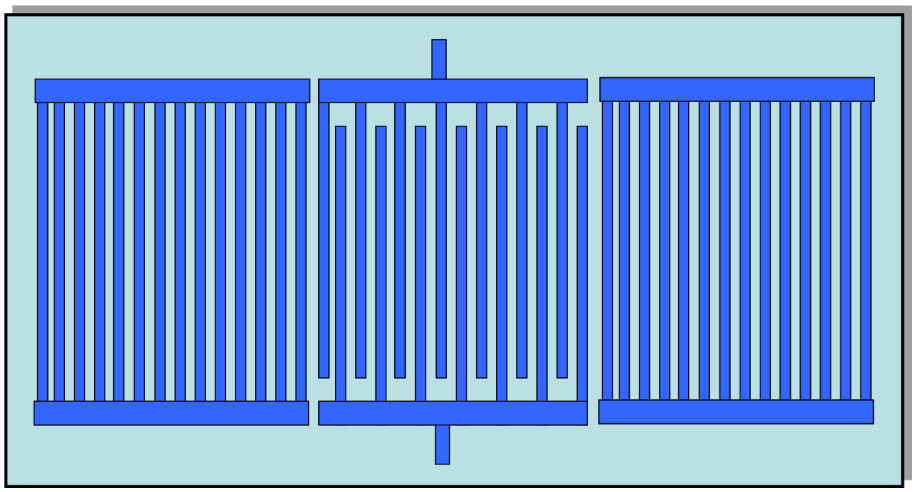

Figure 2.4. Synchronous one-port resonator with an IDT and two reflectors for parameter extraction. The IDT generates the acoustic waves which are reflected in-phase by the reflectors, forming a standing wave pattern.

2.4.2 Perturbation Method

The perturbation method is an analytical technique where the electrodes are replaced with mechanical perturbations on the propagating substrate. The response of the SAW device is obtained from the frequency shift induced by the small perturbations. As the thickness of the electrodes is neglected, this method is not suitable for devices with high electrode thicknesses and complicated electrode patterns. Moreover, the piezoelectric coupling is assumed to be weak so the effects of piezoelectric perturbation, and energy storage caused by non-radiative bulk waves are not taken into consideration (Hasegawa *et al.* 2001, Wang *et al.* 1996). Devices operating on non-Rayleigh modes such as leaky and surface transverse waves are hard to model using this method. This is because of the high sensitivity of these waves to the electrode thickness and surface conditions. Furthermore, the transduction coefficient and phases of the counter propagating modes cannot be determined with the perturbation method.

2.4.3 Finite Element Method-Spectral Domain Analysis (FEM/SDA)

In the finite element method-spectral domain analysis (FEM/SDA) or the hybrid finite element method (HFEM) the electrodes are modelled using finite element method and the piezoelectric substrate fields are modelled using spectral domain analysis. This technique is based on the analysis of the eigenmodes of the structure, in the absence of voltage excitation, by calculating the dispersion relation, as shown in Eqn. (2.15), for electrically open and shorted electrodes. The dispersion relations for the open (DR_o) and shorted (DR_s) gratings are obtained by solving the determinantal system of field equations with boundary conditions for a given frequency (Hasegawa and Koshiba 2003, Hashimoto *et al.* 2000). The extraction of all the SAW parameters is only possible with the knowledge of the electrical response of the structure, which is best described by the harmonic admittance. As the eigenmodes of the electrically open and shorted gratings represent the zeros and poles of the harmonic admittance ($A(\gamma, f)$), it can be expressed as:

$$A(\gamma, f) = \frac{DR_o(\gamma, f)}{DR_s(\gamma, f)}. \tag{2.30}$$

The precise calculation of these dispersion relations across a wide frequency range is crucial for an accurate determination of the parameters. The limitations of this method are: (*i*) The dispersion behaviour is deviant in the vicinity of the stopband and hence, for a dispersive structure, all the parameters cannot be extracted from the knowledge of the stopband edges. (*ii*) In lossy SAW devices, the damping of the resonances restricts the usability of the method. (*iii*) The analysis of the standing wave distribution is limited to the instance where the electrodes are open or short circuited. Therefore, the accurate computation of electric potential distribution is not feasible.

2.4.4 Finite Element Method-Boundary Element Method (FEM/BEM)

The FEM/BEM is a modelling technique where the electrodes are accounted for by the finite elements and the piezoelectric substrate is represented by the boundary elements. The piezoelectric equations corresponding to the substrate are represented in the integral form using Green's function. If G(x) is the Green's function in the x domain, then the displacement ($u_i(x)$) and electric potential ($\phi(x)$) can be related to the normal component of stress (t_n) and electrical displacement (σ), at the interface

between the electrodes and the substrate, as

$$\begin{pmatrix} u_i(x) \\ \phi(x) \end{pmatrix} = \int_{-\infty}^{+\infty} G(x-x') \begin{pmatrix} t_n(x') \\ \sigma(x') \end{pmatrix} dx'. \tag{2.31}$$

Here, the Green's function is a 4×4 matrix as the displacement ($u_i(x)$) has three components.

An idle test structure for parameter extraction is a SAW resonator with large array of identical electrodes. This structure can be approximated as an infinite periodic array of electrodes without compromising the accuracy of measurement. Hence only a periodic structure is considered by neglecting the end effects. This assumption is valid as the fields decay strongly in the presence of reflective arrays. For a periodic structure with periodicity p and driven by a γ harmonic potential excitation, Eqn. (2.31) can be rewritten as

$$\begin{pmatrix} u_i(x) \\ \phi(x) \end{pmatrix} = \frac{1}{p} \int_{-p/2}^{+p/2} G_p^{\gamma}(x-x') \begin{pmatrix} t_n(x') \\ \sigma(x') \end{pmatrix} dx'. \tag{2.32}$$

Here, the periodic harmonic Green's function $G_p^{\gamma}(x)$ can be expressed as

$$G_p^{\gamma}(x) = \sum_{n=-\infty}^{n=+\infty} G(x-np) e^{-j2\pi n\gamma}. \tag{2.33}$$

The mechanical interactions between the acoustic waves are ignored in this periodic Green's function. The parameters in periodic FEM/BEM models are normally extracted from harmonic admittance calculated from the dispersion relations of shorted and open gratings (Laud and Ballandras 2003, Makkonen *et al.* 2002). The dispersion relations (DR_o) and (DR_s) can be obtained as the determinants of the system of the equations given in Eqn. (2.32). As only the homogenous solution of the model is considered, it is hard to analyse the coupling to a voltage excitation. Moreover, this technique is not suitable for the analysis of pseudo-surface acoustic wave (PSAW) devices. This is because of the close proximity of the stopband to higher order modes. Furthermode, the Green's function with complex valued wave numbers compromises the continuity of the function in the complex plane (Plessky and Koskela 2000).

On the other hand, Koskela *et al.* (1999) and Laude *et al.* (2004) have investigated the generation formulation in the presence of voltage excitation, as an alternative to the analysis of the short and open grated dispersion relations. The results obtained in the form of electrically active eigenmodes and electrical admittance have a close resemblance to the experimental situations and hence are easier to analyse. However, factors

such as, deposited material's elastic properties, diffraction and, wave guiding are not considered in the generation formulation of the FEM/BEM models. As a result, these models are limited to designs with electrodes on plane substrates.

2.4.5 Direct Finite Element Method (FEM)

Field theory is best suited for the design of SAW devices as it involves the resolution of all the partial differential equations for a given excitation. The direct finite element method (FEM) is the most appropriate numerical representation of field theory where the piezoelectric behaviour of the SAW devices are discretized to a low level of abstraction and numerically solved (Hofer *et al.* 2002). Apart from the automatic inclusion of all the second order effects, a better insight into the physics of SAW devices can be attained. The coupled mechanical equations of motion and Maxwell's equations for the electrical behavior governing the piezoelectric effect are solved in FEM for the the amplitudes of the mechanical displacement u_i and the electrical scalar potential ϕ:

$$c^E_{ijkl}\frac{\partial^2 u_k}{\partial x_j \partial x_l} + e_{kij}\frac{\partial^2 \phi}{\partial x_k \partial x_j} = \rho\frac{\partial^2 u_i}{\partial t^2} \tag{2.34}$$

$$e_{ikl}\frac{\partial^2 u_k}{\partial x_i \partial x_l} - \varepsilon^S_{ik}\frac{\partial^2 \phi}{\partial x_i \partial x_k} = 0 \tag{2.35}$$

here e_{kij} is the piezoelectric constant, ε^S_{ik} the permittivity for constant strain, c^E_{ijkl} the stiffness constant for constant electric field, and ρ the density of mass.

In FEM, the model is discretized into smaller elements that are connected through nodes. The approximation of the displacement $u_i(x)$ and electric potential $\phi(x)$ of the element by the interpolation function is given by

$$u_i(x) = \sum_n N_n(x) u_{in} \tag{2.36}$$

$$\phi(x) = \sum_n N_n(x) \phi_n, \tag{2.37}$$

where ϕ_n and u_{in} are the values of the potential and the displacement at a node of the element. $N_n(x)$ is the shape function of the element and the index n denotes the node number of the element.

The FEM/BEM and HFEM methods necessitate the formulation of Green's function and spectral domain, respectively. Hence, analytical handling of the singularities within those formulations is required. However, such an exercise can be avoided with a versatile direct FEM approach. Furthermore, there is a high level of flexibility for modelling

complex shaped structures and analysing geometric variations. However, the versatility and flexibility come at a cost of large computational time and memory space requirements. With the growing demand for accurate and simultaneous characterisation of the majority of the second order effects complimented by the availability of software package's with large node handling capability, and increase in computing performance and memory capacity, switching to a direct FEM for numerical simulation of SAW devices appears to be feasible and straightforward.

The analysis of infinite gratings using periodic boundary conditions in FEM was previously performed by Yong (2001) to study the effect of mode shapes, temperature variations and electrode dimensions for SAW, BAW and LSAW resonators. Buchner *et al.* (1991) and Rosler *et al.* (1995) have used the same method to extract the velocity and reflectivity parameters from SAW and LSAW crystals respectively. Moreover, Rosler *et al.* (1995) have compared these two parameters extracted from the FEM model with the one's extracted from periodic partial wave method, periodic Green's function method (FEM/BEM) and experimental measurement. It was concluded that the FEM calculations were closest to the experimental measurements, when compared to the other methods. The FEM periodic structural analysis discussed so far is limited to the instance where only freely propagating eigenmodes or dispersion curves are considered in the absence of excitation, also confirmed by Koshiba *et al.* (1997).

Hofer *et al.* (2006) and Ballandras *et al.* (2003) have investigated the generation problem by driving an infinite periodic grating with harmonic voltage excitation and deriving the electrical admittance and mutual admittance respectively. Moreover, the admittance obtained from FEM simulations was compared to the experimental admittance measurement of a synchronous one-port resonator by Hofer *et al.* (2006). A good agreement between both the results was reported. Furthermore, Le Brizoual *et al.* (2006) have used the same approach for the modelling of diamond based surface SAW layered structures. The admittance response and electrically active eigenmodes were used to determine the penetration depths of the fundamental or harmonic modes. However, the extraction of the complete set of COM parameters from the electrical admittance obtained from the finite element analysis of infinite periodic grating is still an issue. This gap is addressed in this chapter by the finite element analysis of infinite periodic grating and extraction of the COM parameters from the electrical admittance using a fitting technique, as will be discussed in the latter sections.

2.5 FEM of a Infinite Periodic Grating

The modelling of an infinite periodic grating is numerically equivalent to modelling an one-port synchronous resonator with a large number of IDT and reflector gratings. As the SAW resonators are idle test structures for parameter extraction (Kondratiev *et al.* 2001), it suffices to model a periodic structure in FEM. Moreover, the effect of wave reflections from the boundaries are negligible for long resonators. Therefore, the application of the periodic boundary conditions (PBCs) on the side walls of the model would not compromise the accuracy of the computed admittance in the proximity of a stopband. The simulation of a periodic array, which involves solving the system of coupled partial differential equations governing the mechanical and electric fields, in a geometry consisting of the semi-infinite piezoelectric crystal and the periodic electrode array was carried out with a commercially available FEM package (ANSYS). In the following subsections, a discussion of geometry and boundary conditions and how they are employed for the modelling of periodic structures is presented.

2.5.1 Geometry

A long synchronous one-port resonator with hundreds of electrodes for IDT and reflectors is modelled as a periodic structure with a length of one wavelength ($\lambda = 40\ \mu$m), as shown in Fig. 2.5. Here, one wavelength of the device is enough to model the standing wave of the whole structure (Yong 2001). Hence, the reduction in the complexity and size of the numerical model is realisable. The depth of the substrate is considered as 12 wavelengths, which approximates the thickness of the piezoelectric crystals commercially available. The metal gratings with finger widths of $\lambda/4$ are defined on top of the substrate for a metallization ratio (MR = p/λ) of 0.5 and thickness (h/λ) of 3%.

A 128° Y-cut X propagating $LiNbO_3$ piezoelectric material was chosen for the substrate due to its high electromechanical coupling coefficient for Rayleigh SAW. The material properties of $LiNbO_3$ are obtained from Auld (1990 (2^{nd} Edition)) and transformed by an Euler angle of (0°, 38°, 0°) for the 128° YX crystal cut, as shown in Appendix. A. The electrodes are modelled as gold as it is the more commonly used material for X-ray lithography. Therefore, it is easier to validate the extracted parameters with a proof-of-principal prototype built using gold. The model is discretized into 2-D quadratic coupled field elements with 8 nodes per element and 3 degrees of freedom (U_x, U_y and Voltage) per node. The accurate representation of the acoustic wave profiles is

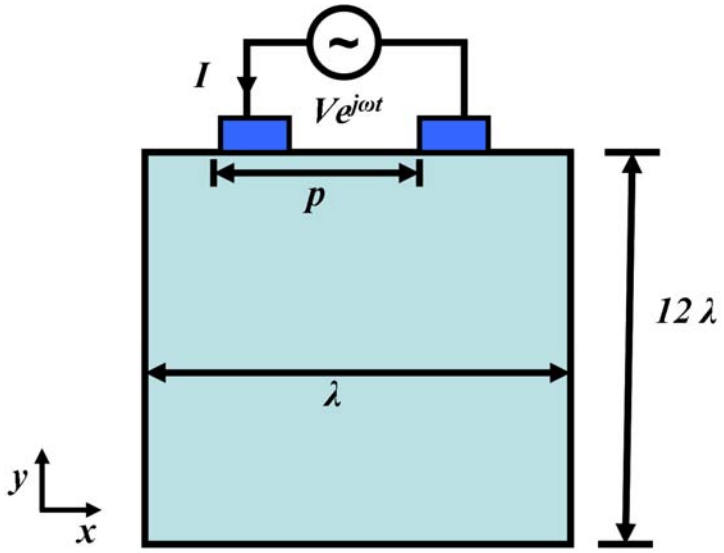

Figure 2.5. A periodic structure with two electrodes and a substrate depth of 12λ.

determined by the size of the element. To ensure precise finite element results, the element size is taken as $\lambda/30$, resulting in a model comprising of 12 thousand elements.

2.5.2 Periodic Boundary Conditions

The standing waves are spatially periodic in SAW and BAW devices with the same grating shape and substrate. Hence, it suffices to simulate just a periodic substructure with periodic boundary conditions (PBCs). This analysis of a periodic substructure yields the frequency response and other design characteristics of the whole structure. With the use of PBCs, each mode that can be excited within the periodic structure can be modelled. As the periodic structure is part of the parent structure, the displacement and electric potential at both the left and right periodic boundaries are made equal. The degrees of freedom on the left boundary can be related to the degrees of freedom on the right boundary using the Eqns. (2.36 and 2.37) as follows

$$\sum_{n_L} N_{n_L}(x) u_{in_L} = \sum_{n_R} N_{n_R}(x) u_{in_R}, \tag{2.38}$$

$$\sum_{n_L} N_{n_L}(x) \phi_{n_L} = \sum_{n_R} N_{n_R}(x) \phi_{n_R}. \tag{2.39}$$

Here, the indices n_L and n_R denote the node numbers of the FEM model in the left and right boundaries, respectively.

A plain strain condition is assumed to reduce the model to a 2-D model. This assumption is valid for structures with a dominant wave propagation in the sagittal plane (Yong 2001). As 128° YX $LiNbO_3$ is a Rayleigh SAW crystal, there is primarily a straight crested wave propagation. Furthermore, the large electrode apertures of the structures support the 2-D assumption. The space above the electrodes and the substrate is modelled as air. As the charge distribution in the electrodes is used for admittance computation, the surface charge of the electrode-air interface cannot be ignored. This boundary condition applies particularly for materials with low dielectric constants (ϵ_r) since the surface charge at the electrode-air interface is computed as $1/\epsilon_r$ times the charge at electrode-substrate interface. Hofer *et al.* (2002) have reported an error of 16% in the charge calculation of the electrodes on a quartz substrate without air/vaccume boundary. Hence, an air boundary is defined on the surface of the periodic structure. As the thickness of the substrate is approximately equivalent to the thicknesses of the commercially available piezoelectric wafers, it is clamped and grounded at the bottom to closely replicate the experimental situation. The simulation results of the periodic structure modelled with these boundary conditions are presented in the following section.

2.6 Results

The response of the finite periodic grating structure can be investigated using two techniques. The first is the eigenmode analysis or modal analysis, where the homogeneous solution of the differential equations is computed to determine the eigenvalues and vectors of the structure. Here, the freely propagating modes, particularly symmetric and anti-symmetric SAW modes, are studied through the examination of eigenvectors and eigenfrequencies. This can be used as a starting point for other computationally intensive analysis involving model excitation. The other analysis technique is the harmonic analysis, where a frequency sweep is employed to determine the particular solution of the differential equations for a given voltage excitation. Here, the electrical input admittance of the structure is calculated from the knowledge of the charge on the electrodes. The singularity points in the harmonic analysis can be used to describe the electrically active eigenmodes thus allowing the quantification of electrical and mechanical responses.

2.6.1 Modal Analysis

The homogeneous solution of the differential equations involved in the finite element modelling of the infinite periodic grating is calculated using modal analysis so as to observe the freely propagating eigenmodes in the structure. The electrodes are either short or open circuit for this case and no external drive voltage is applied. By studying the mode shapes of the periodic structures, the two stopband edge frequencies of the resonator are identified. As the wave motion is confined to the top surface of the substrate for the SAW modes they can be differentiated from other modes.

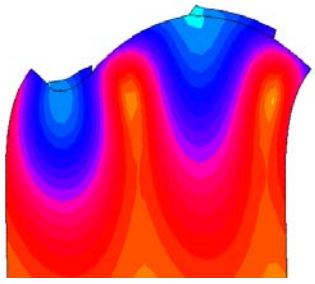

Figure 2.6. Anti-symmetric SAW mode (f_{M+}) at 80.48 MHz, where the electrodes on the surface of the piezoelectric substrate deform anti-symmetrically about its centreline.

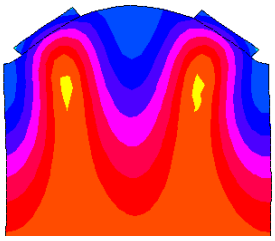

Figure 2.7. Symmetric SAW mode (f_{M-}) at 82 MHz, where the electrodes on the surface of the piezoelectric substrate deform symmetrically about its centreline.

For the periodic structure, two SAW modes were observed at 80.48 MHz and 82 MHz as shown in the Figs. 2.7 and 2.6. The differences in the deformation of the electrodes in both the modes (Yong 2001) and the displacement profiles of the top ends of the side walls in the lateral and vertical direction (Kannan 2006) are used to identify the symmetric (f_{M-}) and anti-symmetric modal frequencies (f_{M+}). The electrodes of the anti-symmetric SAW mode deform anti-symmetrically about its centreline and the Y displacement component of the top ends of the side walls is zero. However, for a

symmetric SAW mode, the electrode deformation is symmetric about its centreline and the x displacement component of the top ends of the side walls is zero. By applying this conditions to the two observed SAW modes in the Figs. 2.7 and 2.6, f_{M+} and f_{M-} was measured to be 80.48 MHz and 82 MHz, respectively. These eigenvalues form the edges of the stopband where the propagation into the medium is negligible. Here, the electrode width determines the bandgap between the symmetric and anti-symmetric saw modes where as the electrode thickness determines the SAW modal frequencies. These proportionalities have been highlighted by Plessky and Koskela (2000) through the analysis of SAW parameters for variable electrode widths and thicknesses. There it was depicted that as the electrode thickness increases the SAW modal frequencies decreases due to the mass loading effect. On the other hand, it was also shown that the bandgap increases with increasing electrode width.

2.6.2 Harmonic Analysis

The evaluation of freely propagating eigenmodes in the modal analysis corresponds to the instance where the electrodes are short or open circuit. Even though this analysis provides valuable information about the stopband edge frequencies and mode shapes, it does not relate to the experimental situation. However, the excitation properties of the structure can be studied with the harmonic analysis. This is carried out by employing a voltage source to supply additional energy to the propagating waves in the frequency domain. Here, the particular solution of the differential equations governing the electrical and mechanical properties of the model is evaluated. A drive voltage of $\pm 1\ V$ was applied across the electrodes and the steady state response was examined around the stopband edge frequencies, obtained from the modal analysis. The electric potential of all the nodes of the individual electrodes was coupled to keep the voltage through out the electrode area constant for a given time.

The mechanical and electrical responses, quantified by the integral calculations, can be used to analyse the displacements or electric potentials for the region of interest. Hence, the electrically active eigenmodes can be studied from the examination of displacement and potential contours from the singularity point in the frequency domain. The harmonic order of the electrically active eigenwaves was determined by the number of nodes. The displacement contour of the periodic structure for f_{M+} is shown in the Fig. 2.8. It can be observed that the displacement is confined to the top surface of the structure with a maximum value of 3.63 nm close to the electrodes.

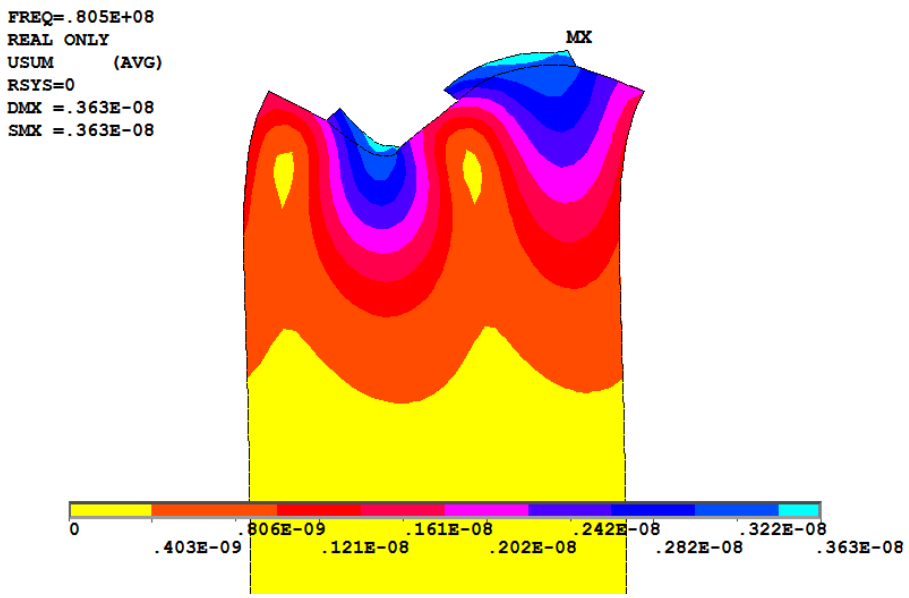

Figure 2.8. SAW displacement contour. Here, the particle displacement is limited to the top surface of the structure, reiterating the excitation of surface acoustic wave.

The complex admittance, which characterises the electrical behaviour of the SAW device, can be determined from the complete charge distribution on the electrodes. Furthermore, as the complex admittance reveals all the resonances (natural frequencies corresponding to the short-circuited electrodes) and anti-resonance (natural frequencies corresponding to the open-circuit electrodes) of the infinite periodic grating the results can be interpreted easily and the coupling to the applied voltage can be analysed directly. If q is the complex charge of the electrode driven by a voltage V, then the admittance Y is given by (Hofer *et al.* 2006),

$$Y = j\frac{q\omega}{V}, \tag{2.40}$$

where ω is the angular frequency.

The admittance magnitude curve obtained from the FEM model is depicted in Fig. 2.9. It can be observed that the resonant peaks in the admittance curve coincide well with the stopband edge frequencies obtained from the modal analysis. The resonance at the anti-symmetric SAW modal frequency, f_{M+}, is strong due to the constructively interfering eigenmodes. However, the resonant peak at the other edge of the stopband, f_{M+}, is weak due to the destructively interfering eigenmodes. The conductance and susceptance curves of the complex admittance are shown in Fig. 2.10.

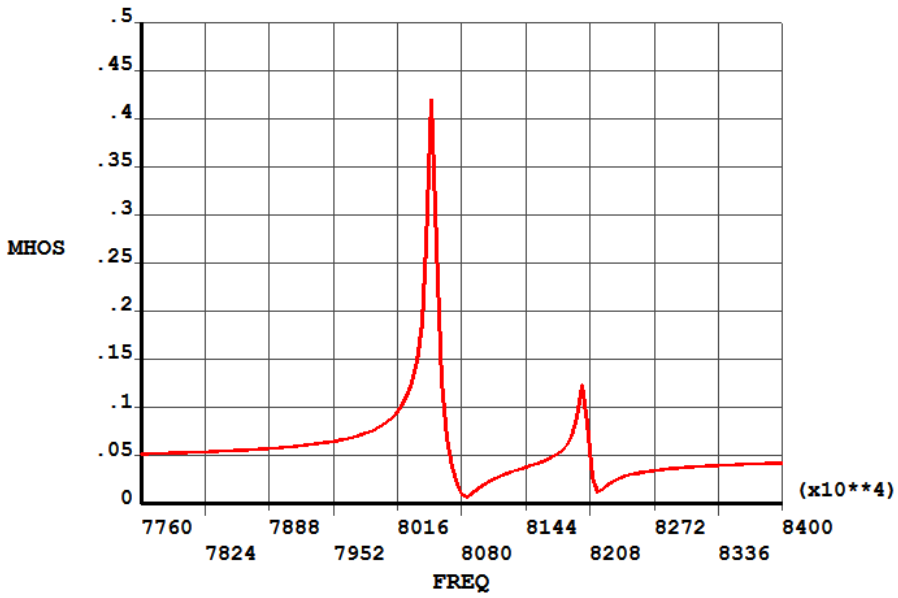

Figure 2.9. FEM computed admittance magnitude curve. The two resonant peaks determine the edge frequencies of the stopband.

2.7 Parameter Extraction

An idle test structure for COM/P-matrix parameter extraction is a synchronous one-port resonator with a large amount of IDT and reflector fingers. The simulation results discussed in the previous section are for such a structure where the influence of the end effects on the complex admittance due to the finite length of the structure is negligible. Moreover, Hofer *et al.* (2006) have validated the FEM computed admittance of a periodic structure with an experimental synchronous one-port resonator with 150 IDT fingers and 60 reflector fingers on either side of the IDT. A good agreement between the simulation and experimental results has been reported around the vicinity of the stop band. Hence, the FEM results of an infinite periodic grating was utilised to extract the complete set of COM/P-matrix parameters in this research. This is carried out by fitting the projection of the FEM analysis onto the set of field distributions predicted by the coupled-mode theory.

The parameters velocity and reflectivity can be derived from the knowledge of the stopband edge frequencies. As a result, Eqns (2.16) and (2.17) can be rewritten as

$$v = (f_{M-} + f_{M+})p, \tag{2.41}$$

$$\kappa_p = \pi \frac{f_{M+} - f_{M-}}{f_{M+} + f_{M-}}. \tag{2.42}$$

The obtained short grated stopband edge frequencies (f_{M+} & f_{M-}) from the modal analysis are substituted in Eqns (2.41) and (2.42) to extract the velocity and reflectivity parameters of the infinite periodic grating. The sign of the reflectivity κ_p determines the location of the symmetric and anti-symmetric SAW modes. All the other COM parameters can be determined from the characteristics of the complex admittance, which is a direct representation of the electrical admittance of the experimental test structure. For devices where the dominant propagating modes are complex waves such as leaky-SAWs and longitudinal leaky-SAWs, the velocity and reflectivity parameter vary with frequency. Therefore, the variation in the values of these parameters with respect to the frequency can be analysed using the derived complex admittance.

There are several curve fitting techniques available for parameter extraction from test structures. However, in this work, the technique used by Koskela *et al.* (1999) to determine the parameters of a periodic Green's function model was utilised to extract the parameters from the FEM computed results. This technique was chosen for it's versatility as it has been proven to be effective for parameter extraction from both simulated and physical structures. The complex admittance obtained from the harmonic analysis in the previous section corresponds to the particular solution (Eqn (2.18)) of the COM equations caused by the excited field. This admittance component (P_A^E), as shown in Eqn (2.29), dominates the total admittance response of the long synchronous one-port resonators considered here. This is because the contribution of the homogenous component of the admittance to the total response is negligible for an infinite periodic grating. So the total admittance for a periodic structure (Y_p) can be expressed as

$$Y_p = -j\frac{4\alpha^2\lambda_0}{\delta+\kappa}L + j\omega C_p. \tag{2.43}$$

The conductance (Y_r) and susceptance (Y_i) of the periodic structure obtained from the complex admittance using harmonic analysis is shown in the Fig. 2.10.

The resonant frequency f_R, given by

$$f_R = f_0(1 - \frac{\kappa_p}{2\pi}), \tag{2.44}$$

is the eigenfrequency of the short circuited electrodes, corresponding to the peak of the conductance $Y_{r\max}$ expressed as

$$Y_{r\max} \equiv Y_R(f_R) = \frac{4{\alpha_p}^2}{\gamma_p}. \tag{2.45}$$

Here the peak of the conductance is determined by the transduction coefficient and the attenuation. In the absence of attenuation, the quantity $Y_{r\max}$ would approach

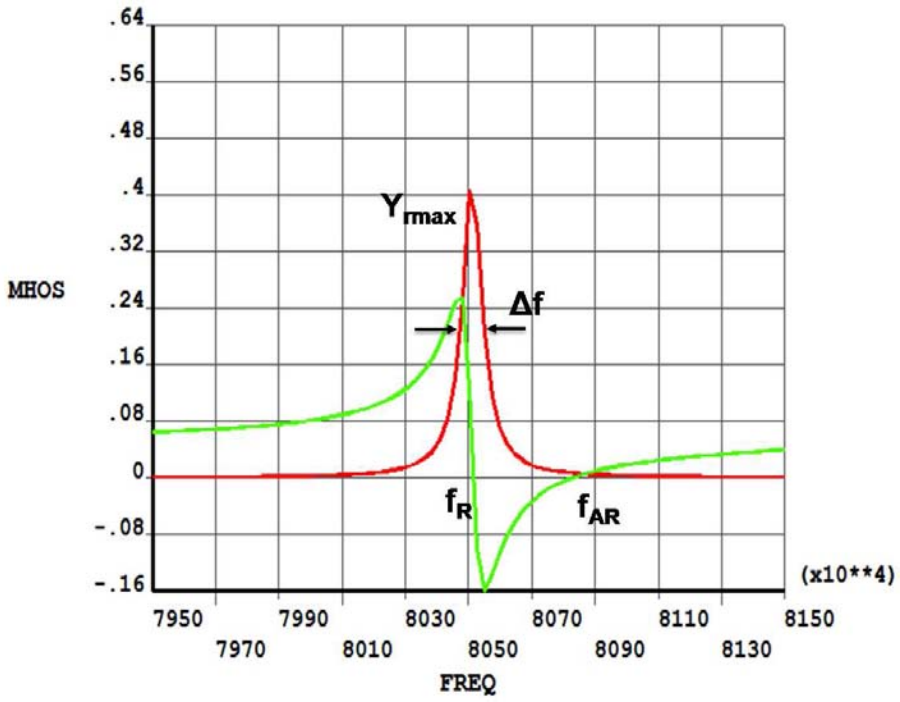

Figure 2.10. FEM computed admittance curve with real and imaginary parts at f_{M+} modal frequency.

infinity. As the numerical simulations of surface acoustic waves do not take the free surface attenuation into account, γ_p becomes zero. To overcome this drawback, a small damping ratio (0.0005) is interposed in FEM to have a finite value for γ_p. All other parameters are unaltered by the introduction of this minor attenuation. However, the insertion of this phenomenological attenuation is not required for LSAW and surface transverse wave (STW) devices due to the nature of the wave propagation. If Δf is the width of the real admittance peak at $Y_R = Y_{r\max}/2$ then

$$\Delta f = \frac{f_0 \gamma_p}{\pi}. \tag{2.46}$$

All the quantities in the Eqns. (2.44) - (2.46) are described by the information contained in the curve, and thus permit the extraction of the parameters: transduction coefficient α_p and attenuation γ_p. The conductance and the susceptance of the complex admittance can be expressed as:

$$Y_r(f) = \frac{Y_{r\max}}{4Q^2(f/f_R - 1)^2 + 1}, \tag{2.47}$$

$$Y_i(f) = -Y_{r\max}\frac{2Q(f/f_R - 1)}{4Q^2(f/f_R - 1)^2 + 1} + 2\pi f C_p. \tag{2.48}$$

where the quality factor Q is defined as $f_R/\Delta f$.

Table 2.2. COM Parameters of a resonator structure with 128° YX-cut $LiNbO_3$ piezoelectric substrate and gold electrodes for a MR of 0.45 and h of 3%.

Parameter	Current work	units
v	3574.56	m/s
κ_p	-0.0294	
α_n	53.7×10^{-5}	$\Omega^{-1/2}$
C_n	106.2×10^{-5}	pF/μm

The zero of Eqn (2.43) corresponds to the open-circuit grating condition at the anti-resonance frequency. As the imaginary part of the admittance crosses zero at the anti-resonance frequency f_{AR} the, Eqn (2.48) can be equated to zero to find C_p

$$C_p = \frac{Y_{\text{rmax}}}{2\pi f_{AR}} \times \frac{2Q(f_{AR}/f_R - 1)}{4Q^2(f_{AR}/f_R - 1)^2 + 1}. \tag{2.49}$$

All the COM/P-matrix parameters can be extracted by applying the above equations to the observed quantities in the admittance curve of Fig. 2.10. The extracted parameters for SAW on 128° Y-cut X-propagating $LiNbO_3$ with rectangular gold electrodes for a metallisation ratio (MR) of 0.45 and electrode thickness (h) of 3% are presented in the Table 2.2

These parameters can be utilised in conjunction with the COM/P-matrix models and matrix cascading techniques for designing various acoustic filters and resonators. The next step would to validate the structures modelled using these parameters with the physical devices, which will be discussed in the following section.

2.8 Experimental Validation of Extracted Parameters

An experimental validation of the above extracted COM/P-matrix parameters is feasible only with a structure with the material types, electrode geometry and dimensions as those of the FEM modelled infinite periodic grating. Hence, a delay line is fabricated with 128° Y-cut X-propagating $LiNbO_3$ piezoelectric substrate and gold IDTs using optical photolithographic techniques, explained in detail in the next chapter. A SEM image of the delayline with two identical IDT's is shown in the Fig. 2.11. Each IDT comprises of 20 finger pairs with a finger width of 10 μm and an aperture of 500 μm. The metallisation ratio (MR) and electrode thickness (h) are same as the FEM model

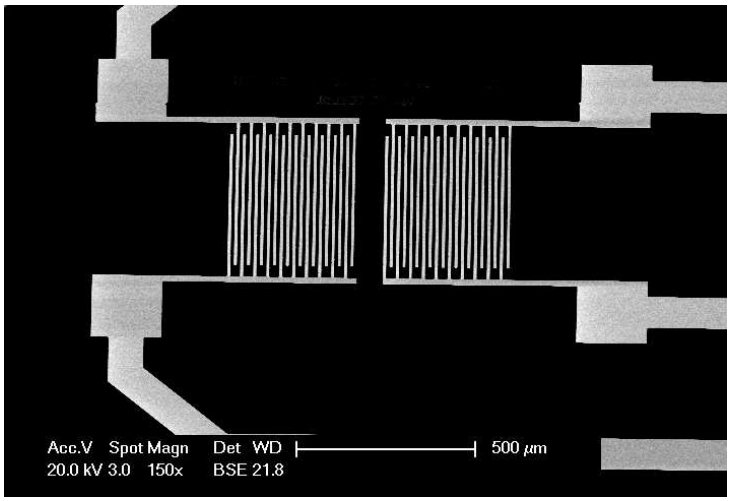

(a)

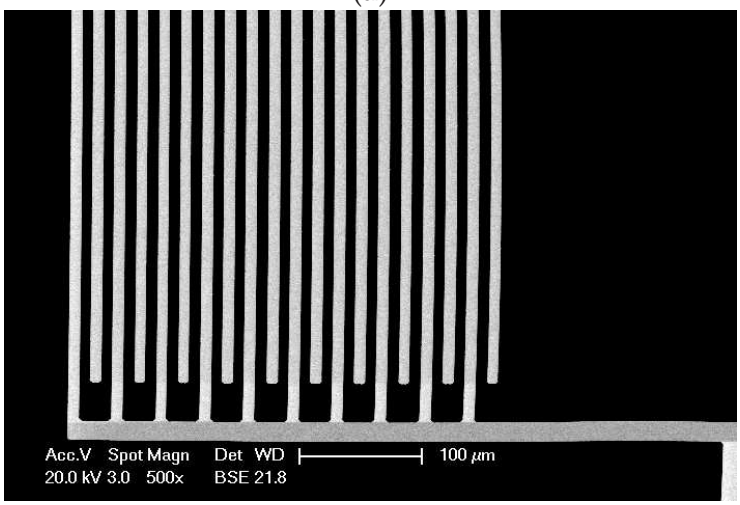

(b)

Figure 2.11. SEM photographs of (a) the complete SAW delayline with input and output IDTs. (b) a part of the IDT with 22 μm periodicity and 10 μm linewidth.

i.e. is 0.45 and 3% respectively. The input and output IDTs are seperated by a gap of 80 μm. The measured frequency response of the delayline filter is compared with the result obtained from the P-matrix method using the parameters extracted from the direct FEM simulations.

If the P-matrix elements, in Eqn. (2.20), with the superscripts i and o correspond to the input and output IDTs of the delayline respectively, then the total admittance response of the delayline is given by

$$A = \begin{pmatrix} A_{11} & A_{12} \\ A_{21} & A_{22} \end{pmatrix} \tag{2.50}$$

where

$$A_{11} = A^i_{33} + \frac{R^o_{11} I^i_{32} E^i_{23}}{1 - R^o_{11} R^i_{22}}, \qquad A_{12} = \frac{E^o_{13} I^i_{32}}{1 - R^o_{11} R^i_{22}}$$
$$A_{21} = \frac{I^o_{31} E^i_{23}}{1 - R^o_{11} R^i_{22}}, \qquad A_{22} = A^o_{33} + \frac{R^i_{22} E^o_{13} I^o_{13}}{1 - R^o_{11} R^i_{22}} \tag{2.51}$$

The insertion loss, S_{21}, of the delayline can be derived from the admittance response by (Wang *et al.* 2006)

$$S_{21} = \frac{-2A_{21}\sqrt{R_{\text{in}} R_{\text{out}}}}{(R_{\text{in}} + jS_1 + A_{11})(R_{\text{out}} + jS_2 + A_{22}) - A_{12}A_{21}}. \tag{2.52}$$

Here, the frequency response is influenced by the input (R_{in}) and output (R_{out}) resistances of the peripheral circuits and the susceptances S_1 and S_2 for impedance matching. A R_{in} and R_{out} of 0.4 Ω is incorporated in the P-matrix model to represent the resistances of the peripheral circuits. Furthermore, the small fabrication tolerances and the spurious capacitances are accounted for in the simulated model by the inclusion of a 2.5 pF capacitance.

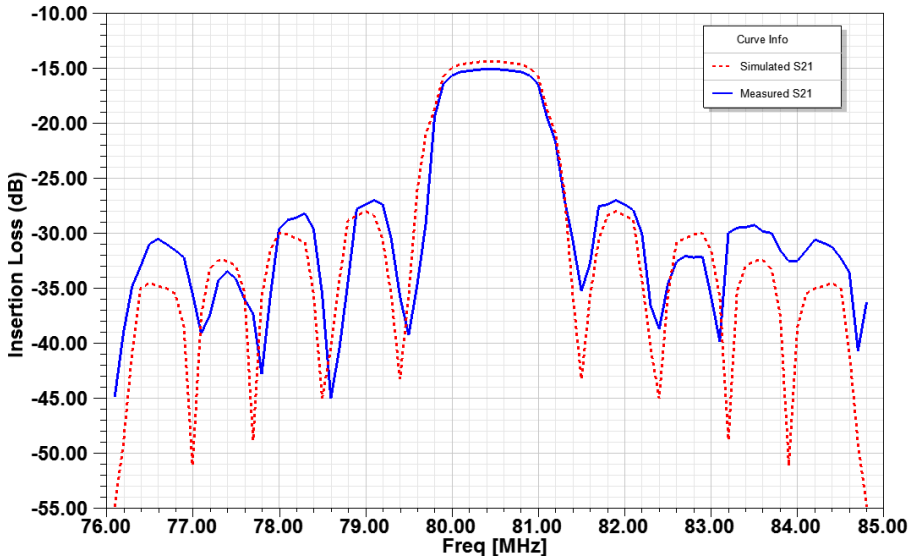

Figure 2.12. Simulated and measured frequency response of the delay line. Here, the P-matrix model of the delayline is simulated using the extracted parameters in Table 2.2

The COM parameters in Table 2.2 are substituted in Eqn. (2.51 - 2.52) to compare the insertion loss of the P-matrix model with the experimental measurement, as shown in the Fig. 2.12. The measured insertion loss of 15 dB, in the vicinity of the stopband frequency, is in good agreement with the simulation result. However, there are differences

between the simulated and measured values above and below the stopband frequencies due to the onset of spurious modes (Hofer *et al.* 2002). This spurious mode generation and scattering can be taken into account by modifying the COM model (Plessky and Koskela 2000). As the 128° Y-cut X-propagating $LiNbO_3$ piezoelectric substrate, used in the current work, is predominantly a Rayleigh wave material these modified versions of the COM model are not considered. However, they could be employed for devices where the primary propagating modes are LSAW or Bulk waves. Finally, the quantitative agreement between the theory and physical measurement is emphasised in the vicinity of the stopband.

2.9 Conclusion

Finite element analysis has emerged as an optimal approach for modelling SAW devices due to its versatility, reliability, ease of modelling complex geometries and automatic inclusion of second order effects. In this chapter, the use of this approach to extract the complete set of COM/P-matrix parameters from the FEM modelling of an infinitely long, synchronous, one-port resonator, which is considered an ideal structure for parameter extraction, was demonstrated. As the structure is modelled by considering the complete set of partial differential equations governing the electro-mechanical properties, with and without excitation, it is possible to analyse the freely propagating eigenmodes, eigenvalues, electrically active waves and electrical admittance. The COM/P-matrix parameters were extracted from the simulation results using a fitting technique. Furthermore, the aspect of experimental validation of these parameters was considered by fabricating a delayline filter with the same periodic dimensions and materials as that of the FEM modelled infinite periodic grating. The measured frequency response of the delayline filter was compared with the result obtained from the P-matrix model of the delayline designed using the extracted parameters. Thus, it can be concluded that the direct FEM facilitates the determination of SAW and LSAW parameters in a more rigorous, direct and realistic manner than any of the simulation techniques currently available. As an extension of the application of the direct FEM technique, the design and development of SAW correlators is presented in the next chapter (Chapter 3).

This page is blank

Chapter 3

Finite Element Method Modelling of SAW Correlator

3.1 Introduction

Surface Acoustic Wave (SAW) based devices, apart from being inherently rugged and reliable, can provide bi-phase coding and processing gain by varying electrodes geometry (Ostermayer 2001, Malocha *et al.* 2004, Moeller *et al.* 1999). Thus, they can be used as wirelessly interrogatable and completely passive devices in many hostile environments. A SAW correlator responds with a correlated peak to an interrogating signal that possesses the correct frequency and correct code. With the evolution of accurate fabrication processes in recent times these devices are increasingly being used in communication systems for code discrimination and sensing (Schmidt and Scholl 2000, Takeuchi and Yamanouchi 1995, Arthur 1996). However, the aspect of employing SAW signal correlation for wireless powering of actuators in a secure manner has not been fully investigated. The concept of using a SAW correlator for improving the security and actuation of the wireless controlled microvalve will be discussed in the next chapter. Such applications can dramatically benefit from the development and implementation of correlators with low insertion loss. Moreover, precise characterisation of acoustic mode propagation determined by the encoded code sequence, device geometry and material characteristics is crucial for designing a SAW correlator. Until now, a considerable amount of effort for acoustic wave correlator characterisation was focused heavily on experimentation, fabrication and processing. The dependence on fabricated test structures can be reduced considerably if the design optimization and mode propagation characterisation of the device is carried out accurately using simulation tools. The existing modelling approaches, mostly based on

the delta function and equivalent circuit models are currently being employed to optimize the design process (Brocato 2004, Lee *et al.* 2002, Yu 2004). The reduction in computational time of these models is at the expense of assumptions or simplifications that are often invalid for practical designs. This results in the negligence of the second order effects such as backscattering, diffraction, charge distribution and mechanical loading (Matthews 2007, Xu 2000). Moreover, these approaches do not provide a comprehensive analysis of the correlators response, determined by variable structural dimensions and material types.

Finite element analysis is an attractive technique, which comes closest to comprehensive modelling of a complete acoustic correlator with minimal assumptions. Field theory is the most appropriate approach for designing SAW devices as it involves the resolution of all the partial differential equations for a given excitation (Hofer *et al.* 2006). The finite element method (FEM) allows for accurate representation of field theory where the piezoelectric behaviour of the SAW devices is discretised and numerically solved in the frequency and time domain. The use of finite element techniques for predicting the response of a complete device is still in its infancy. This is mainly due to the huge constraints placed on the computational resources. Hence, the FEM modelling of SAW devices was previously limited to either periodic structures or simple IDT structures with a few electrodes (Wu and Chen 2005, Le Brizoual *et al.* 2006, Ippolito *et al.* 2003). However, with the availability of software packages with large node handling capability and the growing need to account for the impact of the majority of the second order effects on the device response, under variable boundary and load conditions, the use of FEM for numerical simulation of a SAW correlator appears to be efficient.

Shear horizontal and other higher order mode characterisation using FEM has been well addressed, in the past using small models (Sankaranarayanan *et al.* 2007, Hofer *et al.* 2002, Makkonen *et al.* 2006). However, quantitative understanding of the effect these modes have on the processing gain and the electromechanical coupling of a full scale acoustic device did not garner wide spread acceptance in FEM. This can be attributed to the predominant use of Rayleigh mode for SAW devices. However, the increasing demand for ultra high frequency devices has generated a renewed interest for the characterisation of higher order modes. This interest combined with the availability of powerful computational resources at reasonable cost have made it possible to model a complete SAW correlator by neglecting features that contribute diminutively to the

final output. In this chapter, the modelling of a 2 and 3-dimensional, 5×2-bit Barker sequence encoded acoustic wave correlator using a direct finite element model, previously employed for the analysis of surface acoustic waves and extraction of COM/P-matrix parameters, is demonstrated. The investigation of the effect shear horizontal wave component has on the performance of a 5×2-bit Barker sequence encoded correlator is carried out through 3-D modelling. The correlator's response can be quantified in terms harmonic analysis to obtain, the electrical admittance, output voltage profile, and transient analysis to study the acoustic wave propagating characteristics and correlation pulses. Also, the dynamic responses of the device (such as displacement, and electric potential) when interrogated by different coded signals are examined and presented as a function of frequency. It should be emphasized that while the objective of this research is to achieve finite element modelling of an acoustic wave correlator, it approaches the objective from a design optimization viewpoint. That is, the aim is to determine how the dimensions, materials and harmonic acoustic modes influence the device response, and subsequently use those results to optimise the response. The validation of the simulation results is carried out by fabricating the SAW correlators using optical lithographic technique. A good agreement between the numerical and experimental results highlights the feasibility and potential of using FEM for application specific modelling of SAW correlators.

In this Chapter, modelling of a 2 and 3-dimensional, 5×2-bit Barker sequence encoded acoustic wave correlator is presented using FEM. In Section 3.2, the SAW correlator operation, the various pulse compression coding schemes and signal processing functionality of the correlator are discussed. The various correlator modelling approaches are described in Section 3.3. Then in Section 3.4, the FEM SAW correlator design including the dimensions of the structure, materials used, and boundary conditions are discussed. After the description of the fabrication process flow in Section 3.5, both the simulation and experimental results are discussed in Section 3.6. This includes the harmonic analysis, transient analysis, the investigation of shear horizontal wave component and mismatched code correlator response.

3.2 SAW Correlator

SAW filters and sensors have been widely researched over the past few decades as they offer many advantages including reliability, high filter selectivity, robustness, wireless,

passive operation and facilitate large-volume production. Furthermore, SAW devices do not require any DC power and there is no junction voltage to overcome as in RFID tags and semiconductor electronics. While the senors are being used for measuring physical, chemical and biological quantities in harsh environments the filters are predominantly being utilised in consumer electronics such as mobile phones and televisions. The application domain of one type of SAW filters, the SAW correlators, is not as wide as the other embodiments such as delaylines and resonator-based filters. This could be attributed to the lack of accurate fabrication techniques required for the mass production of these devices operating at GHz frequencies. Moreover, the programmability of the SAW correlators is arduous due to the predetermination of the code in the manufacturing stage and hence do not lend themselves for commercial acceptance. However, these drawbacks have been addressed recently with the advent of piezoelectric substrates with high electromechanical coupling coefficients, advanced lithographic techniques and programmable SAW correlators (Brocato *et al.* 2003, Kosinski 2000).

The basic functionality of a SAW correlator is similar to a digital correlator i.e. to recognise a coded signal. However, a SAW correlator differs from its digital counterpart by being a passive device. Also, it has the capability to undertake complex signal processing functionalities, normally performed by several subsystems of a conventional radio system, in a small space. The small size is plausible due to wavelength compression which is a result of the very short wavelengths of the acoustic waves. Moreover, it can be used both in transmission and reception modes to generate and decode, respectively, complex, broadband, bi-phase coded microwave signals.

A SAW correlator, as shown in Fig. 3.1, is a passive pulse compression filter that operates through the correlation of phase shifts in the transmitted RF signal. It consists of an input IDT and a coded output/compressor IDT deposited on top of a piezoelectric substrate. The input IDT transduces the coded input RF signal into an acoustic wave. The electrodes of the output/compressor IDT are phase coded during construction in such a way that the correlator converts the correctly phase coded acoustic wave to a RF modulated electrical pulse. Thus, the output IDT performs both the signal processing and transduction functions. The code embedded in the output IDT is reflected from the polarities of finger pairs which is in turn determined by the way in which these finger pairs are connected to the two summing bars or bus bars. As the acoustic wave propagates through the output IDT the phase of each finger pair is summed in or

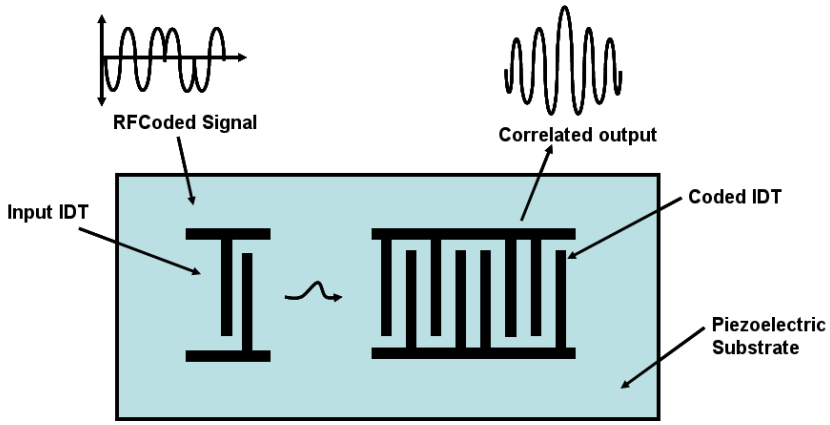

Figure 3.1. Surface acoustic wave correlator with a input IDT and a coded output IDT. After the input IDT converts the phase coded RF signal into a coded acoustic wave, the output IDT transduces the wave back to a RF modulated electrical pulse when there is code match.

out of phase with the acoustic wave. The device will respond with a correlation peak only when the code of the interrogating RF pulse matches with the embedded code in the output IDT, thus enhancing the processing gain of the correlator by combining the code reception scheme with the high Q operation of a bandpass filter (Brocato 2004). For all other transmitted signals with different codes, even the one's excited at the same frequency, the correlator would respond with a pseudo-random noise. The coding scheme used in this work is Binary Phase Shift Keying (BPSK), where the incoming radio wave has 180° phase transitions in its waveform. BPSK was chosen because it offers a simplest form of phase coding and an optimum signal-to-noise ratio. By converting the long input BPSK signal with a matched pattern into a short RF modulated pulse, the correlator can provide considerable process gain.

A coded SAW based communication system, as shown in the Fig. 3.2, consists of an expander IDT in the transmitter and a compressor IDT in the receiver. A narrow pulse or a sinusoidal waveform is fed to the expander IDT to generate a coded acoustic signal depending on the geometry of the expander IDT. The acoustic waves propagate through the substrate to the transmitting IDT, which transforms these coded acoustic waves to electrical coded RF signals. The output from the transmitting IDT is fed to an amplifier, to strengthen the signal, and then to a transmitting antenna. The receiver consists of a correlator, operating as discussed above, with its input IDT connected to a receiving antenna to intercept the transmitted coded RF signal. To ensure efficient reception and processing of the RF signal the transmitter and the receiver antennas are

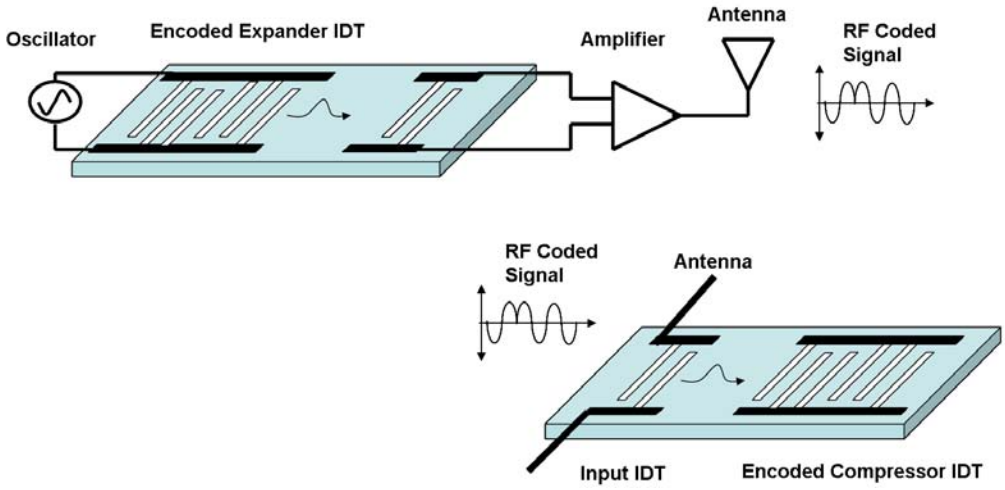

Figure 3.2. SAW correlator transmitter receiver configuration. The transmitter generates a RF coded signal that triggers the receiver when there is code match.

tuned to the centre frequency of the correlator. The optimum transmitter power (P_t) is governed by the application and therefore is influenced by factors such as the the correlator insertion loss (S_{21}) and separation between the transmitter and the receiver (R_{rt}). This power can be estimated from the radar range equation given by (Brocato 2004)

$$R_{rt} = \frac{\lambda}{4\pi} \sqrt[4]{\frac{P_t G_t^2 G_r^2}{S_{21}^2 . \text{SNR}. K\, T_C\, B\, F_N}} \tag{3.1}$$

Here, G_t and G_r are the gains of the transmitting and receiving antennas, λ the wavelength, SNR the signal-to-noise ratio, K the Boltzmann's constant, T_C the receiver temperature, B the signal bandwidth and F_N the noise figure.

The expander in the transmitter is an exact replica of the compressor/coded IDT of the correlator. The coding of the expander and compressor determines the correlation function performed by the correlator. The coding schemes that can be used for SAW correlators are discussed next.

3.2.1 Coding Schemes

As part of the SAW correlator design there is a need to consider the various the pulse compression coding techniques that facilitate a unique activation of the device with good signal-to-noise ratio (SNR). The time-bandwidth product of TB determines the effectiveness of a particular code, where B is the pulse bandwidth and T is the pulse

duration. The BT for a simple un-coded pulse is 1, since B=1/T (Sato and Shinriki 2000). In this section a few code sequences that can be employed for the correlator design are outlined.

Barker sequence

The Barker sequences are a group of binary codes that have a correlation function such that the peak response is N times higher than at all other times (N is the length of the sequence) (Campbell 1998). The resultant response when a 5-bit Barker code is delay tapped and summed with the time reversed code of same order is shown in the Fig. 3.3.

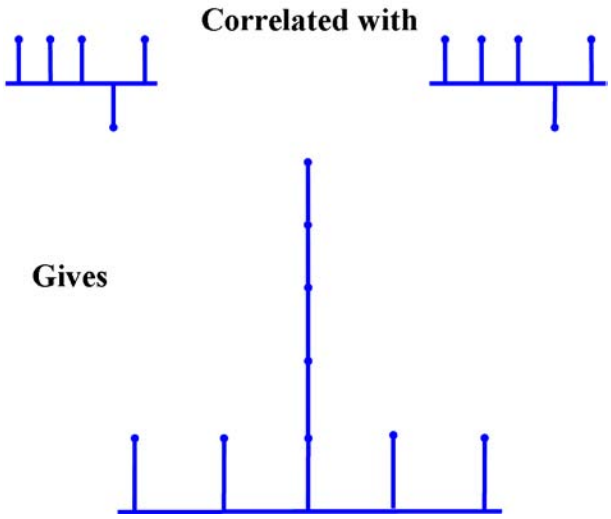

Figure 3.3. The correlation result of a length 5 Barker sequence. As can be seen, when the signals completely overlap, the result is much greater than at all other points.

True Barker sequences are only known to exist up to a length of 13 (Table. 3.1), however if a longer length is required, multiple sequences can simply be concatenated to form a combined or binary weighted Barker sequences (Campbell 1998). For example, a 35-bit code could be constructed by combining a 5×7 sequence. As the order of the code matters, a 5×7 code is different to a 7×5 code, thus allowing many different codes to be constructed for different devices with a significant decrease in the possibility of code reuse. Now, consider the correlation when there is a one bit error in the input signal, as shown in Fig. 3.4. In this case, the peak magnitude is not as high when the codes match this would prevent the triggering of the correlator from spurious signals.

Table 3.1. Known Barker code sequences

Sequence length, N	Sequence
2	+ + or + -
3	+ + -
4	+ + - + or + + + -
5	+ + + - +
7	+ + + - - + -
11	+ + + - - - + - - + -
13	+ + + + + - - + + - + - +

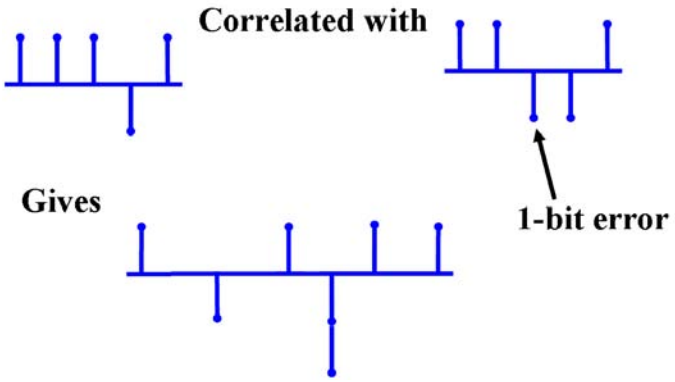

Figure 3.4. The correlation result of a length 5 Barker sequence, where the input signal has a 1-bit error. The peak magnitude is not as high as in previous figure when the sequences match.

Maximum length sequence

One more sequence that can be encoded in the correlator is a pseudo-random binary sequence called the maximum length sequence (MLS). These sequences can be obtained from the linear feedback shift register. The number of stages of the shift register n determines the length of the MLS, N, as $N = 2^n - 1$. The Table. 3.2 lists the length and number of maximal length sequences obtained from shift registers with 2-5 stages.

MLS's are suitable for SAW correlators with long code sequences as there is no limitation on the length of the code. An MLS signal comprises of an approximately equal number of 0s and 1s. The peak-to-sidelobe ratio of MLS is $\sqrt{4N}$. A flat frequency spectrum for all frequencies up to the Nyquist frequency ensures a high signal-to-noise ratio (Kemp 2002). The cross-correlation function reduces the background noise and hence the correlator can be used in noisy environment.

Table 3.2. Maximum length sequences

Number of stages, n	Length of maximum sequence, N	Number of maximum sequences, M
2	3	1
3	7	2
4	15	2
5	31	6

Table 3.3. Golay sequences

Sequence length, N	Sequence	Amplitude of the main peak
2	+ + or + -	4
4	+ + - + or + + + -	8
8	+ + + - - - + -	16
13	- - + - - - - + - + + + - + - - or - - + - - - - + + - - - + - + +	32

Golay sequence

Golay complementary sequences are pairs of binary codes, where the number of pairs of similar elements with any given separation in first series is equal to the number of unlike elements pairs with the same separation in the second series. It consists of two codes of the same length N whose auto-correlation functions have side-lobes equal in magnitude but opposite in sign (Nowicki *et al.* 2004). The peak of the auto-correlation function when both the codes are summed up is $2N$ with no side-lobes. Although these codes may seem to represent the ideal solution to the side lobe suppression problem they are not appropriate for SAW correltors with high bit rate as the maximum length of the code is limited to 16. The longest Golay code has a peak-to-sidelobe ratio of 32.

All the above discussed code sequences provide a high signal-to-noise ratio and good side lobe suppression. The combined Barker sequence, which allows concatenation of basic sequences to form a larger sequence, is employed in the current research for correlator FEM modelling.

3.2.2 Signal Correlation

A correlator also known as a pulse compression filter correlates the input signal with a stored replica. In the frequency domain, compression involves manipulating the phases of the different frequency components of the pulse. Binary phase coding is a way of pulse compression where the phase of the radio frequency signal is repeatedly flipped according to the binary code within the duration of the pulse. The code selectivity of the devices is attained by correlating the received signal with a replica of the stored code. By doing so it is possible to consider the transmitting signal with narrow pulse widths without compromising the receiver bandwidth requirements. Thus, the transmission power levels can be kept under permissible limits. In the case of a SAW correlator, the stored replica is encoded in the IDT, as shown in the Fig. 3.5. The length of the transmitted sequence and the efficiency of the compression algorithm determine the output filter signal-to-noise ratio, which is commonly referred to as processing gain.

In order to study the signal processing functionality of the SAW correlator the following terms are defined (Bracato 2004, Abramov 2005):

t	=	time
f_c	=	centre frequency of the filter
N_B	=	number of binary bits encoded in the IDT
T_B	=	N_B / f_c = bit time of the filter
f_B	=	1 / T_B= bit rate of the filter
a_o	=	1,1,1,-1,1 = BPSK input code (e.g. 5-bit Barker sequence).
b_o	=	1,-1,1,1,1 = time reversed input code encoded in the IDT (e.g. 5-bit Barker sequence).
$u(t)$	=	a unit step function

The BPSK coded input signal represented by a phase varying sine wave is given by

$$V_{ip}(t) = \sin(2\pi f_c t) \sum_{x=1}^{N_B} a_0[u[t-(x-1)T_B] - u(t-xT_B)]. \tag{3.2}$$

The input IDT transduces the BPSK signal into an acoustic wave. The impulse response of the input IDT is

$$C_{ipIDT}(t) = \sin(2\pi f_c t)(u(t) - u(t-T_B)). \tag{3.3}$$

The input BPSK signal is modulated by the bit sequence b_o, a reverse of the input signal code a_o, encoded in the output IDT. The output IDT serves as a pulse compression filter

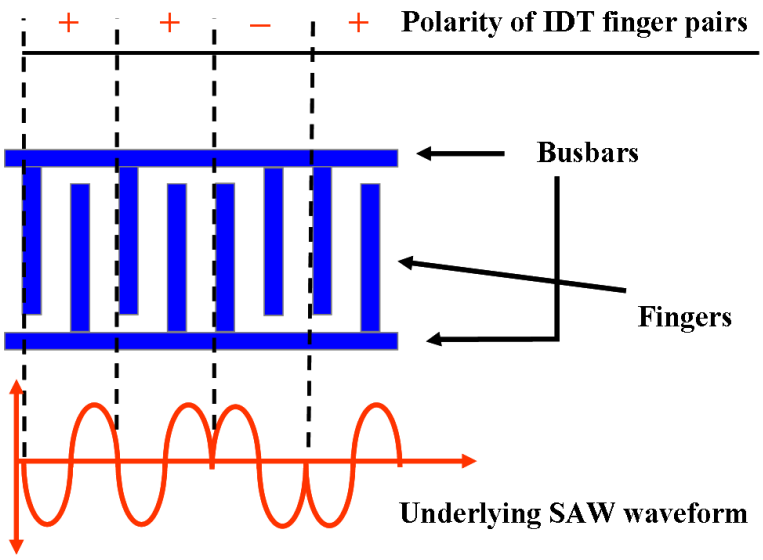

Figure 3.5. Basic structure of the coded interdigital transducer showing relative polarity of finger pairs and the underlying SAW waveform.

to the input BPSK signal. The impulse response of the compressor/output IDT is given by

$$C_{opIDT}(t) = \sin(2\pi f_c t) \sum_{x=1}^{N_B} b_0[u[t-(x-1)T_B] - u(t-xT_B)]. \tag{3.4}$$

The electrical input signal, $V_{ip}(t)$ must pass through the input IDT to be converted into an acoustic waveform. The convolution operation represents the excitation of the SAW correlator by the input signal $V_{ip}(t)$, hence the generated acoustic wave can be written as

$$AC_{op}(t) = \int_0^t V_{ip}(\tau) C_{ipIDT}(t-\tau) d\tau. \tag{3.5}$$

The convolution of the acoustic wave with the impulse response of the compressor IDT gives the electrical response (R_C) of the correlator.

$$R_C(t) = \int_0^t C_{opIDT}(\tau) AC_{op}(t-\tau) d\tau. \tag{3.6}$$

When the transmitted code, a_0, is received by the SAW correlator a correlated peak with high signal to noise ratio is produced.

3.3 SAW Correlator Modelling Techniques

Modelling of SAW correlators is not as straightforward as modelling other commonly used SAW devices due to non-periodic nature of the device and the large problem

domain. Hence, it cannot be carried out with the same basic software tools that are commercially available for modelling SAW filters and resonators. To aid the correlator design process a few modelling techniques were developed (Brocato 2004, Campbell 1998, Hashimoto 2000). The underlying assumptions, abilities and pitfalls of these techniques, eventually leading to the novel finite element method modelling of correlators, will be discussed below.

3.3.1 Delta Function Modelling

In the delta function modelling of the correlator, each electrode of the IDT is treated as a delta function source. The resultant response of the device is obtained by summing the delta sources with respect to the applied voltage. As the correlator is considered as an ideal mathematical element it does not provide an accurate frequency domain characteristics. The model only provides a general understanding of the advantages and disadvantages of different code sequences through the normalised output amplitude plots (Brocato 2004, Campbell 1998). The transfer function of a SAW correlator comprising of input and output IDTs with transfer functions $|H_i(f)|$ and $|H_o(f)|$, respectively, is given by

$$|H(f)| = |H_i(f)|.|H_o(f)|, \tag{3.7}$$

where

$$|H_i(f)| = \sum_{-a}^{a}(-1)^a W_a e^{-j\beta x_a} \tag{3.8}$$

and

$$|H_o(f)| = \sum_{-b}^{b}(-1)^b W_b e^{-j\beta x_b}. \tag{3.9}$$

Here, a and b are the number of electrodes, W_a and W_b are the weighing factors related to the finger pair overlap, for input and output IDT's respectively. Also, x_a and x_b are the distances from the center of the IDTs. The phase contribution of each electrode and therefore the binary code in the IDT is determined by the term $e^{-j\beta x}$. Where, β is the propagation constant. A 13-bit Barker sequence encoded SAW correlator's responses is calculated, as shown in Fig. 3.6, using the delta function model developed by Brocato (2004).

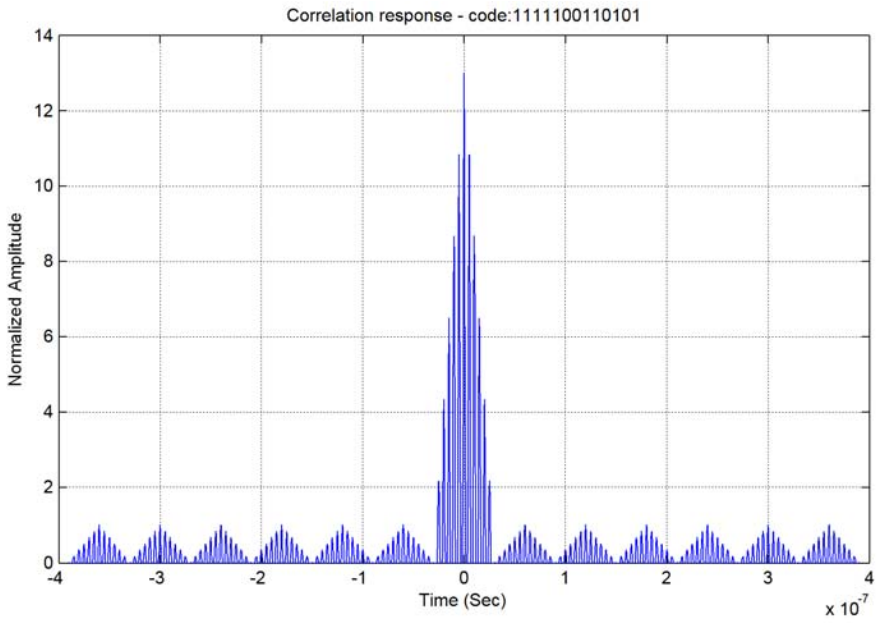

Figure 3.6. A 13-bit Barker sequence SAW correlator's response using delta function model. The normalised amplitude plot provides a qualitative description of the peak-to-sidelobe ratio, which in this instance is 13.

As this model relies on simplistic approximations, it is incapable of considering the bulk wave interferences, IDT admittance, diffraction, effects of energy removal, wave diffraction and harmonic response of the device (Kino 1987). The perturbation of the acoustic wave when it impinges on the IDT, mass loading, wave attenuation due to circuit loading, and bi-directional acoustic wave propagation are disregarded due to the negligence of acoustic path effects. Moreover, the optimization of the processing gain of the correlator through the variations of the structure geometry and electrode material is not feasible. Furthermore, this technique does not facilitate the investigation of the correlator's response for variable acoustic modes.

3.3.2 Equivalent Circuit Modelling

In the equivalent circuit modelling approach of SAW correlators each finger pair of the IDT is considered as a three port model with two acoustic ports and one electric port. The two acoustic ports and the acoustic effects caused by these ports are simulated using transmission delayline elements. The excitation and detection of the acoustic waves is performed by the electrical port. The EM signal propagation in the transmission line is employed to replicate the behaviour of the acoustic wave propagation.

The impedance variation of the transmission line facilitates the modelling of an acoustic wave propagation both on the free surface and metallized area of the piezoelectric substrate. Here, the electrical voltages and the excitation currents are considered as acoustic forces and acoustic velocities respectively. The equivalent circuit of the whole SAW correlator is formed by cascading the equivalent circuits of the individual finger pairs. An equivalent circuit model of a SAW correlator, driven by a voltage source V_S with source impedance Z_S and load impedance Z_L, is depicted in the Fig. 3.7.

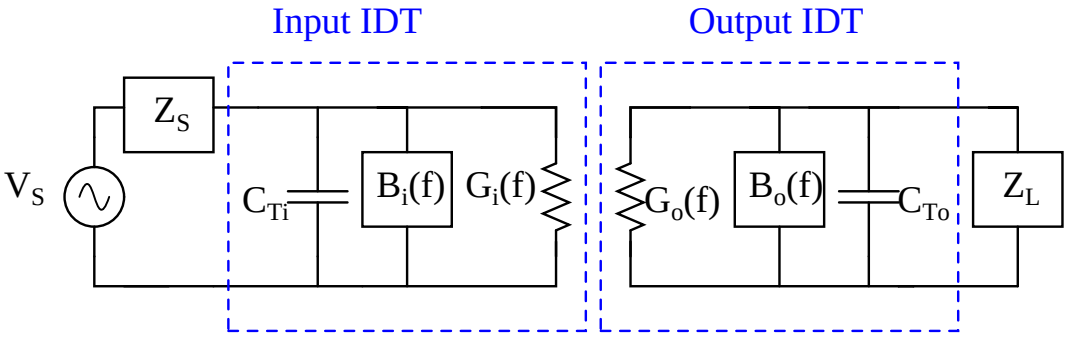

Figure 3.7. Equivalent circuit model of a SAW correlator. The acoustic force and acoustic velocity is represented by the electrical voltage and the excitation current, respectively.

Here, C_{Ti} and C_{To}, $B_i(f)$ and $B_o(f)$, $G_i(f)$ and $G_o(f)$ represent the total capacitance, acoustic susceptance, and radiation conductance of the input and output IDT, respectively. The model provides the transient response and the peak to side lobe ratio of the correlator. The admittance of each IDT can be expressed as

$$Y_x(f) = G_x(f) + j(2\pi f C_{Tx} + B_x(f)). \tag{3.10}$$

Where, x corresponds to either i or o for input and output IDT, respectively.

The equivalent circuit model is a cross field model where the electric field lines are considered to be normal to the piezoelectric substrate surface. It can be quite complex to incorporate the effects of diffraction, backscattering, charge distribution and electrical/mechanical perturbations in the model (Brocato 2004, Yu 2004, Atashbar *et al.* 2004). The electrode discontinuities and thereby the variations in the electrical loading caused by the impinging phase modulated acoustic waves is crucial for pulse compression operation of the SAW correlator and hence cannot be compromised with simplified assumptions. Apart from the frequently used Rayleigh waves, leaky waves or surface transverse waves are much more difficult to describe with this analytical technique.

Though, these simulations are computationally intensive, due to the non-parallel nature of the model components, they do not determine the effect of higher order modes on the performance of the correlator. Moreover, it is hard to optimise the output response of the device for variable structural dimensions and complex geometries.

3.3.3 Finite Element Method Modelling

All the SAW correlator modelling techniques discussed previously provide only an abstract insight into the analysis of certain design aspects of the device such as normalised amplitude response and relative peak-to-sidelobe ratio. However, for the comprehensive investigation of the behaviour of the correlators in the frequency and time domains, the full scale modelling of these structures is demanded. The modelling of a SAW device is mathematically equivalent to the resolution of the partial differential equations of piezoelectricity for a given excitation. FEM is one of the most accurate methods for the full scale modelling of a SAW device where the complete set of partial differential equations is solved (Hofer *et al.* 2006). This versatile technique automatically takes into account the effects of piezoelectric perturbation, mechanical perturbation, diffraction, backscattering, energy storage caused by non-radiating bulk waves, and electric flux leakage from the substrate surface (Hasegawa *et al.* 2001, Xu 2000). Moreover, due to the strong dependence of correlator performance on the electrode pattern, the second order effects, material type of the electrode/substrate and the operating frequency, FEM provides a realistic prediction of the complex structures response subject to a RF coded signal excitation.

It is important to examine the constituent partial differential equations that are descritized in FEM for SAW device modelling. This is to assists in understanding the final operational environment and the degrees-of-freedoms (DOFs) of the design. The analysis is commenced from the consideration of the piezoelectric effect in the substrate, which embodies the coupling between electrical and mechanical domains. The acoustic wave propagation in the piezoelectric media is governed by the mechanical equations of motion and Maxwell's equations for the electrical behavior given by (Hashimoto 2000, Campbell 1998)

$$T_{ij} = c^{E}_{ijkl} S_{kl} - e_{kij} E_k, \tag{3.11}$$

$$D_i = e_{ikl} S_{kl} + \varepsilon^{S}_{ik} E_k. \tag{3.12}$$

Here, T_{ij} is the components of stress, D_i the electric displacement, e_{kij} the piezoelectric constant, ε_{ik}^S the permittivity for constant strain, c_{ijkl}^E the stiffness constant for constant electric field, E_k the electric field intensity and S_{kl} the strain tensor given by

$$S_{ij} = \frac{1}{2}(\frac{\partial u_i}{\partial x_j} + \frac{\partial u_j}{\partial x_i}). \tag{3.13}$$

The negligible effect of magnetic fields on the SAW devices and the low velocity of acoustic waves compared to the EM waves, which in turn leads to quasi-static condition, reduce the Maxwell's equation to

$$E = -\nabla\phi, \qquad \text{and} \qquad \nabla.\mathrm{D} = 0. \tag{3.14}$$

Furthermore, the absence of internal body forces reduces the mechanical equation of motion in Eqn. (3.11) to

$$\frac{\partial T_{ij}}{\partial x_j} - \rho\frac{\partial^2 u_i}{\partial t^2} = 0, \tag{3.15}$$

where ρ is the density.

By substituting the conditions in Eqns. (3.13-3.15) back in the piezoelectric equations of Eqn. (3.11 & 3.12) results in a system of coupled wave equations given in Eqn. (2.34 & 2.35) and repeated here for the sake of clarity.

$$c_{ijkl}^E\frac{\partial^2 u_k}{\partial x_j\partial x_l} + e_{kij}\frac{\partial^2\phi}{\partial x_k\partial x_j} = \rho\frac{\partial^2 u_i}{\partial t^2}, \tag{3.16}$$

$$e_{ikl}\frac{\partial^2 u_k}{\partial x_i\partial x_l} - \varepsilon_{ik}^S\frac{\partial^2\phi}{\partial x_i\partial x_k} = 0. \tag{3.17}$$

This system of coupled wave equations comprises of an electric potential term and three displacement components in all directions, which are descretized in the form of nodal DOF's (Eqns. (2.36 & 2.37)) in FEM.

The dynamic system of linear piezoelectricity in the SAW devices, corresponding to the time steps 0 and 1, is obtained from the structural solution equation by assembling all the equations of individual elements (Lim 2003), given by

$$F_1 = [M]\frac{\partial^2 u_i^1}{\partial t^2} + [C]\frac{\partial u_i^1}{\partial t} + [K]u_i^1, \tag{3.18}$$

such that

$$\begin{pmatrix} M & 0 \\ 0 & 0 \end{pmatrix}\begin{pmatrix} \frac{\partial^2 u_i}{\partial t^2} \\ \frac{\partial^2 v_i}{\partial t^2} \end{pmatrix} + \begin{pmatrix} C & 0 \\ 0 & 0 \end{pmatrix}\begin{pmatrix} \frac{\partial u_i}{\partial t} \\ \frac{\partial v_i}{\partial t} \end{pmatrix} + \begin{pmatrix} K & K_p \\ K_p^T & K_d \end{pmatrix}\begin{pmatrix} u_i \\ v_i \end{pmatrix} = \begin{pmatrix} F \\ L \end{pmatrix}. \tag{3.19}$$

Where, F is the mechanical force, L the applied electrical loads, v_i the nodal electric potential vector, $[M]$ the mass matrix, $[K]$ the elastic stiffness matrix, $[K_p]$ the piezoelectric coupling matrix, $[K_d]$ the dielectric matrix, and $[C]$ the damping matrix of the piezoelectric substrate. These matrices are determines by the material properties and the boundary conditions of the model. A direct integration method called Newmark method (Moaveni 2007 (3^{rd} Edition), ANS 2008) is employed in FEM to define the velocity and displacement in Eqn. (3.18) as

$$\frac{\partial u_i^1}{\partial t} = \frac{\partial u_i^0}{\partial t} + \Delta t[(1-\psi)\frac{\partial^2 u_i^0}{\partial t^2} + \psi\frac{\partial^2 u_i^1}{\partial t^2}], \tag{3.20}$$

$$u_i^1 = u_i^0 + \Delta t\frac{\partial u_i^0}{\partial t} + \Delta t^2[(\frac{1}{2}-\xi)\frac{\partial^2 u_i^0}{\partial t^2} + \xi\frac{\partial^2 x_i^1}{\partial t^2}]. \tag{3.21}$$

Here, the parameters ψ and ξ determine the unconditional stability and second-order accuracy of the system.

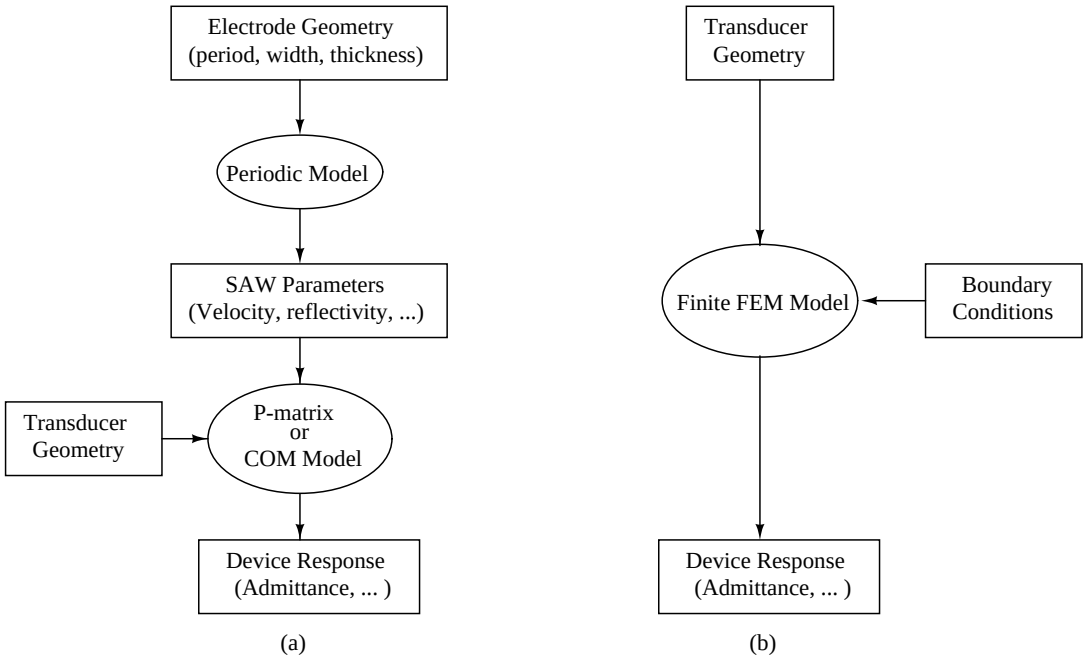

Figure 3.8. The two FEM SAW device modelling approaches for infinite periodic structures (a) and finite structures (b).

The FEM modelling of complete SAW devices can be classified into two approaches. The first approach, shown in Fig. 3.8.(a), considers a structure with infinite periodic gratings, often refered to as periodic structure. This approach focuses on the extraction of the acoustic wave propagation parameters such as velocity, electromechanical coupling coefficient and capacitance, from the FEM simulation results. These parameter

are utilised in phenomenological models like Coupling of Modes (COM) and P-matrix to model the whole device. The first approach was employed in the previous chapter for the modelling of a SAW delayline from the FEM extracted COM/P-matrix parameters. Although this approach is less time consuming and requires fewer computational resources, it is not suitable for non-periodic structures such as SAW correlators. This is because the effects of phase changes and there by the additional reflections and scattering of acoustic waves is beyond the scope of the COM/P-matrix model. Moreover, the influence of SAW-BAW conversions at the device discontinuities and higher order spacial harmonics on the device characteristics is not considered with the current approach. An alternative approach, shown in Fig. 3.8.(b), uses a finite model, based on a low level of physical abstraction. Here, the FEM simulation of a complete SAW device is carried out from the knowledge of its geometrical characteristics and material properties. This approach evaluates the influence of the excitation source on the response characteristics of the complete acoustic wave device. The modelling of SAW correlators in the current research is carried out using the second approach.

Historically, the use of direct FEM for SAW device modelling was limited to infinite periodic gratings as has been discussed in the previous chapter. However, with growing emphasis on the accurate characterisation of the effect of higher order modes and second order effects on the performance of the whole device combined with the advent of fast computers with high storage and computational capabilities the focus, over the past few years, has shifted to the use of FEM for finite transducer structures. This approach has the capability to perform a full scale, accurate simulation of a whole SAW device for any set of feasible material types and loading conditions. Moreover, the versatility of this approach facilitates the simultaneous resolution of all the second order effects for both two and three-dimensional models.

The finite transducer FEM modelling approach has been previously employed by Xu (2000) to study the second order effects on the frequency response of a SAW filter, caused by electrode perturbation. This was carried out by analysing the response of a 2-dimensional, 11 electrodes per IDT delayline for different electrode dimensions and therewith their influence on the bulk waves. Ippolito *et al.* (2003) have used this technique for the 3-dimensional modelling of a layered delay line with two finger pairs per IDT and investigated the effect of electromagnetic feed-through and wave propagation in distinct directions. Atashbar *et al.* (2005) have undertaken a 3-dimensional FEM modelling of a delayline based hydrogen gas sensor. This was carried out by

analysing the response of the device with and without palladium thin film between the IDT's. Sankaranarayanan *et al.* (2007) have used this technique for the 3-dimensional modelling of a hexagonal SAW structure comprising of three two-port delayline structures. The frequency response and the wave characteristics for all the delay paths was investigated. Recently, Song *et al.* (2008) have used the same method to study the surface wave propagation in 3-dimensional concrete structures for nondestructive testing. Whilst the finite transducer FEM modelling approach has been applied to study the second order effects and sensing capabilities of SAW devices, it has not been applied to evaluate the frequency and time domain characteristics of a SAW correlator.

3.4 Correlator design using FEM

A 2 and 3-dimensional SAW correlator modelling is carried out using ANSYS, a commercially available finite element package. The simulations are aimed to characterise the full scale electromechanical phenomenon of the device, subjected to frequency and time varying excitation. A frequency sweep is performed using harmonic analysis to determine the response of the correlator for different acoustic modes of interest. The charge distribution of the correlator is calculated by solving the inhomogeneous piezoelectric partial differential equations with incorporated boundary conditions. The electrical admittance curve, to characterise the electrical behaviour of a SAW correlator, is obtained from the charge collected at the IDT. Apart from the admittance curve and the electric response calculation, analysis of various acoustic modes is carried out with the help of the displacement, electric field, and stress contours. Furthermore, these contour plots provide information about the mode depth penetration and interaction of surface acoustic waves with higher order modes. Moreover, the influence of the shear horizontal wave component on the performance of the structure is investigated through the 3-dimensional modelling of the SAW correlator. Finally, the transient response of the device is analysed for the instance when there is a code match.

3.4.1 Geometry

A meshed, 5×2-bit Barker sequence encoded, SAW correlator comprising a piezoelectric substrate and two non-uniform input and output IDT's is shown in the Fig. 3.9. The choice of the code length is guided by the aim to verify the functionality of the

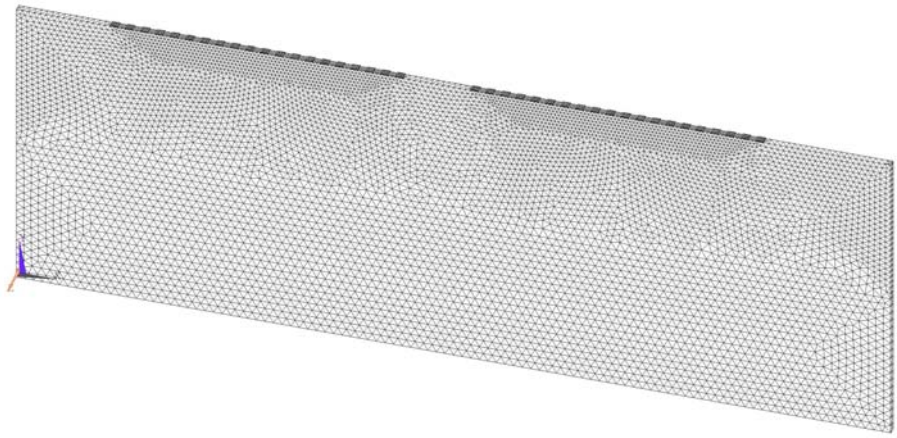

Figure 3.9. Meshed acoustic wave correlator model. The mesh is discretized to higher densities near the surface than near the bottom as the surface acoustic wave displacements are largest near the substrate surface.

FEM modelling approach, while keeping the computational time under control. Initially, a two dimensional model is employed to account for the large apertures of the correlators and straight crusted nature of the surface acoustic waves. Latter, a three dimensional model with a short aperture is considered to analyse the displacement component of the acoustic waves in the shear horizontal direction. Both the input and the output transducers have 20 electrodes each. Here, the input IDT of the structure is modelled as an expander to cause it to generate a coded acoustic wave when a normal pulse or a sinusoidal signal is fed to it. The expander IDT geometry determines the code of the generated acoustic wave. A 5(+++-+)×2(++) bit Barker sequence is encoded in the output/compressor IDT. This is carried out by coupling the electrodes of the IDT identical to the way they are connected to the positive and negative busbars. The input/expander IDT is a replica of the output/compressor IDT when a code matching is desired. The response of the device for mismatching codes can be observed by varying the input IDT finger geometry, in this case by varying the coupling between the electrodes.

The choice of the piezoelectric substrate determines the insertion loss of the correlator and hence the usability of the design for a specific application. The electroacoustic and acoustoelectric conversion at the input and output transducers, respectively, influence the insertion loss of the device. Hence, it is desirable to consider a piezoelectric substrate with high electromechanical coupling coefficient. Here, 128° YX $LiNbO_3$ was

chosen as the piezoelectric substrate, which is predominantly a Rayleigh type substrate. The FEM model has a substrate of length 28λ (λ = 40 μm) and a thickness of 12.5λ. The selection of the substrate thickness is guided by the thickness of the commercially available piezoelectric wafers. Gold was used to model the electrodes with a metallization ratio (MR) of 0.5, and an electrode thickness of 3%. The material properties of the piezoelectric substrate and electrodes are obtained from Auld (1990 (2^{nd} Edition)), as shown in Appendix. A. The separation between the IDTs is chosen to be 2λ. This was found to be an optimal distance to improve the gain and keep the electromagnetic feedthrough under control (Ippolito *et al.* 2003). The electromagnetic feedthrough is a secondary effect in SAW devices, which can degrade the stop-band rejection. It is caused by the interference of fields between the IDT's due to inductive and capacitive coupling.

Coupled field triangular elements with 3 degrees of freedom (DOF) are used for the 2-dimensional modelling of the device. These degrees of freedom are the displacements in the longitudinal (x) and normal (y) directions and the third being the voltage. The displacement profiles along the different directions is independent of each other as the substrate is anisotropic. The reactive charge component of individual elements is utilised to obtain the admittance curve. The model consists of approximately 100 thousand nodes forming over 45 thousand elements. A denser mesh was generated at the surface and through out the middle of the structure to realise an accurate representation of surface waves. However, the relatively coarser mesh near the bottom surface would still ensure an accurate characterisation of bulk waves as their wavelengths are about twice those of surface waves (Xu 2000).

3.4.2 Boundary Conditions

The application of boundary conditions is important to ensure the realistic modelling of the device both for replicating the actual working environment and minimising the impact of any design approximations. Due to the large electrode apertures and predominantly lateral propagation of the surface waves and bulk waves, a plain strain condition is assumed to reduce the model to a 2D model (Yong 2001). However, a 3-D modelling of the correlator with a small aperture width is also undertaken to confirm the validity of this assumption. This was carried out by investigating the displacement components in all the directions. It is desirable to suppress the acoustic reflection from the side boundaries of the device. The length of the piezoelectric substrate is extended

by 4λ at the IDT ends to minimise the electromechanical coupling contribution from the reflected waves. Although the choice of this substrate length, in the FEM model, is long enough to minimise the acoustic reflections from the side boundaries, the actual length of the physical device could not be replicated due to the huge model domain. Hence, an absorption side boundary condition was employed to counter the effect of the reflected waves (Song *et al.* 2008). Absorption boundary condition was introduced by selecting all the nodes on the side walls and defining the longitudinal (F_L) and normal (F_N) forces as

$$F_L = -\rho S_L (v_l^b - v_l^a) A_n, \tag{3.22}$$

$$F_N = -\rho S_N (v_n^b - v_n^a) A_n. \tag{3.23}$$

Here, ρ is the density of the piezoelectric material, S_L and S_N are the longitudinal and normal wave speeds at the side boundaries, respectively, v_l^b and v_l^a are the longitudinal velocities of the boundary node and the node adjacent to it, respectively, v_n^b and v_n^a are the normal velocities of the boundary node and the node adjacent to it, respectively; and A_n is the influential area of the boundary node. The bottom surface of the correlator is clamped and an air boundary is defined on the top surface to replicate the real operating conditions.

3.5 Fabrication

The optical lithography and electron beam lithography are the two predominantly used techniques for SAW device fabrication (Gardner *et al.* 2001). The line width of the device and therefore the operating frequency determines the fabrication approach. Optical lithography or photolithography is limited by the wavelength of the light exposed to the wafer, which in turn places a limit on the resolution of the electrodes. Optical lithography is sufficient for devices operating at frequencies up to 800 MHz, however, for higher frequencies electron beam lithography is the preferred technique (Brocato 2004).

The SAW device fabrication in this research was carried out using optical lithographic process, as shown in the Fig. 3.10. A 4" 128° YX $LiNbO_3$ circular wafer is cleaned with acetone, IPA and then de-ionized water and blow dried with an N_2 gun to remove any organic and inorganic depositions. A gold film of thickness 1.2 μm was deposited over a seed layer of $NiCr_2$ to ensure good adhesion with the wafer. The wafer was then

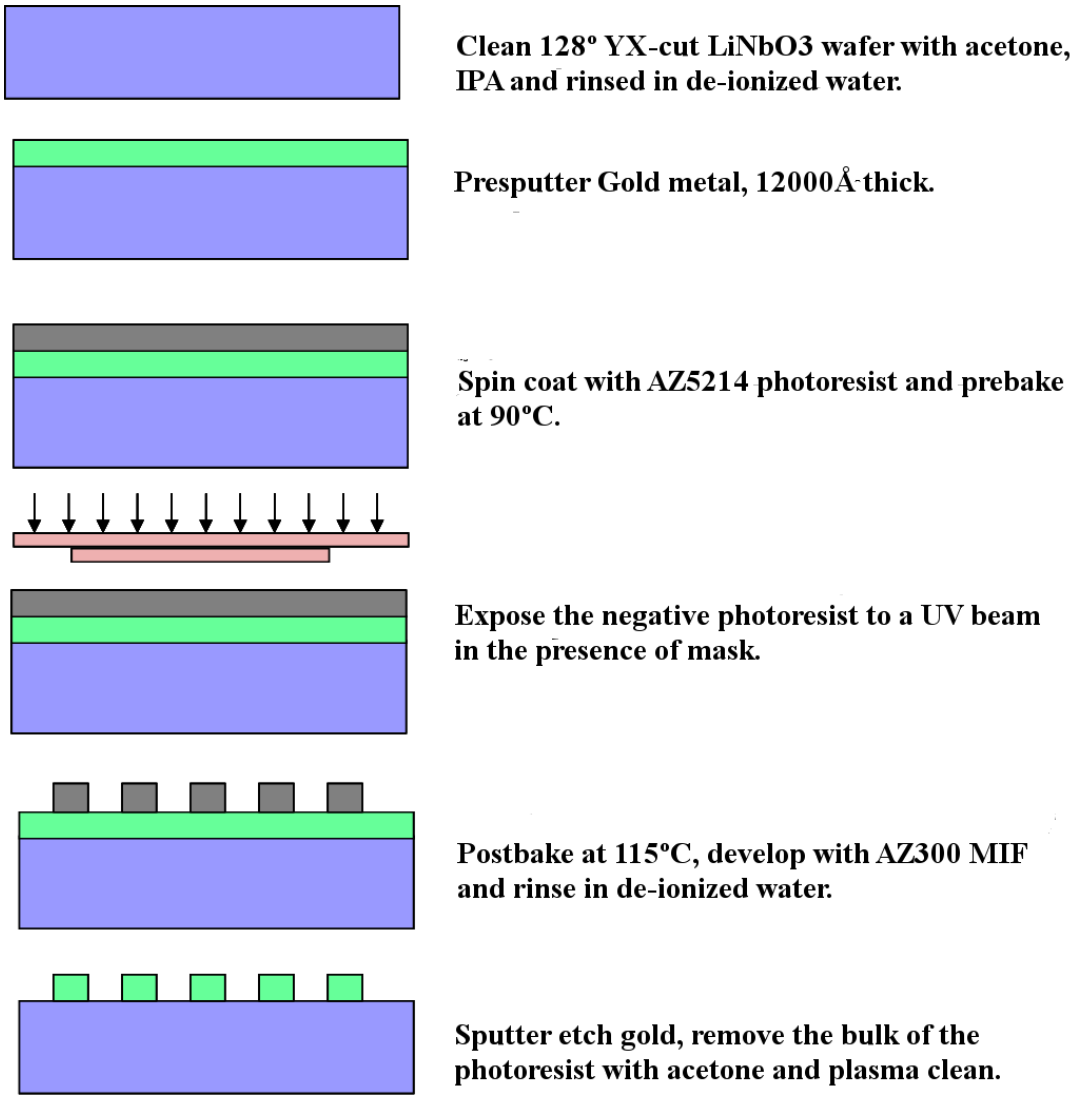

Figure 3.10. SAW device fabrication flow.

spin coated with AZ5214, a negative photoresist, to produces a constant thickness. It is then prebaked at 90°C to make the harden the photoresist and make it sensitive to ultraviolet (UV) light. In the next step, the sample was exposed to UV light through a mask, which defines the geometry of the IDT patterns to be generated on the wafer. The mask was kept close to the wafer, which was held flat to suppress the diffraction of UV light and therefore improve the photolithography resolution. The exposed negative photoresist is cross linked and is thus insoluble in the developer solution. Following this, the wafer was postbaked at 115°C to change the material properties of the photoresist. The wafer was then exposed to a flood of UV light without a mask to make the previously unexposed areas of the photoresist soluble in developer. Then, the wafer was developed with AZ300 at room temperature and rinsed with de-ionized

water to remove the unexposed areas of photoresist. The areas of the gold which were not covered by the photoresist were sputter etched by ion bombardment and extreme care was taken not to damage the wafer. In the last step of photolithography, the remaining photoresist was bulk stripped with acetone and plasma cleaned. With this a number of SAW devices were fabricated on the wafer. Following this, a gold layer of 1.2μm thickness is deposited on the other side of the wafer to be used as ground. Fig. 3.11 depicts an SEM image of a sample 7 $\times$ 5-bit Barker sequence SAW correlator built using the above describes fabrication process for a linewidth of 10 μm.

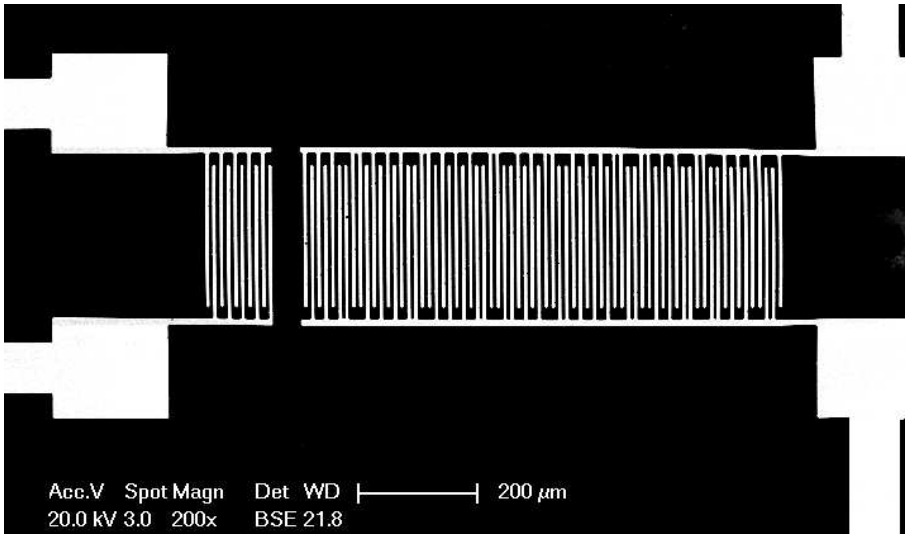

Figure 3.11. SEM photograph of a 7 $\times$ 5-bit Barker sequence SAW correlator with 10 μm linewidth.

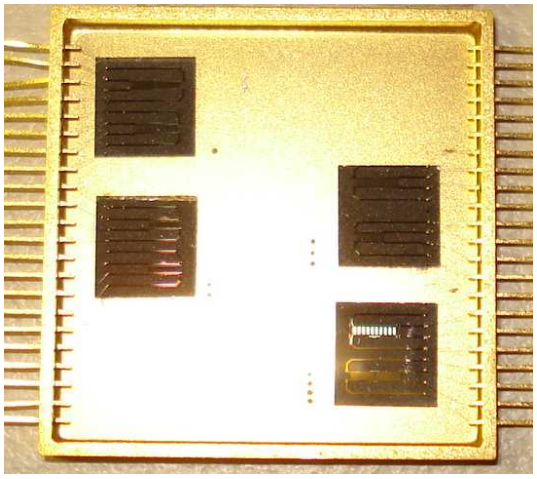

Figure 3.12. The fabricated SAW devices mounted on a 54 pin DIL carrier.

The wafer was then diced into square dies of 7.5×7.5 mm such that each die consists of two SAW devices. A variety of package styles and sizes were consider before choosing a 54 pin Dual In Line (DIL) carrier with dimensions of 38.5×38.8 mm. A maximum of 6 dies could be placed in each package using silver epoxy. To ensure an even smear and tight bonding, the package is cured at 85°C for 2 hours. The pads of the dies are wire bonded to the pins of the package using gold wire of diameter 25 μm. A sealable package with 6 dies wired bonded to the pins is shown in the Fig. 3.12.

3.6 Results and Discussion

The mode propagation properties and the electrical response of both the FEM modelled and fabricated, $5\times$2-bit Barker sequence SAW correlator, subjected to electrical excitation, are described in this section. Furthermore, the impact of the shear horizontal acoustic wave component and the non-correlating code of the input BPSK signal on the correlator's response is also analysed. Initially, modal analysis is performed on the design to identify the freely propagating modes, particularly symmetric and anti-symmetric SAW modes, through the examination of eigenvectors and eigenfrequencies. This was used as a starting point for the harmonic and transient analysis.

3.6.1 Harmonic Analysis

A valuable insight into the excitation properties of the model can be gained from harmonic analysis, where the particular solution of the system of partial differential equations given in Eqns. (3.16 & 3.17) is computed. In this work, the frequency response of correlator was obtained by driving the input IDT electrodes with an alternating voltage with 20 volts peak-to-peak.

The focus is on modelling a low loss correlator, that can power miniature wireless actuators in a secure manner, through the optimisation of design parameters. The correlator's response to different acoustic modes, when there is a code match, is considered as one of the design parameters. Hence, the harmonic analysis was carried out for a wide frequency range. Depending on the operating frequency, various acoustic wave modes and their associated harmonics were excited. These modes can be identified by observing the contour plots, e.g. displacement, potential, and stress, of the structure.

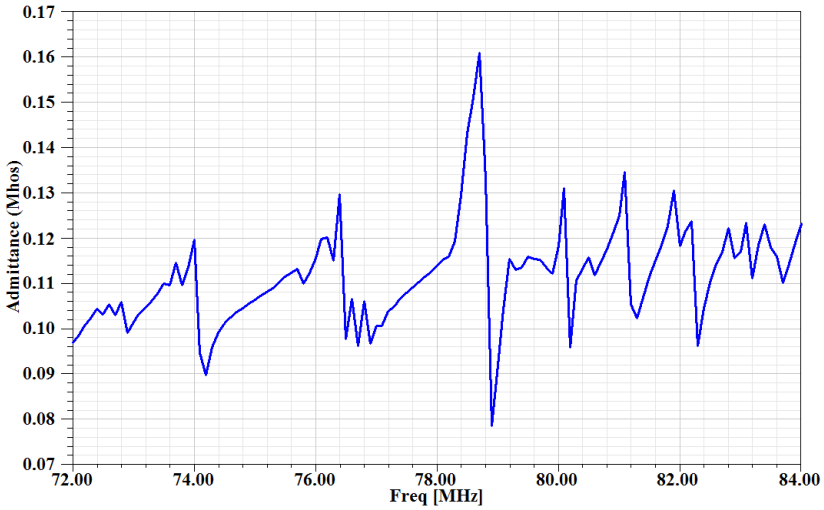

Figure 3.13. Electrical admittance response of the correlator when there is a code match. The admittance peaks at 78.8 MHz and 80 MHz correspond to the anti-symmetric and symmetric SAW modes, respectively.

The complex admittance of the device was computed based on the accumulated complex charge at the electrodes (Eqn. (2.40)). As can be seen from the Fig. 3.13, the magnitude of the complex admittance attains, as expected, a high value at the resonant frequencies and hence exhibits a strong peak. The dominant admittance peak at 78.8 MHz corresponds to the anti-symmetric surface acoustic wave mode with a minor peak at 80 MHz corresponds to symmetric SAW mode. The symmetric SAW mode is not as profound as the anti-symmetric SAW mode due to the destructive interference of the eigenmodes. The eigenvalues for these two modes (Figs. 2.7 & 2.6) were discussed in detail in Chapter 2 for the FEM modelling of the periodic structure. Fig. 3.14 shows the displacement contour, summation of the x and y displacement components, of the correlator for the anti-symmetric SAW mode. The wave displacement was confined to the top surface of the structure with a maximum displacement of 5.11 nm.

The other admittance peaks in the Fig. 3.13 correspond to the waves with higher wave penetration depths into the substrate. The penetration depth of the mode at 82.4 MHz is larger than 6λ.

The output voltage response of the correlator is determined by the electromechanical coupling energy E_c given by (Moaveni 2007 (3^{rd} Edition))

$$E_c = -\frac{1}{2} S_{ij}^{T}[e] E_k, \tag{3.24}$$

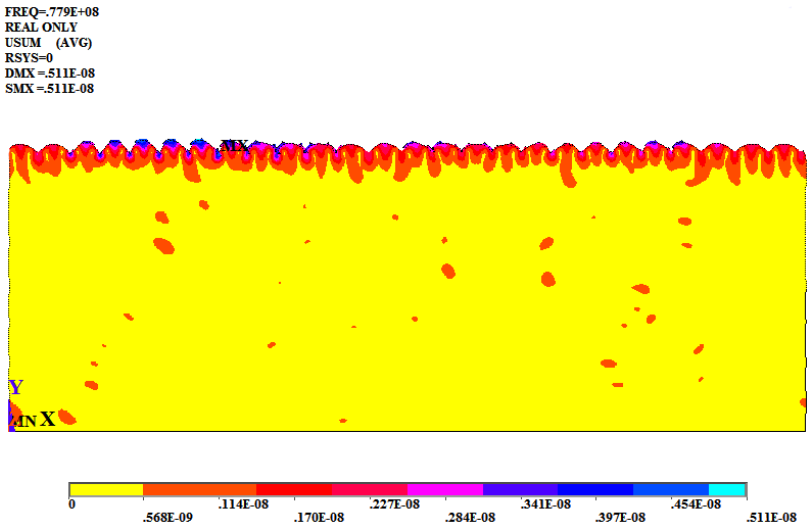

Figure 3.14. Surface acoustic wave displacement contour for a substrate thickness of 10λ. The acoustic wave displacement is confined to the top surface of the substrate and, as can be seen from the scale, is in nanometers.

where S_{ij}^{T} is the strain vector with constant stress, $[e]$ the piezoelectric stress matrix, and E_k the electric field vector. Fig. 3.15 shows both the simulated and measured output voltage response of the correlator, when the code matches, for different acoustic modes determined by the excitation frequency. The modes definitely impact the response of the correlator and as can be seen from the Fig. 3.15, the output response is highest for the anti-symmetric SAW mode. Hence, it is desirable to operated the correlator at this mode where the acoustic energy is confined to within one wavelength from the substrate surface along the y direction. The high electromechanical coupling is attributed to the absence of additional propagation losses caused by the wave propagation into the depth of the substrate or the bulk-wave scattering (Lehtonen *et al.* 2004). A good agreement between the measurements and simulations is observed in terms of modal excitation frequencies. The minor deviance in voltage profiles at SAW mode is attributed to differences in apertures of the physical structure and FEM model. However, the significant potential differences for other modes is due to the non-consideration of shear horizontal wave component in the 2-dimensional model. Nonetheless, the wave propagation in the shear horizontal direction for a 3-dimensional correlator is analysed in the later subsection with a short aperture.

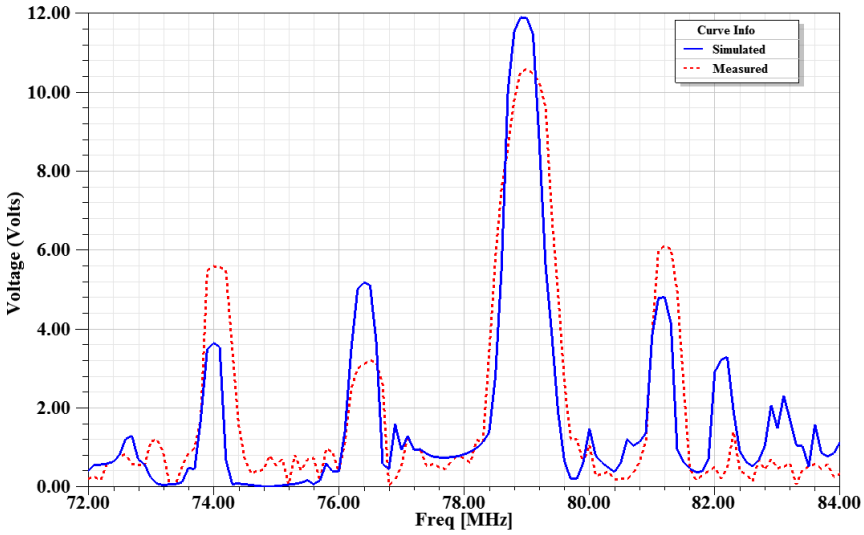

Figure 3.15. A frequency sweep of the voltage across the output IDT, for different acoustic modes, when there is a code match. The output response is maximum at the anti-symmetric SAW mode

3.6.2 Transient Analysis

Transient analysis was performed on the correlator FEM model for a time of 3.5 microseconds. The matched code sequences are sent successively by driving the expander IDT with a $\pm 10V$ sinusoidal signal. The frequency of the sinusoidal input is 78.8 MHz, corresponding to the SAW mode. Coded surface acoustic waves are generated in both directions of the expander IDT as could be verified from the displacement contours. These simulations are computationally very intensive. The simulated output IDT voltage profile, shown in Fig. 3.16, took about 30 hours of computer run-time on a dual 2.33 GHz Xeon processor with 8 GB RAM. The voltage profile at the output IDT provides a measure of the acoustic wave propagation times and the signal correlation.

The output response initially was very low due to the time taken by the surface acoustic wave to propagate from the input IDT to the compressor IDT. Moreover, the mismatched filling of the correlator caused by the non-synchronisation between the coded acoustic wave and the encoded electrodes of the compressor IDT contributes to this delay. From the instance when the synchronous filling of the correlator occurs the device stabilises, as can be observed from Fig 3.16, after 650 ns. After this time, the electrodes of the compressor IDT pick up the coded acoustic waves synchronously and hence the correlation peaks can be observed from then on. However, the peak-to-sidelobe ratio

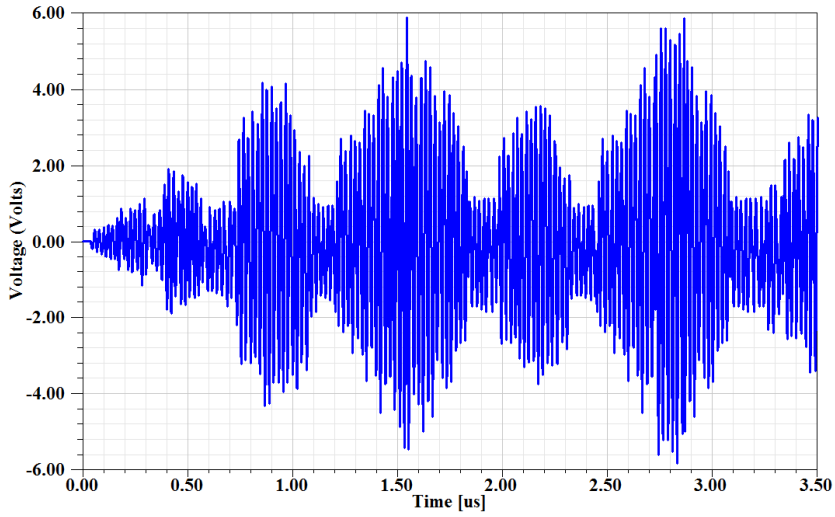

Figure 3.16. The transient response of the voltage across the output IDT, displaying the acoustic propagation times and the signal correlation.

is low due to the short length of the code employed. The simulated correlation peaks are consistent with those observed experimentally.

3.6.3 Effect of the shear horizontal wave component on the correlator response

It is necessary to carry out a 3-dimensional modelling of the correlator both to gain a deeper insight into the mode propagation characteristics and to completely account for the anisotropic nature of the piezoelectric substrate. In this research, a 3-D modelling of the above discussed correlator is performed with all other dimensions and boundary conditions kept the same. The aperture or the width of the structure was limited to 40 μm as a higher value would require large number of elements limiting the practical applicability of the method for now. The propagation characteristics of the excited waves depends on the property and orientation of the piezoelectric material, the thickness of the deposited metal, and the boundary conditions. A quadratic coupled field element with 20 nodes and 4 degrees of freedom per node was chosen to model the 3-D structure. The additional degree of freedom in this element, compared to the 2-D element, is the displacement in the shear horizontal (z) direction. After harmonic excitation, the admittance peaks could be observed at the same frequencies, however, with suppressed magnitudes due to the aperture width limitation.

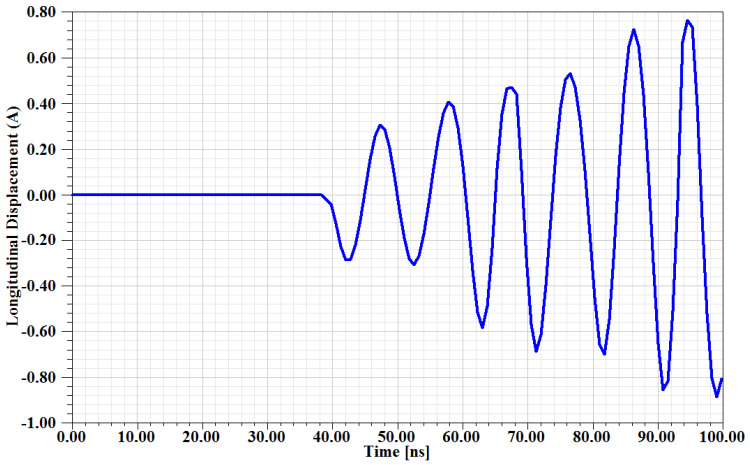

(a)

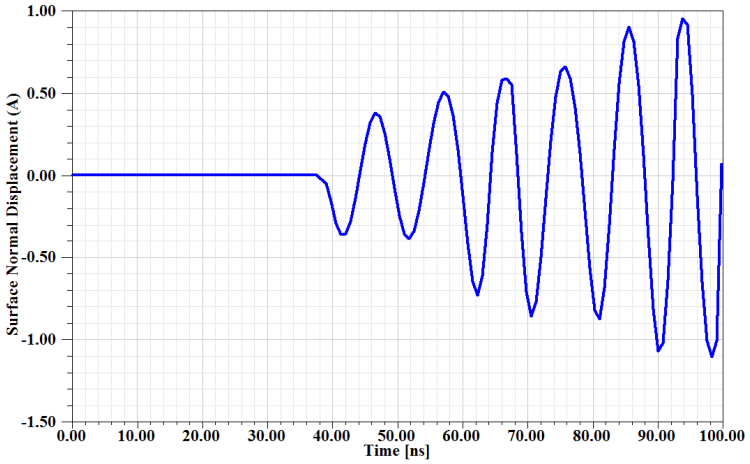

(b)

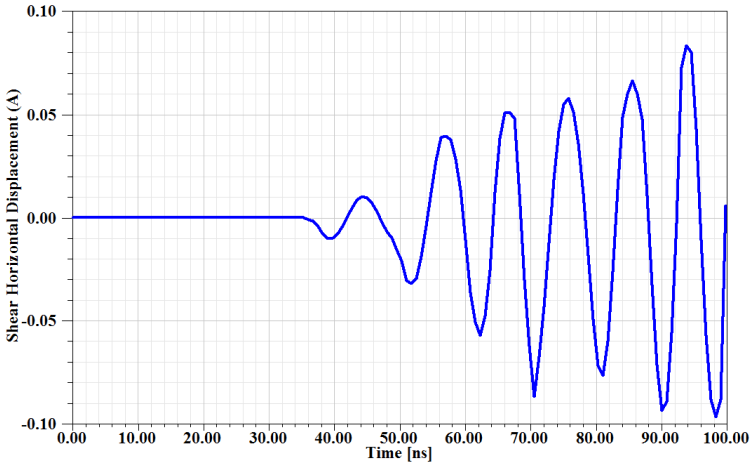

(c)

Figure 3.17. Displacement at the output IDT along the (a) longitudinal direction. (b) Surface normal direction. (c) Shear horizontal direction.

Then, the correlator structure was driven by a sinusoidal signal with SAW modal frequency. The particle displacement in all the directions is analysed for a node on the output IDT, as depicted in the Fig. 3.17. It can be observed that the maximum displacement amplitudes in the longitudinal (x) and surface normal (y) directions are 0.76 A and 0.92 A (where 1 A = 10^{-10} m), respectively. However, the maximum displacement component in the shear horizontal direction is 0.08 A, which is an order of magnitude less than the other two components, which is indicative of the Rayleigh wave motion. Thus, it can be asserted that the minor difference in the output voltage between the simulated and the measured structures at the SAW mode in Fig. 3.15 is a reflection of the aperture deviance rather than the acoustic wave characterisation disparity.

3.6.4 Correlator response analysis for mismatched code

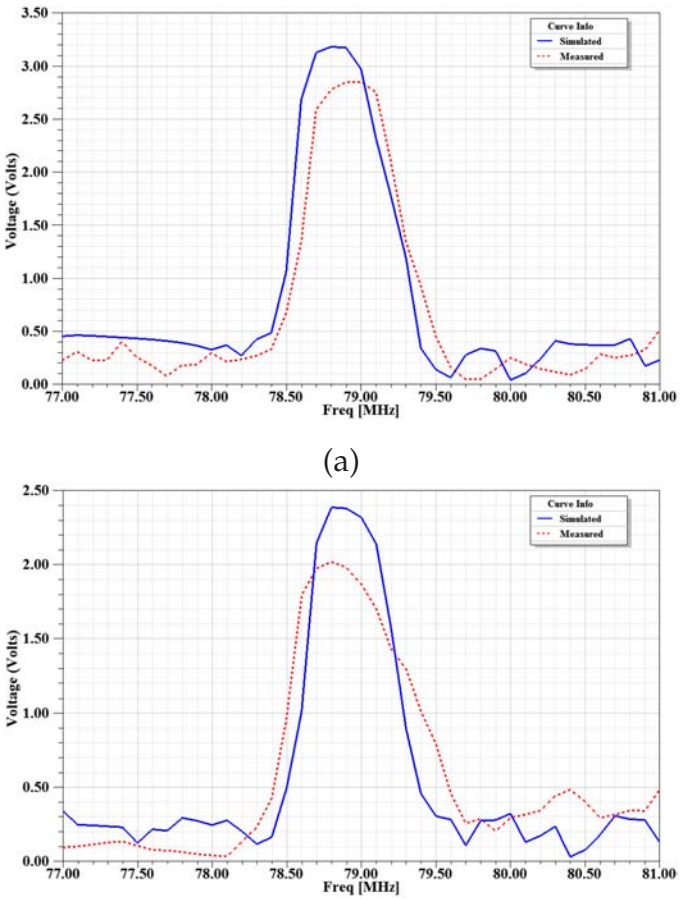

(a)

(b)

Figure 3.18. Voltage across the output IDT when there is a code mismatch (a) delay line input (b) noncorrelating input.

So far the results are confined to the instance when there is a code match between the input signal, in this model the expander IDT, and the compressor IDT of the correlator. The functionality of the correlator can best be verified by comparing its response to a matched and mismatched input codes. This was carried out by varying the electrode coupling of the expander IDT. The simulated and measured response of the correlator to two different codes, a delayline input and other noncorrelating input, is shown in Fig. 3.18, while all other specifications are kept the same. By comparing these responses with the correlating peak response of the Fig. 3.15 it can be established that in addition to the excitation frequency, the correlator's response is determined by the code in the RF signal. Even in the case of a delayline input, when the two codes are very similar, the device response is much less than its response to the matched code, as shown in Fig. 3.15.

3.7 Conclusion

A rigorous modelling approach for precise simulation of SAW correlators is presented. The requirements placed by the current and emerging wireless interrogation applications on these devices such as low insertion loss and high selectivity are taken into consideration. The results discussed in this work include: (i) Comprehensive FEM modelling of 2 and 3-dimensional, 5×2-bit Barker sequence encoded SAW correlator, and device fabrication using photolithographic techniques. (ii) Detailed study of the harmonic and transient responses of the correlator using Au electrode grating on 128° YX $LiNbO_3$ piezoelectric substrate, while considering the effect of the shear horizontal wave component, difference in electrical response when there is a code mismatch, and comparison of the simulation results with physical measurements were conducted. As the applicability of this method is not restricted by the design complexities or the material properties or the loading conditions it provides an effective way for gaining a deeper understanding of the correlator's response and ultimately in the optimisation of correlator design. Backed by experimental validation of developed SAW correlator FEM model, its application to the design and optimisation of a wireless powered microvalve is presented in the next chapter (Chapter 4).

Chapter 4

A SAW Based Remotely Actuated Microvalve Modelling

4.1 Introduction

With the ever increasing demand for high performance microfluidic devices and continuous quest for miniaturisation, the development of novel and innovative microvalves has witnessed a rapid growth in the recent times (Oh and Ahn 2006, Nguyen *et al.* 2002, Nguyen and Wereley 2002). Most of the research in this area is focused on improving the performance of the microvalve by targeting features such as flow rate, leakage flow, power consumption, response time and disposability (Oh and Ahn 2006, Hesketh *et al.* 2003, Frecker 2003). However, the constant expansion of the application domain of these devices into fields as diverse as life sciences and chemistry applications is placing new demands on the existing models (Gomez 2008, Felton 2003). One of these new design requirements is the remote interrogability of the microfluidic devices. The capability to wirelessly control fluid flow can emerge as an attractive technology enabling various biomedical applications. Furthermore, most of the existing microfluidic devices in biomedical implants are either battery powered or have external pump modules that are connected to the patient by means of a passive port (Cao *et al.* 2000, Geipel *et al.* 2006). The use of a battery places additional constraints on the device size and would require an electronic circuitry module. Hence, the development of an active microvalve with fully passive components, enabling wirelessly control of fluid flows, is a key task in the realisation of compact high performance biomedical implants. Moreover, such a device would provide a freely programmable, time-modulated control profile to ensure patient safety and comfort in long-term treatment.

Microfluidic devices using acoustic streaming phenomenon have been investigated in the literature (Demirci 2006, Wixforth 2004). These devices use surface acoustic waves or flexural plate waves to cause fluid motion, through hydrodynamic coupling, on the planar surface of the piezoelectric material. Acoustic streaming based microfluidic devices have several advantages such as low fluidic impedance of the channel, simple structure and low sensitivity to the electrical and chemical properties of the fluid. However, secure actuation of the wireless devices using acoustic streaming is limited only to frequency addressability rather than discrete code addressability, thus rendering them inefficient for remote interrogation applications. This shortcoming is tackled, in this research, by using two identical 5×2-bit Barker sequence encoded surface acoustic wave (SAW) correlators placed one on top of the other with an air gap and suspending an edge clamped microchannel with two conducting diaphragms between the compressor interdigital transducer's (IDT) of the correlators. The correlator's response is employed to impart ultrasonic energy on the conducting diaphragms using electrostatic actuation. Thus combining the high frequency operation of the ultrasonic, secure code embedded, acoustic correlator with low power, fast response time, and reliability of electrostatic actuation. Successful wireless operation of this device hinges on the precise occurrence of fluid flow when interrogated by a correlating BPSK signal. The microvalve is normally closed and is opened by using the deformation of the diaphragms caused by the electrostatic effect. The risk of high leakage and valve clogging is addressed by employing both diffuser elements and check valves in the structure.

Small device dimensions make it typically complicated or even impossible to perform measurements of the physical conditions inside microdevices. To facilitate optimal design of MEMS devices based on such microactuators, efficient simulation schemes for analysing the channel deformation are required. The physical behaviour of micro components is best described by partial differential equations, which are typically solved by finite element methods. Due to the complexity involved in combining the electroacoustic and electrostatic mechanisms, a systematic design and optimization of the active microvalve is best possible with finite element method (FEM) modelling. Furthermore, coupled field simulations are vital for capturing both electroacoustic and electrostatic-structural interactions in a single finite element run and for taking into account non-linear effects that are inherent in MEMS devices. Hence, in this work, we model the whole structure by employing a direct FEM to verify the functionality of

the concept. The FEM simulation architecture for the structural components of the microvalve consists of two major subsystems: a SAW correlator electroacoustic analysis, including the voltage response and the influence of the excited acoustic modes, as was discussed in the Chapter. 3, and a microchannel electrostatic analysis that captures the channel deformation and the code dependent behaviour of the structure.

In this Chapter, the design and simulation of a 3-dimensional, remotely interrogatable, active microvalve is presented using two 5×2-bit Barker sequence encoded SAW correlators. In Section 4.2, the use of SAW devices for microfluidic applications including acoustic streaming is outlined. In Section 4.3, the principle of operation, the transmitter receiver architecture, electrostatic actuation and the finite element formulation is discussed. Then in Section 4.4, the microchannel electrostatic model, including the dimensions of the structure and materials are described. In section 4.5, the results of the comprehensive harmonic and transient deflection analysis of the microvalve for variable acoustic modes and different input interrogating code sequences are presented.

4.2 SAW devices for Microfluidic Applications

In recent times extensive research and development efforts are globally directed towards fluid diagnostics and flow manipulation by adopting advances made in other expansive fields such as MEMS, micromachining and material sciences. The novel miniature microfluidic pumps, valves, sensors and controllers have reached a level of maturity to make deep inroads into both civilian and military markets. As per market studies, the microfluidic component market is projected to reach $4.2 billion by 2014 (Micro fluid management technology - Yole development). It is also reported that the trend towards function integration would drive the demand for next generation of microfluidic applications such as portable medical devices, micro-fuel cells, and microchemical reactors. The use of SAW technology for such applications has the potential to open up many new possibilities. The main advantage of such an approach is that the SAW devices, being inherently passive and robust, are not severely impacted by the hostile conditions. Furthermore, with the ability to wirelessly power and control, these devices can be placed in remote locations.

SAW device are commonly used in consumer electronics as high frequency filters and signal processing components. Over the past two decades the use of SAW devices for

sensing, especially for microfluidic applications, has gained momentum. To be quantified as a sensor there is a need to have a sensing layer that is commonly designed in between the input and output IDTs. The layer should be sensitive to the input stimuli and is usually deposited in between or above the IDT's. The variation in the properties of the sensing layer when contacted by the fluid determines the dynamics of the interaction between the charges at or close to the surface of the sensing layer and the underlying SAWs. This is measured in terms of deviation of the wave velocity, phase angle or the attenuation of the output response of the SAW sensor. The acoustic wave sensors have the additional capability to sense both gas and liquid media. The development of a wide array of acoustic sensors have been reported in the literature targeting microfluidic sensing quantities such as gases at high temperature (Thiele and da Cunha 2003), viscosity (Bastermeijer *et al.* 2002), humidity (Li *et al.* 2007b), antibody-antigen reactions (Luo 2004), DNA molecules (Sakong *et al.* 2006), and protein samples (Mitsakakis *et al.* 2009).

4.2.1 Acoustic Streaming

Recently SAWs are increasingly being employed to act in a completely different way than for sensing in micro-fluidic applications, i.e., for the manipulation of fluid flow. This is carried out by a phenomenon known as acoustic streaming where the interaction of the acoustic wave with the fluid on the surface, as shown in the Fig. 4.1, induces an internal streaming. This internal streaming causes a droplet motion in the range of microliters down to picoliters. As most of the energy propagating in a SAW is of mechanical nature, the acoustic radiation pressure exerted on the fluid drives it in the direction of the propagation of the acoustic wave. Fluid tracks are created on the surface of the substrate, to confine the liquid flow to a predetermined path, by the chemical variation of the surface tension of the tracks. The acoustic streaming technique reduces the reliance on other passive flow control mechanisms, such as capillary force, needed to overcome the high impedance of the channel (Wixforth 2004).

The ridges and wells of the acoustic wave create a fluid pressure difference ($2\delta p$) which leads to a difference in the liquid density ($2\delta\rho$). Thus, the excited longitudinal acoustic wave, into the liquid medium, comprises of oscillating pressure and density components with an equilibrium values of p_0 and ρ_0, respectively. If v_S and v_L are the acoustic velocities in the piezoelectric substrate and liquid medium respectively, then the

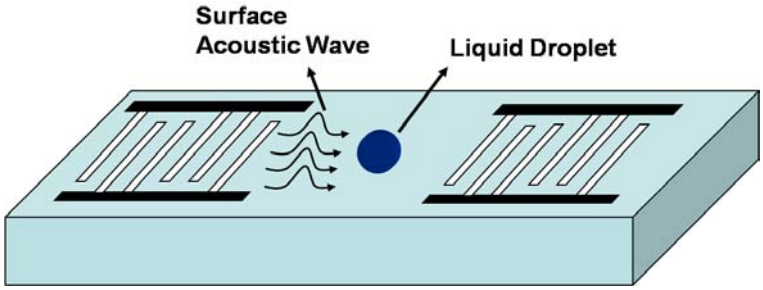

Figure 4.1. Acoustic streaming of liquid using a SAW device.

diffraction angle of the launched wave is given by (Strobl *et al.* 2004, Wixforth 2004)

$$\Theta_D = \arcsin\left(\frac{v_S}{v_L}\right). \tag{4.1}$$

Furthermore, the radiation pressure of the launched wave that causes the internal streaming of the liquid is given by

$$p_a = \rho_0 v_S^2 \left(\frac{\delta\rho}{\rho_0}\right)^2. \tag{4.2}$$

Many microfluidic devices based on acoustic streaming such as micropumps (Nguyen and White 2000, Rife *et al.* 2000), microliquid heating systems (Kondoh *et al.* 2005), micro-particle removal devices (Qi and Brereton 1995), and ultrasonic motors (Changliang and Mengli 2005) have been reported in the literature. These devices thrive on the numerous advantages offered by SAW technology. Some of them are simple device structure, ease to manufacture, high reliability due to the lack of moving components, and improved channel resistance because of the presence of propelling force throughout the fluidic network. Moreover, very large forces are generated over a very small area due to the scalable nature of the acoustic streaming phenomenon. This enables small scale applications where the contribution of acoustic force to induced streaming is significant. However, acoustic steaming based microfluidic devices are plagued by their share of limitations as well. These devices suffer from low efficiency as the induced streaming is a nonlinear and second order phenomenon. A plausible way of addressing this shortcoming is by employing large amplitude acoustic waves, which would make streaming inappropriate for applications where power usage is critical such as wireless and battery-less applications. Moreover, the amount of heat generated at the solid liquid interface for such high acoustic amplitudes is detrimental for thermally sensitive liquids. Due to these limitations, no wireless acoustic streaming

based fully passive microfluidic device is presented in the literature. Even if developed, by employing recent innovations such as focusing of acoustic power with horns, lenses and focused transducers (Frampton *et al.* 2004, Yu *et al.* 2006), the secure actuation of such a device is limited only to frequency addressability rather than discrete code addressability, which would render it inefficient for remote interrogation applications. This constraint is addressed in this research by employing a synergetic approach which combines electroacoustic correlation and electrostatic mechanisms, as discussed in detail in the next section.

4.3 Wireless Microvalve Design

Microvalves can be classified in two broad categories namely active and passive. While the the fluid flow in passive microvalves is controlled by the fluid pressure, active microvalves are triggered by an external signal irrespective of the fluid dynamics. Active microvalves have emerged as the predominant form of microfluidic components currently being employed for a wide array of applications ranging from on/off switching to fluid flow control and isolation. Innovations in this area are normally aimed at developing novel devices with optimising characteristics such as valve closing dynamics, response time, power consumption, leakage, flow resistance and reusability. However, not much research effort is directed towards remotely controlled flow manipulation, which has the potential to pave a new way for the next generation of microfluidic devices. The possible applications of a remote controlled, fully passive microvalve are boundless, especially for drug delivery applications in the biomedical field. The ability to wirelessly administer accurate doses of drug, for an extended period of time, at an inaccessible target location, through an implanted microvalve can revolutionise the way diseases such as cancer and diabetes are treated.

The design of a normally closed, remotely actuated, secure coded, batteryless, active microvalve using fully passive components is presented in this chapter. The crucial choice of actuation mechanism for microvalves is normally guided by the design specifications. Even though acoustic streaming appears to be a suitable actuation principle, that comes closest to satisfying all the above mentioned design specifications, it falls short in addressing the power and secure coding requirements. These drawbacks are alleviated in this research by combining the complex signal processing capabilities of

acoustic wave correlator with the electrostatic actuation of the microchannel. This synergetic approach incorporates the advantages of both of these mechanisms into the microvalve design.

4.3.1 Principle of Operation

The design of the current novel, passive, wireless microvalve is motivated by the aim of high-resolution volumetric dosing and the demand for a minimum device size and power consumption. The core components of the microvalve are two identical SAW Correlators, two diaphragms and an antenna array. The diaphragms are suspended with an air gap between the compressor IDT's of the correlators forming a microfluidic channel. The resulting correlated output at the compressor IDT of the correlator generates an electrostatic field within the air gap which in turn deflects the diaphragms, thereby regulating fluid flow through the microfluidic channel.

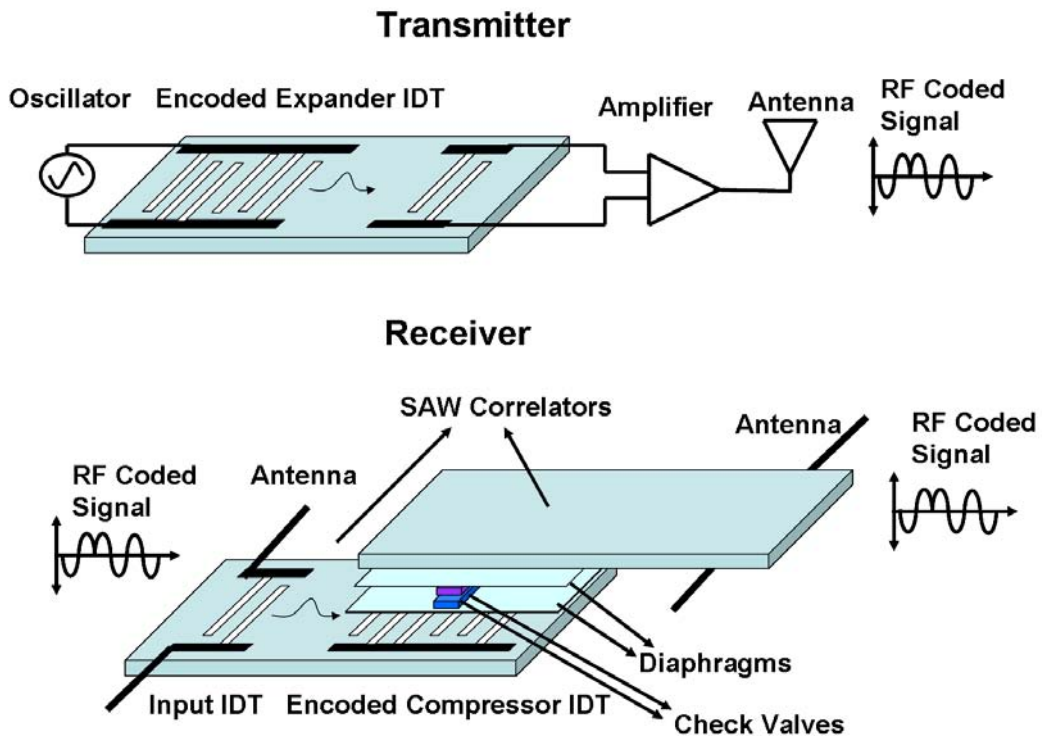

Figure 4.2. Wireless microvalve transmitter-receiver configuration. The transmitter transmits a RF coded signal with the use of an expander IDT. The two identical SAW correlators of the microvalve are triggered simultaneously if the transmitted signal code matches with code of the correlators, and thus facilitates a secure microchannel deflection.

The wireless telemetry system for the SAW based microvalve is depicted in Fig. 4.2. By means of the antennas, the microvalve captures part of the electromagnetic energy to provide power for its own operation. One of the advantages of this approach is the ability to establish bidirectional communication between the microvalve and the interrogator. Moreover, this concept does not allow simultaneous triggering of several microvalves present in the same electromagnetic field as each device is encoded with a different code. System level protocols, such as those in use in contactless smart-card readers, allows a single interrogator to communicate with several individually identified microvalve.

A coded SAW based communication system for the microvalve consists of an expander IDT in the transmitter and a compressor IDT in the receiver, as explained in detail in the previous chapter and briefly outlined here for the sake of clarity. A narrow pulse or a sinusoidal waveform is fed to the expander IDT to generate a coded acoustic signal depending on the geometry of the expander IDT. These acoustic waves propagate through the substrate to the transmitting IDT, which transforms these coded acoustic waves to electrical coded RF signal. The output from the transmitting IDT is fed to an amplifier, to strengthen the signal, and then to a transmitting antenna. The receiver consists of two identical correlators, the operation of which is explained in the next section, with their input IDT's connected to the receiving antennas to intercept the transmitted coded RF signal. The expander in the transmitter is an exact replica of the compressor/coded IDT of the correlators. The coding of the expander and compressor determines the autocorrelation function performed by the correlators. The resultant response of the acoustic devices is then electrostatically coupled to the conducting diaphragms, suspended between the compressor IDT's with an air gap. Thus the actuation method not only depends on the excitation frequency but also on the code of the transmitted BPSK signal. The microchannel comprises of two diaphragms with check valves and an inlet and outlet diffuser element on the either side of the channel. Apart from the fluid flow resistance of the inlet and outlet diffuser elements, the leakage is further controlled by the check valves. When an electrostatic force is applied, the diaphragms are pulled towards the compressor IDT of the correlators causing the check valves to separate. Thus, the simultaneous actuation of the diaphragms at ultrasonic frequencies by the correlating input signal allows the microvalve to induct and expel fluid through the check valves in the channel. On the fabrication and assembly of the proposed microvalve structure, the SAW correlators and the antennas can be custom built by using optical lithographic techniques, whereas the diaphragms can be

acquired off the shelf. The mounting of the microchannel in between the SAW correlators can be carried out by using microassembly techniques. However, the assembly of all the subcomponents of the microvalve is outside the scope of the current thesis.

The valve efficiency is a critical parameter when microvalve is used in on/off switching applications. The valve efficiency of an active microvalve with diffuser elements is poor in the reverse direction due to high leakage. The desired leak-tight operation makes it necessary to incorporate micro check valves on the diaphragms in the fluid channel. The lateral dimensions of the check valves are designed to make them stiff enough to resist bowing under pressurisation caused by the fluid in the idle state and yet compliant enough to allow for the diaphragm motion during actuation. The sketches in Fig. 4.3 depict the functionality of the microvalve in the OFF/normally closed state and ON state. In the OFF state the check valves push tightly against each other as shown in Fig. 4.3(a). Assuming a perfect check valve, the fluid flow through the channel is shut-off in the OFF state or even when there is a mismatch in the operating frequency and code of the interrogating BPSK signal. In the ON state, when the device is interrogated by a correlating signal, the double membranes inflate due to electrostatic actuation and inhale the fluid into the chamber. Since this is happening at ultrasonic frequency the expansion and compression of the channel volume allow the compressed fluid to escape through the outlet. The microchannel dimensions and the diaphragm deflection depend on the application envisaged for the device. The piezoelectric material's electromechanical coupling capabilities, the encoded code of the SAW correlator, the diaphragm material and thickness, the air gap, the compliances of the fluid and check valve elements in the channel, and the nature of the interrogating RF signal all contribute to the performance of the microvalve device.

The fabrication of microfluidic devices is time consuming, expensive and complex. The lack of a generalised architecture, especially for a specialised design such as the one proposed in the current research, necessitate a thorough understanding of the multiple coupled physics phenomenon at the process level, before fabrication. Moreover, the measurement of physical quantities in miniature microdevices is complicated and in some instances unfeasible. However, with the use of FEM based multiphysics modelling the interactions between electromagnetic, piezoelectric, electroelastic and fluid fields can be analysed to gain a deeper insight into the operation and functioning of

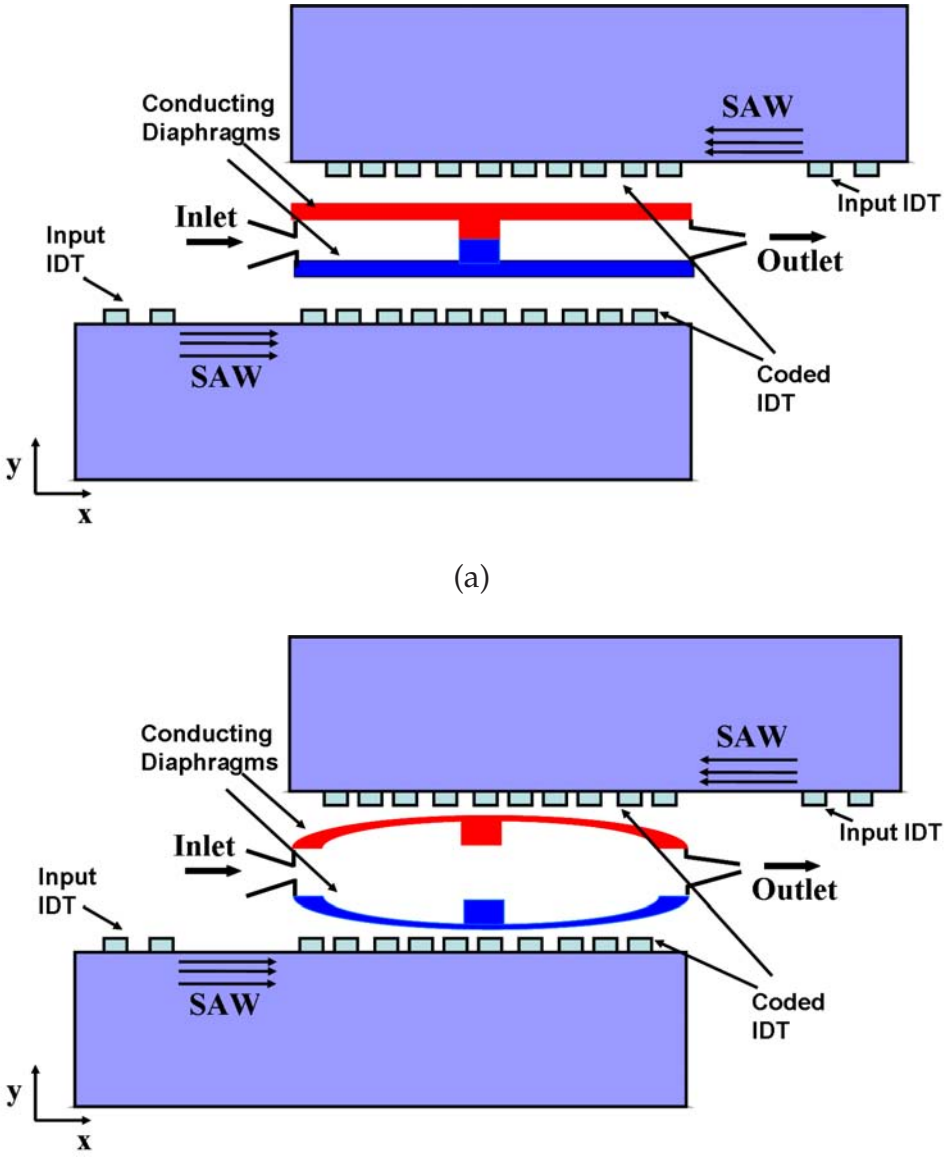

Figure 4.3. Microvalve in (a) OFF/Normally closed state. (b) ON state. In the OFF state, in addition to the flow resistance of the inlet and outlet diffuser elements, the check valves block the flow of fluid through the microchannel. On the other hand, in the ON state, the electrostatic actuation of the diaphragms causes the check valves to separate and enables the induction and expulsion of fluid through the microchannel.

microdevices. The FEM multiphysics provides a rapid and inexpensive design evaluation, geometry independent resolution and the ability to seamlessly incorporate multiple materials and different loading conditions. Furthermore, a comprehensive nonlinear transient loading and dynamic frequency characteristics of the microfluidics can be obtained with the inclusion of parameters such as structural spring force, squeeze film damping, fringing field, and intrinsic residual stresses, to simulate the test conditions.

In the current research the emphasis is on the design and optimisation of the novel microfluidic structure through the deflection analysis, both, to verify the functionality of the concept and to investigate the working range of the structure. Hence, the primary focus is on secure actuation caused by combining the electroacoustic and electrostatic mechanisms. The optimisation of the microchannel design is addressed by the consideration of the diaphragm materials with enhanced mechanical and surface properties, and rational and reproducible selection of air gap while integrating the SAW correlator with the microchannel. The contributions of electroacoustic correlation and electrostatic mechanisms to the microvalve design are analysed in detail in the following subsections.

4.3.2 Electroacoustic Correlation

The need to optimise and verify individual components of the microvalve in order to achieve the desired performance of the integrated assembled system is clearly evident. The FEM modelling and experimental validation of SAW correlator were considered first, as were discussed in the Chapter. 3. The use of SAW technology in general and correlation in particular bestows several benefits to the microvalve structure. The contributions of SAW filter technology include small size, passivity, low cost, high reliability, more robustness, compact packaging, relatively stable performance over temperatures, ease of device fabrication for both low and high volume production. Furthermore, the use of SAW correlation provides remote discrete code addressability, low loss and sharp signal suppression from resonance to rejection band (high Q-factor). The next step would be to impart the measured correlator's response on the microchannel and analyse the electrostatic actuation.

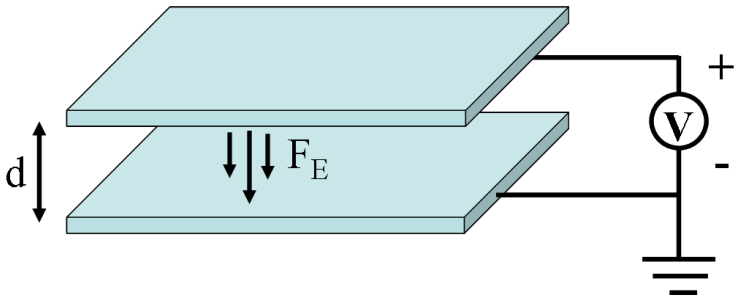

Figure 4.4. Parallel plate electrostatic actuator when driven by a voltage V results in the generation of an electrostatic force F_E.

4.3.3 Electrostatic Actuation

Electrostatic mechanism is one of the preferred methods of actuation for microfluidic devices due to fast response time, low power consumption, ease of integration, compatibility with other fabrication technologies and independency on the ambient temperature (Batra *et al.* 2007, Sounart *et al.* 2005). The electrostatic actuators utilise the induced forces between closely placed conducting plates/electrodes that are energised to different potentials, as shown in the Fig. 4.4. Using basic electrostatics, this force can be written as

$$F_E = \frac{\epsilon A_o}{2(d - \mathbf{a})} V^2. \tag{4.3}$$

Where, ϵ is dielectric constant of the plate material, A_o the overlapping area of the plates, V is the applied potential difference, d is the initial separation between the plates and $\mathbf{a}$ is the displacement of the moving plate from its initial equilibrium. This electrostatic force is significant in the micro scale and can deform one of the plates until they are balanced by the restoring elastic forces. Apart from the plate thickness and material type, the quadratic increase in the induced electrostatic force for decreasing distance between the plates determines the range of deflection. With the recent advances in micromachining techniques, the two plates can be placed very close to each other to generate a large field strength for moderate plate potentials. This is crucial for the current design where the wireless powering imposes tighter constraint on the voltage available for microvalve actuation. However, by varying the transmitted power levels the deflection range and therefore the ejected fluid quantity from the microvalve can be controlled.

Finite Element Formulation

The need for a careful design and optimisation of the electrostatically driven microchannel structure has lead to the use of FEM modelling. The finite element design formulation along with the ingrained differential equations are discussed here. The coupled field microchannel model is descretised into finite elements and solved by a three-field formulation. Here, in addition to use of structural elements and electrostatic elements for describing the conducting diaphragms and air gap respectively, a third field is introduced to account for the motion of the electrostatic mesh due to geometric and material nonlinearities.

According to electromechanical energy conservation principle (Avdeev 2003), the net flow of energy into the lossless system, due to applied loads, is offset by the internal change of energy stored in the system. Thus, the expression for equilibrium structural solution can be written as (Moaveni 2007 (3^{rd} Edition), ANS 2008):

$$\mathbf{F} = [M]\frac{\partial^2 \mathbf{u}}{\partial t^2} + [C]\frac{\partial \mathbf{u}}{\partial t} + [K]\mathbf{u}, \tag{4.4}$$

here, the mechanical force vector $\mathbf{F}$ comprises of two components, the nodal forces applied to the element $\mathbf{F}^N$ and the thermal force component $\mathbf{F}^{TH}$ given by

$$\mathbf{F}^{TH} = \int_{vol} [G]^T [D] \epsilon^{TH} d(vol), \tag{4.5}$$

where $[G]$ is the strain-displacement matrix determined by the element shape. $[M]$ is the mass matrix given by

$$[M] = \rho \int_{vol} [N]^T [N] d(vol), \tag{4.6}$$

where $[N]$ is structural shape function of the element and ρ is the density of the material used for the microchannel. $[K]$ is structural stiffness matrix expressed as

$$[K] = \int_{vol} [G]^T [D][G] d(vol), \tag{4.7}$$

where $\mathbf{D}$ is the electric flux density vector in the electrostatic domain. If $[N_E]$ is an electrical shape function of the element then the dielectric permittivity matrix $[K_d]$ is

$$[K_d] = -\int_{vol} [N_E]^T \epsilon [N_E] d(vol). \tag{4.8}$$

The dynamic equilibrium equation for an electrostatically actuated microchannel is influenced by the dissipated or stored mechanical energy of the structural elements

and the stored electrostatic energy of the electrostatic elements. A strongly coupled tetrahedral electrostatic element is used in this work to accurately model the electromechanical coupling. Based on the developed model geometry and design requirements, the structural equilibrium expression in Eqn. (4.4) can be modified to represent a electrostatic system (Moaveni 2007 (3^{rd} Edition), ANS 2008):

$$\begin{pmatrix} M & 0 \\ 0 & 0 \end{pmatrix} \begin{pmatrix} \frac{\partial^2 \mathbf{u}}{\partial t^2} \\ \frac{\partial^2 \mathbf{v}}{\partial t^2} \end{pmatrix} + \begin{pmatrix} C & 0 \\ 0 & 0 \end{pmatrix} \begin{pmatrix} \frac{\partial \mathbf{u}}{\partial t} \\ \frac{\partial \mathbf{v}}{\partial t} \end{pmatrix} + \begin{pmatrix} K & 0 \\ 0 & K_d \end{pmatrix} \begin{pmatrix} \mathbf{u} \\ \mathbf{v} \end{pmatrix} = \begin{pmatrix} \mathbf{F} + \mathbf{F}^E \\ \mathbf{L} \end{pmatrix}. \tag{4.9}$$

Here, the vector $\mathbf{L}$ represents the nodal, surface and body charges. $\mathbf{F}^E$ is the nodal electrostatic force, that contributed to the microchannel deformation, expressed as

$$\mathbf{F}^E = \int_{vol} [G]^T [\sigma^M] d(vol), \tag{4.10}$$

where $[\sigma^M]$ is the Maxwell stress tensor obtained from

$$[\sigma^M] = \frac{1}{2}(\mathbf{E_k}\mathbf{D}^T + \mathbf{D}\mathbf{E_k}^T - \mathbf{D}^T\mathbf{E_k}[I]), \tag{4.11}$$

$\mathbf{E_k}$ and $\mathbf{D}$ are the electric field intensity and electric flux density vectors, respectively, in the electrostatic domain and $[I]$ is the identity matrix. For the design analysis performed in this research, the complete solution is obtained via the solution of equation Eqn. (4.9).

As the electrostatic actuation involves the coupling of electrostatic and elastomechanic fields, any deformation in the microchannel would require a remeshing of the structure due to the nonlinear structural stiffness of the clamped diaphragms. This is carried out by using Newton-Raphson method (Lai 2007) where the non-linear system is iteratively solved for convergence using finite-differences.

$$\begin{pmatrix} \frac{\partial \mathbf{R}_s^i}{\partial \mathbf{u}} & \frac{\partial \mathbf{R}_s^i}{\partial \mathbf{v}} \\ \frac{\partial \mathbf{R}_e^i}{\partial \mathbf{u}} & \frac{\partial \mathbf{R}_e^i}{\partial \mathbf{v}} \end{pmatrix} \begin{pmatrix} \Delta \mathbf{u}^i \\ \Delta \mathbf{v}^i \end{pmatrix} + \begin{pmatrix} \mathbf{R}_s^i \\ \mathbf{R}_e^i \end{pmatrix} = 0. \tag{4.12}$$

Here $\mathbf{R_s}$ and $\mathbf{R_e}$ are discretized residual vectors of elastostatic and electromechanic field respectively for a nodal charge density of q_n, given by

$$\mathbf{R}_s(\mathbf{u}, \mathbf{v}) = \mathbf{F}(\mathbf{u}) - \mathbf{F}^E(\mathbf{u}, \mathbf{v}), \tag{4.13}$$

and

$$\mathbf{R}_e(\mathbf{u}, \mathbf{v}) = \epsilon_e(\mathbf{u})\mathbf{v} - q_n. \tag{4.14}$$

Where ϵ_e is the permittivity of the electrostatic field. The updated values of $\Delta\mathbf{u}^i$ and $\Delta\mathbf{v}^i$ for the ith iteration in Eqn. (4.12) are calculated from

$$\begin{pmatrix} \mathbf{u}^{i+1} \\ \mathbf{v}^{i+1} \end{pmatrix} = \begin{pmatrix} \mathbf{u}^{i} \\ \mathbf{v}^{i} \end{pmatrix} + \begin{pmatrix} \Delta\mathbf{u}^{i} \\ \Delta\mathbf{v}^{i} \end{pmatrix}. \tag{4.15}$$

For the solution to converge, Eqns. (4.12) and (4.15) are solved repeatedly until both residual vectors approach zero. The FEM modelling of the microchannel is discussed in the next section.

4.4 Microchannel Electrostatic Actuation

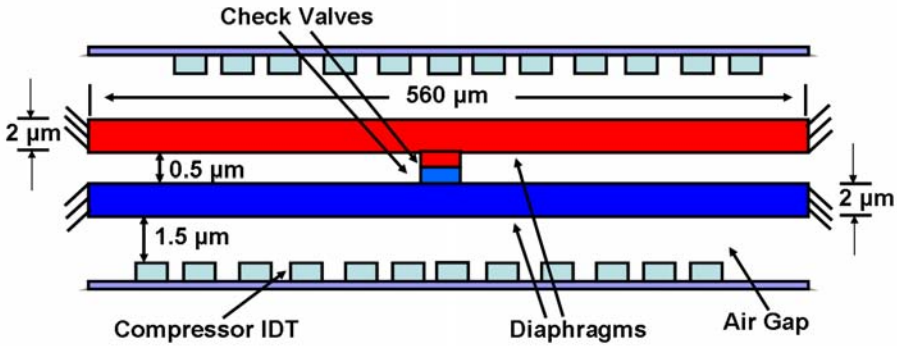

Figure 4.5. Microchannel electrostatic model comprising of two compressor IDTs and two conducting diaphragms with check valves. The medium between the diaphragms and IDTs is modelled as air.

The fast response times and the absence of friction in the electrostatic actuators make them an appropriate choice for high speed ultrasonic applications. However, the usage of electrostatic actuation to achieve moderate displacements is challenging in a wireless environment. This is mainly due to the tradeoff between the applied voltage and the gap between the electrodes. If the air gap between the diaphragm and the compressor IDT is increased then the required amplitude of the interrogating signal to actuate the microvalve becomes extremely high. On the other hand, if the air gap is small, the diaphragm might run the risk of shorting with the compressor IDT. Therefore, the usage of two identical SAW correlators with two diaphragms is a way of addressing this problem and hence optimising the microchannel deflection. As both the diaphragms are grounded the lack of electrical connections near or inside the channel provides electrical isolation of the fluid and simplifies channel sealing.

In the current microchannel model, as shown in the Fig. 4.5, the actuating field is between a 2 μm thick polyimide diaphragms and the output IDT of the correlators, separated by a 1.5 μm air gap. A biocompatible polyimide is chosen as the diaphragm material due to its high conductivity and low Young's modulus constant, as shown in Appendix. A. The length of the edge clamped diaphragms (560 μm) is determined by the length of the output IDT of the correlators. Short diaphragm lengths consume less die area and increase the actuator resonant frequency. Longer diaphragms, however, reduce operating voltage requirements (Galambos *et al.* 2008). While design rules limit how close a diaphragm can be to a SAW correlator, manufacturability issues limit the thickness of the diaphragm. The width of the microchannel is taken as 0.5 mm conforming with the overlapping area between the diaphragms and the compressor IDTs of the correlators. The flexible electrode or conducting diaphragm is electrically connected to ground, while the voltage at the fixed electrode or output IDT of the SAW correlator is determined by the input interrogating BPSK signal. In this work, the measured output voltage response of a 5×2 Barker sequence SAW correlator, as discussed in the previous chapter, is employed to drive the microchannel. The electrostatic force is generated due to the electric field between the interdigitated fingers and the diaphragms. Thus, this attractive force results in the centre deflection of the diaphragms towards the compressor IDTs of the correlators.

The demands for accurate modelling of the structure, replicating the physical conditions, and the strong dependence of microchannel deflection on the width of the diaphragm prompted the use of 3-D modelling. A meshed 3-D microchannel structure along with the compressor IDTs of the correlators is depicted in the Fig. 4.6. Tetrahedral elements with four degrees of freedom, three for displacement and one for potential, are used to model the diaphragms. The medium between the diaphragms and the IDTs is modelled by employing electrostatic elements for the direct coupled-field analysis.

4.5 Results and Discussion

The main objective in the evaluation of the microvalve is to measure the centre deflection of the microchannel when the correlator is interrogated with a matched and mismatched BPSK signal. This key parameter determines the working range of the microvalve. The interrogating code and acoustic mode dependent behaviour of the microvalve is studied using harmonic analysis. Furthermore, the displacement and the

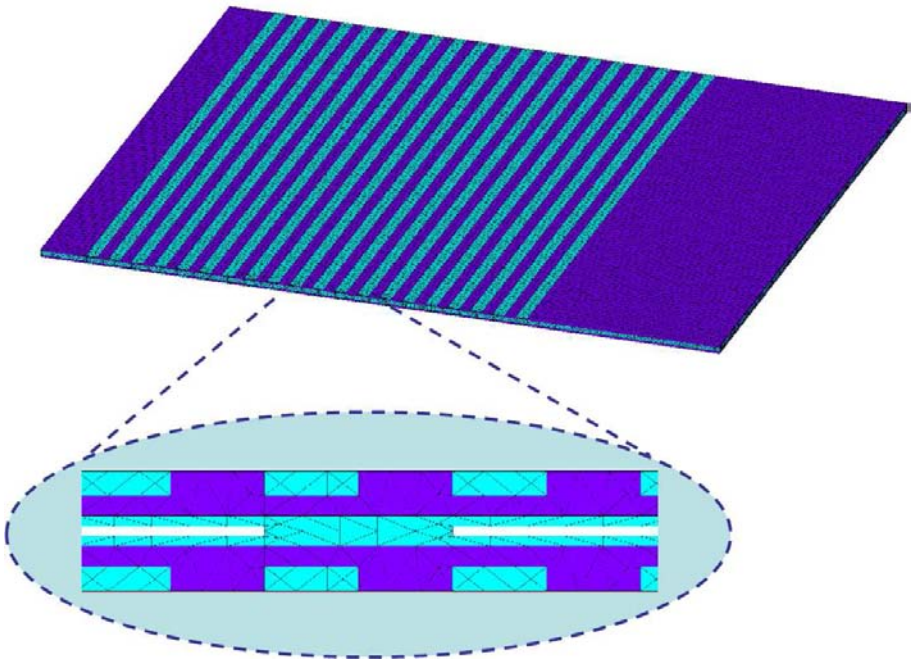

Figure 4.6. A 3-dimensional meshed microchannel structure with the check valves in the inset.

potential contours are employed to get a deeper insight into the microvalve actuation. In addition to analysing the nonlinear time response of the microvalve, the dynamic transient analysis assists in the investigation of other performance criteria of the structure such as microchannel opening dynamics and the microvalve loading time. This is performed by looping the electrostatic solution and the structural deformation till the convergence is attained, as outlined by the iterative Eqns. (4.12) and (4.15).

A fabricated 5×2 Barker sequence correlator is driven by a ±10V BPSK signal and the measured voltage response at the compressor IDT is utilised for the microvalve design. Fig. 4.7(a) shows the centre deflection of both the diaphragms in the y direction, when the code matches, for different acoustic modes determined by the excitation frequency. There, the curves labelled as U_y top and U_y bot correspond to the y-direction displacements of the top and bottom diaphragms, respectively. Substantial microchannel displacement can be observed in the vicinity of the excited modal frequencies of the correlator. Hence, the electrostatic analyses of the microchannel for a widely varying range of frequencies acts as an effective method for displacement optimisation. This can be used to pick the operating mode of interest for displacement optimisation. From Fig. 4.7 (b), a maximum separation of the check valves of 0.59 μm can be observed at the SAW mode at 79 MHz. The y-displacement contour and the electric potential

contour of the check valves at the same modal frequency is shown in Fig. 4.8 to analyse the microchannel opening. Here, the separation between the check valves can be observed. Even though this displacement is small compared to thermal and piezoelectric bimorph actuators, the high frequency operation of the microvalve results in high particle velocities (Kaajakari *et al.* 2001). The diaphragm deflection can be further increased by employing corrugated diaphragm structures (Dissanayake *et al.* 2009) or by considering correlators encoded with a longer code, which in turn increasing the diaphragm length. This could not be implemented in the current work due to the huge

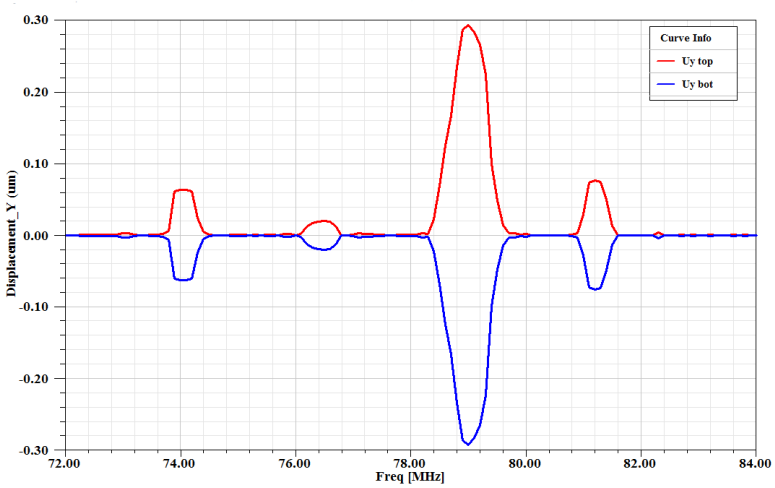

(a)

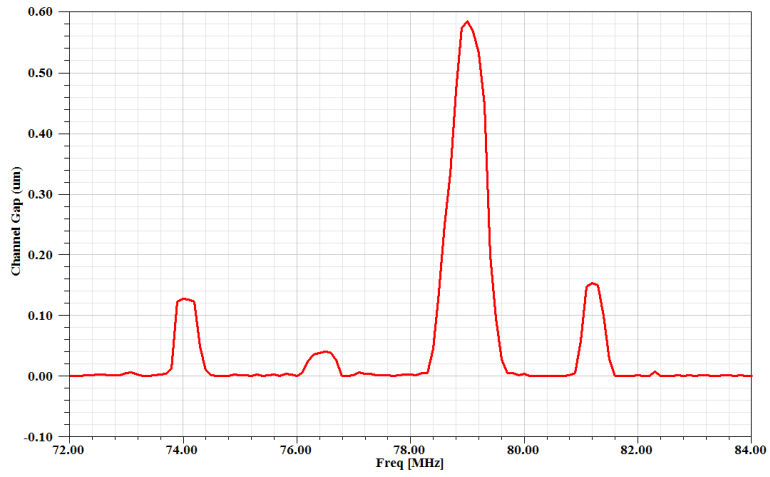

(b)

Figure 4.7. A frequency sweep of the centre deflection of the two diaphragms, when the code matches, for various acoustic modes (a) in the y direction. (b) the channel separation between the check valves.

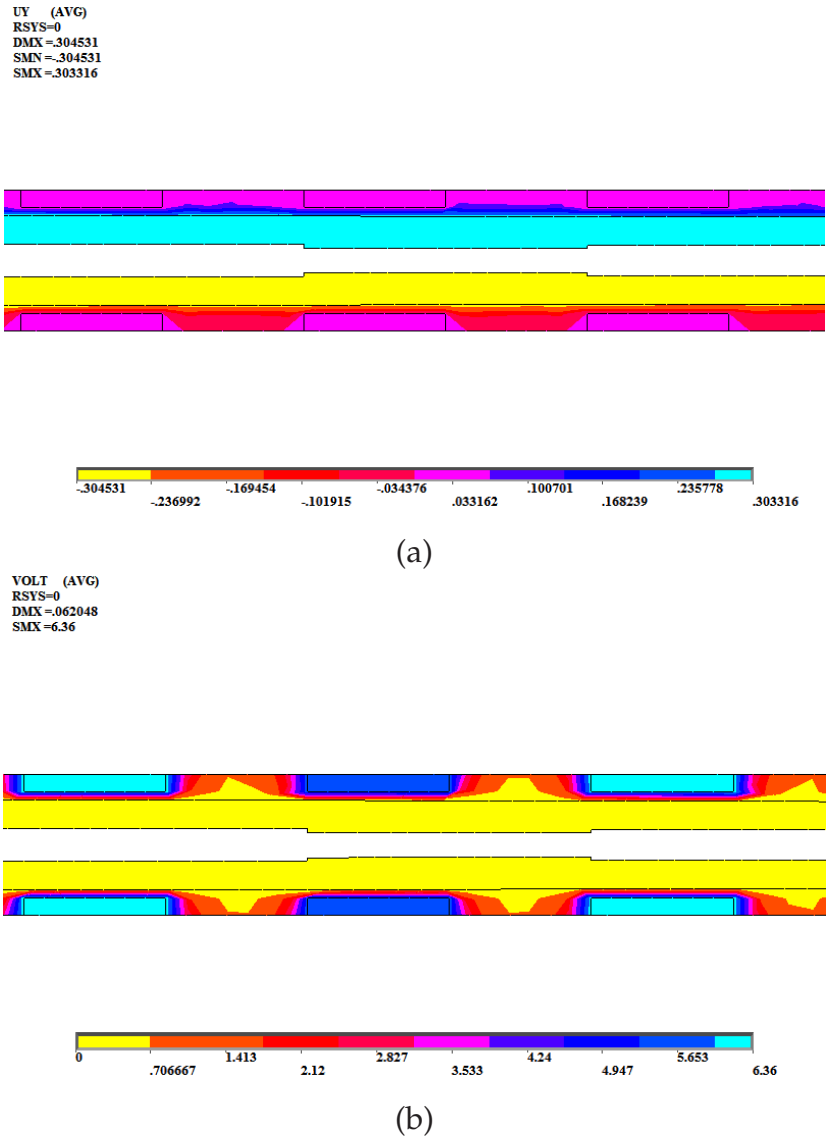

Figure 4.8. Contour plots of the check valves at SAW modal frequency. (a) Y-displacement contour. (b) Electric potential contour.

constraint imposed by such a microvalve modelling technique on the available computational resources.

In addition to the harmonic analysis, a dynamic transient analysis of the microchannel is carried out to develop a complete nonlinear finite element model. With this analysis, the transient microchannel deflection and the microvalve loading time are derived by interrogating the microvalve with a continues sequence of matched BPSK signal at SAW modal frequency. Fig. 4.9 depicts the transient centre deflection of both the diaphragms in the y-direction for a period of 3.5 microseconds. The deflection is very low initially due to the time taken by the surface acoustic wave to propagate from the

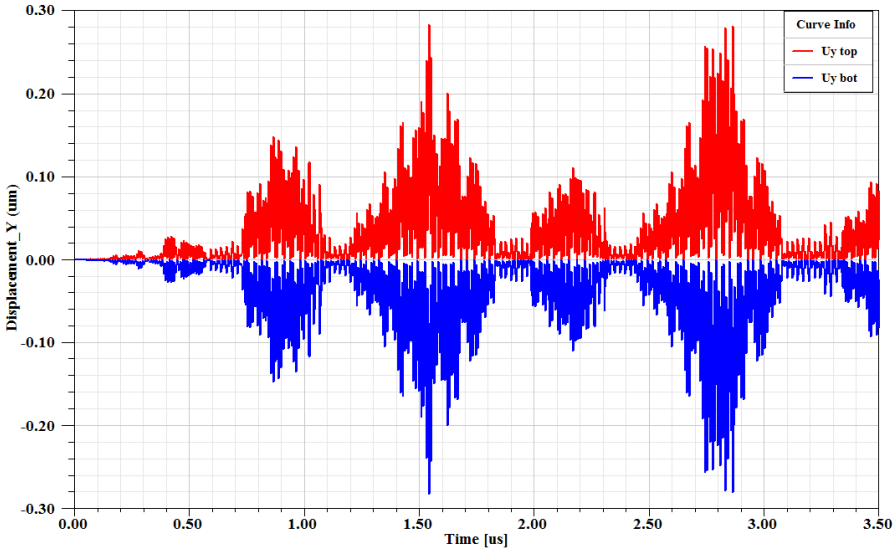

Figure 4.9. Transient centre deflection of two diaphragms in the y direction, when the code matches, at SAW modal frequency. The microvalve loading time of of 650 ns can be observed.

input IDT to the compressor IDT of the correlator. Moreover, the mismatched filling of the correlator caused by the non-synchronisation between the coded acoustic wave and the encoded electrodes of the compressor IDT contributes to this delay. From the instance when the synchronous filling of the correlator occurs the microvalve stabilises, as can be observed from the Fig. 4.9 is after 650 ns. After this time the electrodes of the compressor IDT pick up the coded acoustic waves synchronously and hence a consistent deflection peaks can be observed from then on.

So far the results are confined to the instance when there is a code match between the input BPSK signal and the compressor IDT of the correltor. The functionality of the microvalve can only be verified by observing the microchannel deflection to a mismatched input code. This was carried out by driving the physical correlators with mismatches BPSK signals and imparting the measured response to the microchannel structure. The response of the structure to two different codes, a delayline input and other non-correlating input, at the SAW mode of interest is provided in Fig. 4.10. All the other specifications of the model are kept the same except for the mismatched input code.

By comparing these responses with the correlating microchannel deflection response of the Fig. 4.7 it can be established that in addition to the excitation frequency, the microvalve's response is determined by the code in the RF signal. Even in the case of a

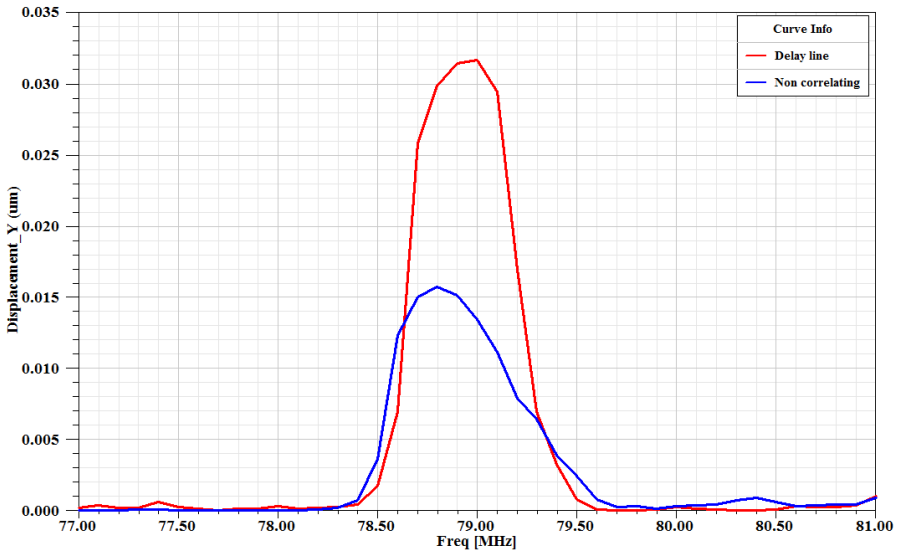

Figure 4.10. The channel gap between the check valves when the code mismatches for a (a) delayline input (b) noncorrelating input.

delay line input, when the two codes are very similar, the device response is much less than its response to the matched code, as can be seen from Fig. 4.10.

4.6 Conclusion

The chapter presented the design and simulation of a novel wireless active microvalve by taking into account both the electroacoustic and electrostatic mechanisms in a single finite element run. The requirements placed by the current and emerging biomedical applications on these devices such as small size, passivity, and remote interrogability are taken into consideration. The results discussed in this chapter include: (i) comprehensive FEM formulation of 3-Dimensional, 5×2-bit Barker sequence SAW correlator driven microchannel, (ii) detailed study of the harmonic and dynamic transient microchannel deflection caused by electrostatically coupling the output IDT's of the SAW correlators to the microchannel and (iii) analysis of the difference in microchannel deflection when there is a code mismatch and a code match. It is concluded that the model appropriately represents the interrogating signal code dependent, and the excited acoustic mode dependent operation of the microvalve and hence enabled the analysis of the microchannel deflection. In consideration of such actuation analysis by the developed FEM model, a microfluidic device with more optimal performance is expected to be designed for various applications. The design and development of a

telemetry system for the proposed novel microvalve is presented in the next chapter (Chapter 5).

Chapter 5

Wireless Telemetry System for the Implanted Microvalve

5.1 Introduction

The culmination of rapid advances made in the areas of microelectromechanical systems (MEMS), nanotechnology and biomedical engineering have resulted in the expansion of their horizons in modern medicine for the deployment of implantable devices as diverse as pacemakers, retinal and cochlear implants, physiological recording devices, muscle stimulaters, and drug delivery devices (Mokwa 2007, Loizou 1999, Mercanzini *et al.* 2005, Russold and Jarvis 2007). Most of these devices employ nonregenerative power sources, i.e they are powered through batteries or wires, thus restricting their mobility, compactness and lifespan (Li *et al.* 2007a, Grayson *et al.* 2004, Amer and Badawy 2005, Geipel *et al.* 2007, Cook-Chennault *et al.* 2008). Moreover, the development of a remotely powered and securely interrogated microactuator has not been fully exploited. Hence, a wireless controlled, Surface Acoustic Wave (SAW) correlator driven, passive microvalve is highly desirable. Numerical applications can be envisaged as such a device is light, reliable, chemically stable, enables high patient mobility, and not limited by the lifetime of the battery. However, designing a telemetry system for such a microvalve is challenging as the small size of the device needs to be matched by a miniature antenna. In addition to the restriction on the receiving antenna size, the impact of the lossy human tissue on the attenuation, and antenna efficiency degradation determine the practicability of remotely powered implant system.

Optimum design of the contactless powering and wireless telemetry for the microvalve, being unique to the device specifications, necessitates a thorough understanding of the electromagnetic propagation around and inside the human body. This includes the

modelling, characterisation and development of a reliable communication link specific to the device dimensions, surrounding environment, substrate material and, electrical and mechanical conformity with the structure. Inductively coupled RF telemetry is an optimal method for both power supply and data transmission in long term artificial implants due to small size, high reliability, and extended life span of the device. Furthermore, inductive coupling relies on the propagation of magnetic fields which are subjected to minimal attenuation in the biological tissues. Wireless transfer of power based on inductive coupling has been extensively investigated in the past (Lu *et al.* 2007, Si *et al.* 2008, Basset *et al.* 2007, Wang *et al.* 2004). However, most of these systems are incompatible with the proposed microvalve due to their large physical dimensions and the requirement to build such antenna on a piezoelectric substrate to maintain a small device size and reduced device complexity. Furthermore, the use of integrated electronics technology in previous designs would not comply with the passivity requirement of the implanted microvalve. Hence, there is a need to custom design a receiver coil with high coupling efficiency to maximise the amount of power harvested by the implant. Moreover, the common approach of treating the receiver and transmitter coils separately for design optimization cannot be applied to the current model (Neagu *et al.* 1997, Renauda *et al.* 2002, Vergara *et al.* 2007). This is because the generation of magnetic field pattern and the power coupling through the media representing human tissue are significant for holistic link budgeting.

The numerical and experimental analysis of the biotelemetry link for the microvalve is undertaken, in this research, using numerical and physical human body phantoms. To accurately account for the path losses and to address the design optimisation, the receiver coil/antenna is solved simultaneously with the transmitter coil/antenna in the presence of human body simulant using 3-dimensional, high frequency electromagnetic FEM modelling. This modelling of the whole system, which accounts for the radiation properties of the antennas and signal attenuation by the human body, is feasible because of the short distance between the reader and implanted antennas. Such a holistic and comprehensive FEM modelling of the telemetry link, for human implants, has not been reported in the open literature. To validate numerical calculations, the miniature antenna is fabricated on a 128° YX $LiNbO_3$ piezoelectric substrate whereas the reader antenna is fabricated on a FR-4 substrate. The received relative signal strength is numerically and experimentally derived for a miniature ($6\times6\times0.5$ mm), square spiral antenna/coil when interrogated by a handheld $8\times5\times0.2$ cm square spiral antenna/coil in the near field. This investigation is performed for a frequency range

between 10 and 100 MHz, while the two antennas are separated by a human body simulant of 5 cm thickness, as shown in Fig. 5.1. The S_{12} response of the coils is analysed from the simulated telemetry link both to maximise the transmitted power at the implanted coil, through the optimisation of mutual inductance, and to investigate an appropriate transmitter-receiver coil layout. Thus, the numerical analysis enables the design of an efficient and reliable contactless power transmission. Furthermore, the study of the variation in power transfer due to changes in the orientation of the coils, which is important for moving load applications, is also considered. This is carried out by tilting the transmitter coil by an angle and analysing the drop in received relative signal strength, influenced by the reduced flux linkage between the misaligned coils. Finally, the experimental results confirm well with the FEM analysis predictions and hence ascertain the applicability of the developed system for secure interrogation and remote powering of the proposed microvalve.

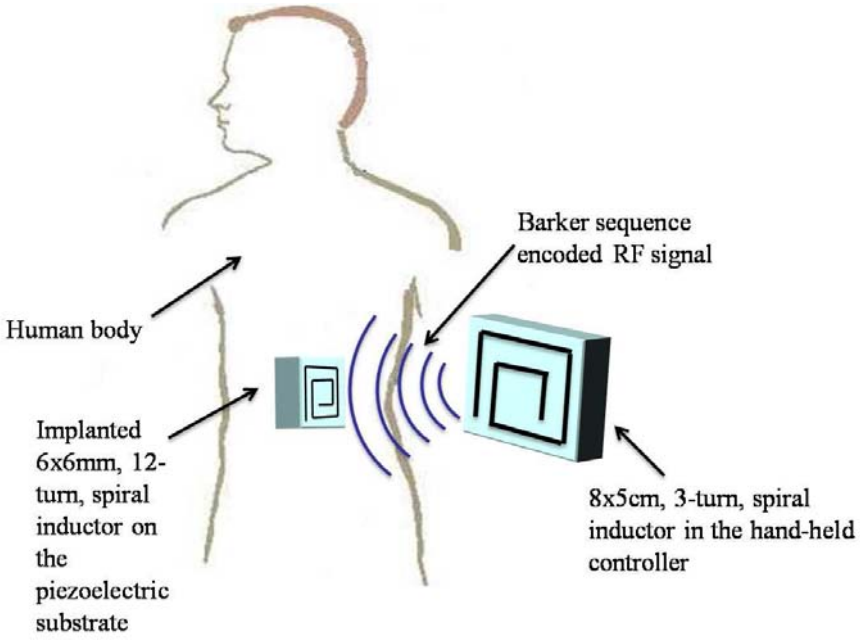

Figure 5.1. Inductive powering system of a wireless microvalve with an implanted coil/antenna and a transmitter coil/antenna (Note: Figure not to scale).

In this chapter, the design and experimental validation of an inductive power transmission link for a wireless controlled microvalve is presented. In Section 5.2, the requirements placed on the telemetric link due to the mechanical and electrical conformity with the SAW correlator, biomedical application and reproduction of the operating

environment, are discussed. In Section 5.3, a description of the transmitter receiver architecture of the microvalve is provided. Then in Section 5.4, the inductive link design including the layout and geometry of the handheld and implant inductors, equivalent circuit and FEM modelling is presented. The simulation and measurement results comprising the quality factor, effective inductance, and relative signal strength in the frequency domain are outlined in the section 5.5. Furthermore, the variation of the power transfer capabilities due to the tilting of the antennas is also discussed in the same section.

5.2 Design Considerations

As the demand for miniaturisation grows, inductive coupling approach could be a strong candidate for meeting the power and bi-directional data communication requirements of future implants. The benefits offered by this technology such as, the elimination of battery or feed through wires, ease of implantation, increased portability, and higher chemical stability, have the potential to unfold many innovative biomedical applications. A basic inductive link comprises of two coils, primary and secondary, resembling a loosely coupled transformer. When the coils are in close proximity, the magnetic field generated by the primary coil, placed outside the body, is partly picked up by the implanted secondary coil. Here, the magnetic field is strengthened at the interface between the body and the air and also passes with minimal hindrance, compared to the electric field, through the biological media (Ahmadian *et al.* 2003). Hence, the use of magnetic antennas/coils restricts the transmission losses to a permissible limit. There are a number of design considerations for a telemetry link which are strongly determined by the application. Here, for the wireless actuation of a SAW correlator driven microvalve, the important ones are: the mechanical and electrical conformity with the SAW correlator, restrictions imposed on the implanted microvalve, and recreation of operating environment, as are outlined in detail in the current section.

5.2.1 Inductive Coupling of a SAW Correlator

Contactless near-field powering of SAW devices was previous employed to avoid the usage of bonding wires and hence to improve the mechanical robustness and temperature sensitivity in sensing applications (Luo 2004). By designing the SAW device's

IDTs as an integral part of the secondary coil/antenna, RF energy is inductively coupled through a primary coil in close proximity.

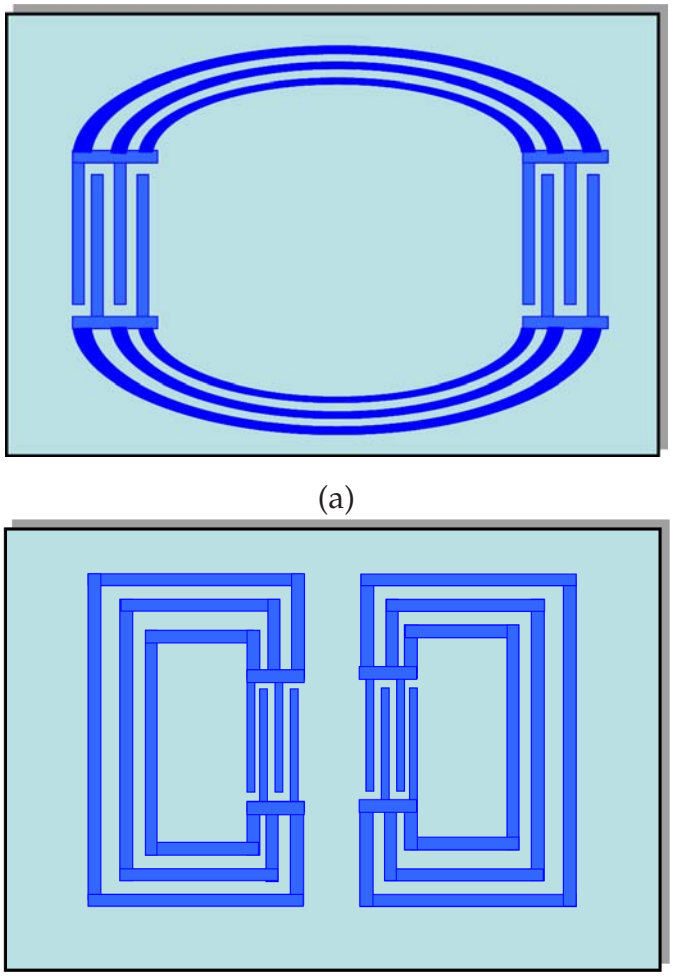

Figure 5.2. Inductively coupling SAW devices for a (a) one-port configuration. (b) two-port configuration.

Beck *et al.* (1998) and Wagner and von Schickfus (2001) have proposed two designs for connecting the coils to the busbars of the IDTs, as shown in Fig. 5.2. The configuration in Fig. 5.2.(a) is for a one-port device which is electrically equivalent to an inductor connected in series with two IDTs. When interrogated by the primary coil, each IDT excites a SAW in the direction of the opposite one. As the SAWs reach the opposite IDTs they are transduced to RF signal and retransmitted back to the primary coil. This configuration is suitable for reflection measurement using a network analyzer. The two coil configuration shown in Fig. 5.2.(b) is for transmission measurement. Due to the absence of the reflected SAW in the second coil it is applicable for oscillator

applications. The first configuration is not suitable for the SAW correlator as it is a two-port device and the second configuration, however, is available at a increased chip surface area. As the device size is an uncompromisable factor in the microvalve design, there is a need to develop a new coil layout for the SAW correlator which enables a higher level of miniaturisation. This area limitation is addressed in the current research by printing the inductor on the bottom side of the piezoelectric substrate of the SAW correlator, as will be discussed in detail in the next section.

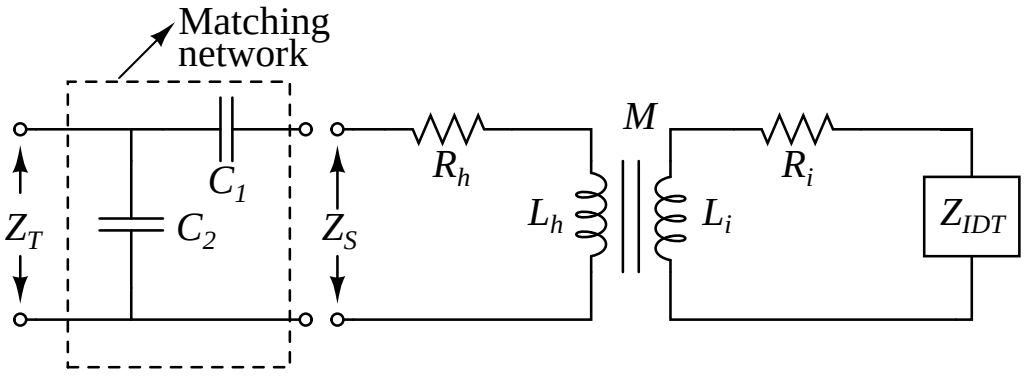

Figure 5.3. Equivalent circuit of the inductive link when coupled to a SAW correlator. It comprises of a matching network, primary coil, and secondary coil connected to the input IDT of the SAW correlator.

There is a need to optimise the impedance of the SAW based inductively coupled system both to minimise the electrical-acoustic transduction losses and to match it's impedance with the external RF components connected to the primary coil. Fig. 5.3 depicts the equivalent circuit of the inductive link with the secondary coil connected to the input IDT of the SAW correlator. Here, R_h and L_h are the ohmic resistance and inductance of the primary/handheld coil, respectively, and R_i and L_i are the ohmic resistance and inductance of the secondary/implanted coil, respectively. The impedance (Z_{IDT}) of the input IDT of the SAW correlator can be obtained from the expression of IDT admittance given in Eqns. (2.27) - (2.29), such that

$$Z_{IDT} = \frac{1}{A_{33}} = \frac{1}{A_{33}^M + A_{33}^E}, \tag{5.1}$$

where

$$\begin{aligned} A_{33}^M &= -\frac{4\alpha^2(\delta+\kappa)}{n^3}\frac{(\delta+\kappa)(1-\cos(nL)) - jn\sin(nL)}{n\cos(nL) + j\delta\sin(nL)}, \text{and} \\ A_{33}^E &= -j(\frac{4\alpha^2}{\delta-\kappa}L - \omega LC). \end{aligned}$$

The primary and secondary coils represent a loosely coupled transformer and hence the total impedance of the system (Z_S) is given by

$$Z_S = R_h + j\omega L_h + \frac{\omega^2 M^2}{R_i + j\omega L_i + Z_{IDT}}. \tag{5.2}$$

Here M is the mutual inductance between the coils. In order to match the impedance of the secondary coil with the external RF components and control the coils resonant frequency, capacitors C_1 and C_2 are placed in series and parallel to the SAW correlator, respectively. The total impedance (Z_T) of the system after impedance matching is

$$\frac{1}{Z_T} = j\omega C_2 + \frac{1}{Z_S + \frac{1}{j\omega C_1}}. \tag{5.3}$$

An in depth inductive link analysis, specific to the chosen coil geometries, is be presented in Section 5.4.

5.2.2 Biomedical Application

The efficiency of the telemetry link of the microvalve is strongly dependent on the intended application. For biomedical applications, the location of the microvalve in the body, the required actuation and fluid flow rate heavily influence the selection of inductive link specifications such as the antenna size, separation between the microvalve and the handheld controller, power consumption, electromagnetic radiation absorption, implant lifetime, data bandwidth, and biocompatibility (Hall and Hao 2006). The choice of the size of the microvalve and hence the implant antenna is guided by the aim to minimize its impact on the body and enhance the free movement of the subject. Furthermore, it is mandatory to keep the power consumption of implant to as low as possible for two reasons. First, to enable a practicable separation between the antennas, and second to reduce the heat dissipation into the surrounding tissues.

The other important design consideration for human implants is the level of electromagnetic exposure to a human body. For instances, where small areas of the body are exposed to the radiation, the field distribution is determined by factors such as the dielectric properties of the biological tissues, the physical geometry of the body, and orientation of electric and magnetic fields (Osepchuk and Petersen 2001). The IEEE C95.1-1991 (*IEEE standard for safety levels with respect to human exposure to radio frequency electromagnetic fields, 3 kHz to 300 GHz 1999)* provides the safety standards for human exposure to electromagnetic energy in the frequency range of

Table 5.1. Maximum permissible human exposure to electromagnetic field in a controlled environment (*IEEE standard for safety levels with respect to human exposure to radio frequency electromagnetic fields, 3 kHz to 300 GHz 1999*). Here, f is the frequency in MHz.

Frequency range (MHz)	Electric field strength (E) (V/m)	Magnetic field strength (H) (A/m)	Power density (S_P) E-field, H-field (W/cm^2)
$0.1-3.0$	614	$16.3/f$	$(0.1, 10/f^2)$
$3-30$	$1842/f$	$16.3/f$	$(0.9/f^2, 10/f^2)$
$30-100$	61.4	$16.3/f$	$(0.001, 10/f^2)$
$100-300$	61.4	0.163	0.001

3 kHz to 300 GHz. The bioeffects, which are predominantly thermal, can be reduced by adopting the standard guidelines for the electric and magnetic fields, and power densities given in Table 5.1. The values in Table 5.1 are limited to the vicinity of operating frequencies of interest for the microvalve in consideration.

Finally, biocompatibility is another vital consideration for implants. This is to ensure that the microvalve causes no damage to the surrounding tissues nor is it affected by the properties and actions of the body. The interface of the microvalve with the body can be enhanced with biocompatible coating (Potkay 2008). On the other hand, the microvalve must be designed to withstand the diffusion of substances into the body, and the attachment of connective tissues. This is possible by isolating the internal components of the microvalve with hermetic sealing.

5.2.3 Human Body Phantom

Body-centric communication systems, such as the one being considered for the microvalve, necessitates a thorough understanding of the electromagnetic wave interactions with the human tissues. This is because the wave propagation from the handheld controller through the air, into the body, and to the implanted microvalve is strongly influenced by the surrounding conductive, lossy body media. Hence, there is a need to account for the variations in efficiency and directivity, caused by the tissues, in the system design and link budget calculations.

Table 5.2. Dielectric properties of muscle tissue.

Frequency range (MHz)	Relative dielectric constant (ϵ_r)	Conductivity (σ) S/m	Penetration depth (δ_p) cm
1	411	0.59	70
10	131	0.68	13.2
100	79	0.81	7.7
1000	60	1.33	3.4

When the antenna is operating in non-conducting environment such as air or vacuum, the permittivity of the medium is $\epsilon_0 = 8.86\times10^{-12}$ f/m. However, the permittivity becomes a complex quantity for conducting medium such as human tissue, and is given by

$$\epsilon_t = \epsilon_r\epsilon_0 + j\frac{\sigma}{\omega}. \tag{5.4}$$

Here, ϵ_r and σ are the relative dielectric constant and conductivity of the lossy medium, respectively. The attenuation of the electromagnetic wave traveling towards the implanted microvalve is determined by the penetration depth of the tissue. The penetration depth (δ_p) is the depth at which the field strengths or induced current densities have been attenuated by a factor of $1/e$ of their initial value at the boundary of the medium. It is given by (Osepchuk and Petersen 2001)

$$\delta_p = \frac{1}{\omega}\left[\sqrt{\left(\frac{\mu_0\epsilon_r\epsilon_0}{2}\right)^2 + \left(\frac{\mu_0\sigma}{2\omega}\right)^2} - \frac{\mu_0\epsilon_r\epsilon_0}{2}\right]^{-\frac{1}{2}}. \tag{5.5}$$

Where, $\mu_0 = 4.7\times10^{-}7$ Vs/Am is the permeability of vacuum. A comprehensive investigation of the dielectric properties of various tissues of the body was undertaken by Gabriel *et al.* (1996) in the frequency range from 10 kHz to 10 GHz. These dielectric properties are widely used in the design of body-centric and on-body communication systems and are even employed in the Australian *Radiocommunications (Electromagnetic Radiation - Human Exposure) Standard* (2003). The relative dielectric constant, conductivity, and penetration depths of the muscle tissue are outlined in Table 5.2 for the operating frequencies of interest.

The magnetic field is less affected by the body tissue at low frequencies and hence, as can be seen in the Table 5.2, the penetration depth is high at these frequencies. If the microvalve is to operate between 10-100 MHz then the penetration depth would be in the range of 13.2-7.7 cm, respectively. As the body supports communication

Table 5.3. Body tissue recipe for liquid phantom.

Ingredients	% by weight
Water	52.5
Sugar	45.0
Salt (NaCl)	1.4
Hydroxyethyl Cellulose (HEC)	1.0

channels, these are practicable depths for the envisaged biomedical application of the microvalve. Furthermore, these depths are higher than 5 cm, which appear to be the commonly employed gap in body-centric communications (Hall and Hao 2006). The ϵ_r and σ of the lossy tissue medium further impact the speed of propagation of the electromagnetic wave in the medium. The change in wavelength (λ_t) is given by (johansson 2004)

$$\lambda_t = \frac{\lambda}{\sqrt{(\epsilon_r)^2 + \left(\frac{\sigma}{\omega\epsilon_0}\right)^2}} Re\left[\sqrt{\epsilon_r + j\frac{\sigma}{\omega\epsilon_0}}\right]. \tag{5.6}$$

As it is not always possible to design and verify the functionality of the telemetry link in the presence of actual tissues, human body phantoms are widely used in medical research both for safety analysis and for the development of novel diagnosis and treatment techniques (Izdebski *et al.* 2009). A numerical biological body or a physical model epitomising the characteristics of the biological tissues is referred to as phantom (Hall and Hao 2006). In contrast to the human subjects, the phantoms provide a stable, long lasting, controllable, and easy to produce and use propagation environment. The phantoms can be broadly classified into numerical and physical types. Different modelling techniques, such as ray tracing, method of moments, finite-difference time-domain (FDTD) method, and finite element method (FEM) are currently being used for numerical phantoms (Hall and Hao 2006). On the other hand, the physical phantoms can be further classified as solid (dry), semisolid (gel), solid (wet), and liquid (Hall and Hao 2006). The numerical and physical phantoms are employed for simulations and measurements, respectively. The choice of a type of phantom is generally guided by the application.

FEM modelling approach was used in the current research both for the simulation of the muscle tissue and the design of the telemetry link as a whole. This is to take advantage of the versatility and accuracy offered by that technique, as was discussed extensively in the previous chapters. For measurements, liquid phantom was employed in this work. Liquid mixtures have been developed by Hartsgrove *et al.* (1987) to represent the dielectric properties of various parts of the body. The same article is referenced in the Australian *Radiocommunications (Electromagnetic Radiation - Human Exposure) Standard (2003)* for outlining the recipes for simulation liquids representing the human brain and body tissues. The composition of water, sugar, salt and, hyroxyethyl cellulose (HEC) for human body tissue is presented in Table 5.3.

5.3 Transmitter Receiver Architecture of a Wireless Powered Microvalve

The design of a communication system for an implant is unique to the implant function required. A brief description of the SAW correlation based telemetry system for the microvalve, as shown in the Fig. 5.4, is provided here. A coded SAW based communication system consists of an expander IDT in the handheld controller and a compressor IDT in the implanted receiver. In the handheld controller, a narrow pulse or a sinusoidal waveform is fed to the expander IDT to generate a coded acoustic signal depending on the geometry of the expander IDT. These acoustic waves propagate through the substrate to the transmitting IDT, which transforms these coded acoustic waves to electrical coded RF signals. The output from the transmitting IDT is fed to an amplifier, to strengthen the signal, and then to a transmitting antenna. The front-end of the implanted microvalve consists of a correlator with its input IDT connected to a receiving antenna/coil to intercept the transmitted coded RF signal. The microvalve will be actuated only when the code of the interrogating RF pulse matches the embedded code in the output IDT. A more detailed description of the SAW correlator and the microvalve operation was presented in Chapters. 3 and 4, respectively.

The selection of the transmitter antenna is guided by the need to optimise the power transmission by taking into consideration the influence of the human body. As the magnetic field increase at the boundary between air and body, and the magnetic reluctance of the biological tissues is low, it is advantageous to establishing an inductive link using magnetic antennas (Ahmadian *et al.* 2005). Coils are the preferred choice of

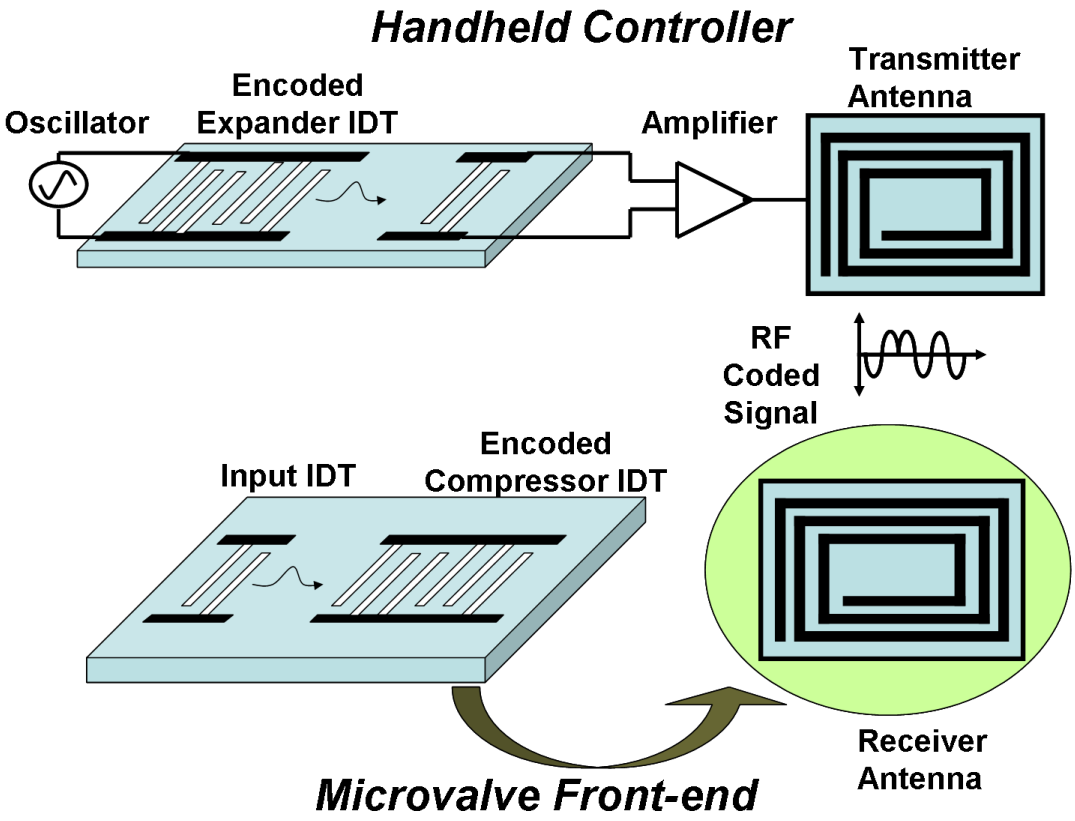

Figure 5.4. SAW correlator based microvalve transmitter receiver configuration. The handheld controller generates a RF coded signal that securely powers the microvalve when there is code match.

magnetic antennas due to their compactness and low ohmic losses. On the microvalve side, the receiver coil is printed on the bottom surface of the correlator to ensure optimum space utilisation. Moreover, the conformity of the coil shape with the implant makes it immune, to a large extent, from the mechanical properties of the microvalve.

The requirements placed by the implanted microvalve on the receiver coil have to be analysed to design an effective inductive link with optimum power transfer. The most critical factors are the physical dimension and operating frequency of the coil. The dimension of the implanted coil and the operating frequency are determined by the SAW correlator in the microvalve. As the SAW correlator is built to operate at $50-100$ MHz on a square die with a physical dimension of 7.5×7.5 mm, the same limitations are placed on the receiver coil. The handheld controller and the implanted microvalve are in close proximity, usually 5 cm apart. As this distance is short compared to the electromagnetic wavelength, corresponding to microvalve operating frequency range

of 50−100 MHz, the system operates in the near field. Here, the electromagnetic field can be considered as magnetic alternating field resulting in reduced propagation path losses. The design of an inductive powering system which is complaint with the above mentioned specifications is discussed in the next section.

5.4 Inductive Link Design

The modelling of inductive coupling between the transmitter and receiver coil is mathematically equivalent to the resolution of the electromagnetic field equations for a given excitation and separation. The various inductive powering design approaches in the literature seem not to fully address the modelling of transmitter coil and the receiver coil simultaneously. A common practice has been to ignore the generation of magnetic field pattern by treating the two coils separately or to make use of empirical rules (Kim and Rahamat-Samii 2006, Theodoridis and Mollov 2005). However, for the current application, where high coupling sensitivity and efficiency are needed, modelling and optimisation of the complete system in the presence of human body simulant is necessary. The Finite Element Method (FEM) is one of the most accurate methods of modelling the inductive link as the complete set of electromagnetic field equations is solved at radio frequencies in a 3-dimensional environment. Thus, an accurate evaluation of the effect of lossy human tissue, radiation and parasitic reactance is possible with this versatile technique. Moreover, the strong dependence of the loosely coupled power transmission link performance on the trace metal thickness, line width, substrate material, number of turns, spacing between turns, impedance of the load, and the operating frequency provides a realistic prediction of the telemetry systems response when excited by a RF signal. A 3-dimensional inductive link modelling was carried out using HFSS; a commercially available electromagnetic finite element package. The system, as shown in the Fig. 5.1, comprises of a transmitter antenna/coil and a receiver antenna/coil on a piezoelectric substrate, separated by a human tissue simulant.

5.4.1 Implanted Coil/Antenna

The design of an implantable antenna determines the radiation dependent mutual inductance and power transfer efficiency of the system and therefore is a critical step

in the modelling of the telemetry link. It is preferable to use a square spiral geometry due to ease of manufacturing, optimum utilisation of the piezoelectric substrate area, and tolerance to coils misalignment during coupling (Bahl 2003). In addition to possessing a reliable inductance, this conformal geometry provides a minimum mechanical interference with the microvalve structure. As the physical dimensions of the implanted coil are restricted to those of the die of the SAW correlator, which in this case is 7.5×7.5 mm, there is a limit placed on the self-inductance of the coil and hence the mutual inductance. The reduction of spacing between the turns enables the dominant current vectors to be in phase and thus increases the self inductance of coil. Furthermore, a high value of quality factor, which is the ratio of the magnetic energy stored to the power dissipated, is desirable for an implant antenna. As the quality factor is inversely proportional to the sheet resistance of the metal coil it can be enhanced by increasing the coil thickness and conductivity. On the other hand, having a high quality factor for the implant coil could be a problem because of the detuning effect, which causes a significant drop in transmission efficiency for a minor variation in operating frequency.

Fig. 5.5 depicts the square spiral geometry and the lumped equivalent circuit for characterising that geometry. Here, L_i, R_i and C_i are the inductance, sheet resistance, and loss capacitance, respectively, of the implant coil. Various expressions are available in the literature to analytically predict the inductance of spiral structures (del Mar Hershenson *et al.* 1999). Recently, Mohan *et al.* (1999) have presented three simple expressions for calculating the inductance of spiral coils. The accuracy of these expressions was validated by using a large number of three-dimensional field solver results and measurements. As an accuracy of $97-98$ % was reported, when compared with three-dimensional field solver and measurement results, any of these inductance expressions is suitable for the lumped equivalent circuit model of the implant coil. The first expression is a modified Wheeler equation given by

$$L_{i1} = K_1 \mu_0 \frac{n^2 l_{avg}}{1 + K_2 æ}. \tag{5.7}$$

Here l_{avg} (given by $0.5(l_{in} + l_{out})$) is the average diameter of the square spiral, $æ = (l_{out} - l_{in})/(l_{out} + l_{in})$ is the fill ratio, n is the number of turns, and K_1 & K_2 are the spiral shape dependent Wheeler coefficients, outlined in Table 5.4.

The second expression is based on current sheet approximation, where the sides of the square spiral are approximated as symmetrical current sheets of equivalent current

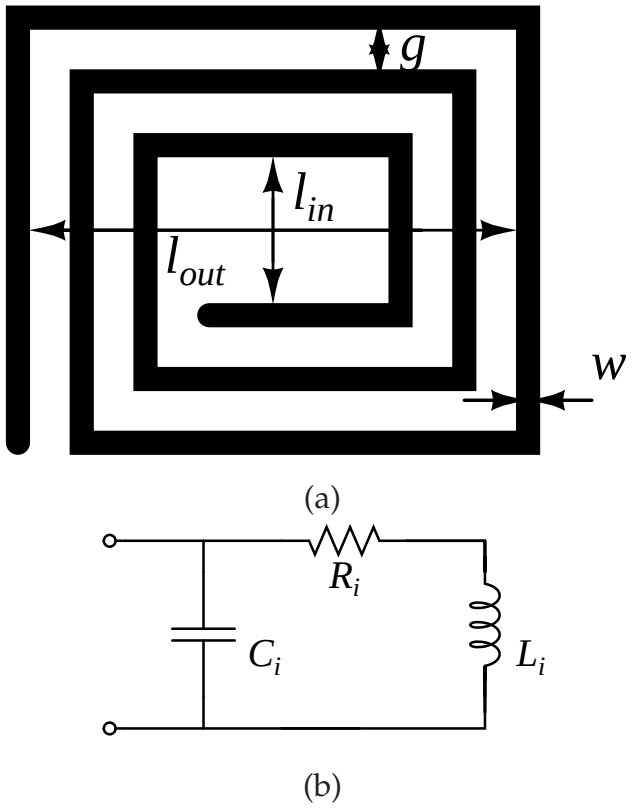

Figure 5.5. Square spiral configuration (a) Geometry. (b) Lumped equivalent circuit. The square spiral geometry can be represented in terms of inductance (L_i), sheet resistance (R_i), and loss capacitance (C_i).

densities, and is given by

$$L_{i2} = \frac{\mu_0 n^2 l_{avg} c_1}{2}\left[\ln\left(\frac{c_2}{æ}\right) + c_3 æ + c_4 æ^2\right]. \tag{5.8}$$

Here, c_i (i = 1 to 4) are shape-dependent coefficients, and are presented in Table 5.4. Finally, the third expression for inductance is a data fitted monomial equation and is given by

$$L_{i3} = \Psi(l_{out})^{m_1}(w)^{m_2}(l_{avg})^{m_3}(n)^{m_4}(g)^{m_5}. \tag{5.9}$$

Where m_i (i = 1 to 4) and Ψ are the layout-dependent coefficients outlined in Table 5.4.

The sheet resistance R_i heavily influences the conductor loss of the coil. The sheet resistance for a conductor strip of thickness t is given by

$$R_i = \frac{l_{tot}}{W\delta\sigma\left(1 - e^{-\frac{t}{\delta_c}}\right)}. \tag{5.10}$$

Table 5.4. Coefficients for inductance expressions

Square spiral inductor		
Modified Wheeler expression	K_1	2.34
	K_2	2.75
Current sheet approximation	c_1	1.27
	c_2	2.07
	c_3	0.18
	c_4	0.13
Data-Fitting monomial expression	Ψ	1.62×10^{-3}
	m_1	-1.21
	m_2	-0.147
	m_3	2.40
	m_4	1.78
	m_5	-0.030

Here $l_{tot} = 4\,n\,l_{avg}$ is the total length of the conductor strip in the coil, W is the width of the strip, and δ_c is the skin depth given by

$$\delta_c = \sqrt{\frac{2}{\omega \mu_c \sigma_c}}, \tag{5.11}$$

where μ_c and σ_c are the magnetic permeability and conductivity of the strip metal conductor, respectively. Finally, the term C_i in Fig. 5.5(b) represents the capacitance loss associated with the penetration of the electric field into the lossy piezoelectric substrate, and is given by (Hall and Hao 2006)

$$C_i = \frac{\epsilon_0 \epsilon_{rs} n W^2}{t_s}. \tag{5.12}$$

Here t_s and ϵ_{rs} are the thickness and relative permittivity of the piezoelectric substrate, respectively.

The receiver coil comprises of a 6×6 mm, 12-turn square spiral, 3 μm thick gold coil manufactured on a 128° YX $LiNbO_3$ piezoelectric substrate of thickness $t_s = 0.5$ mm, as shown in the Fig 5.6. The choice of the conductor material and thickness was guided by the aim to increase the quality factor of the coil through the use of low-resistive material such as gold. The line width of the coil is $W = 100$ μm and the spacing between the turns is $g = 50$ μm. The number of turns and the spacing between the turns was chosen to increase the self-inductance, and the inner diameter of the coil to limit the eddy currents.

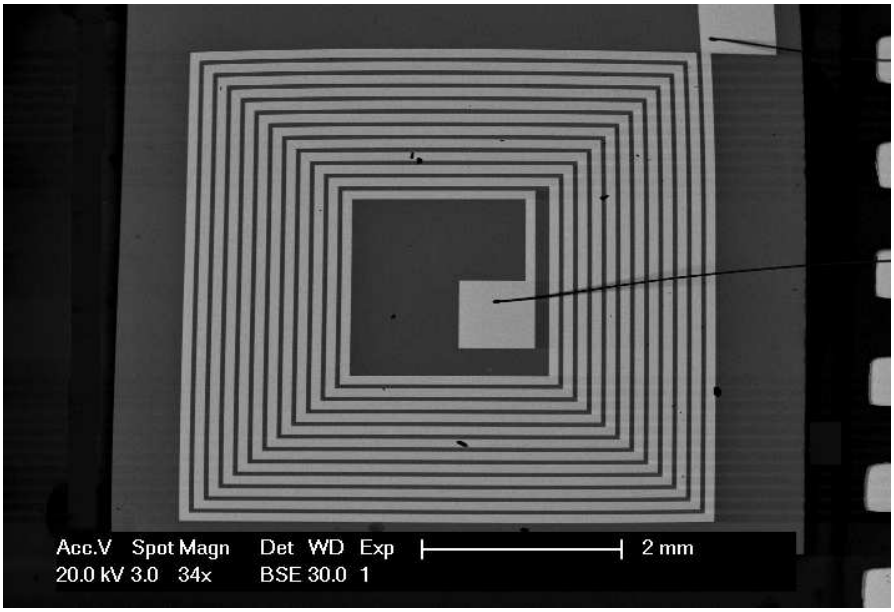

Figure 5.6. SEM photograph of a 12-turn square spiral coil/antenna on a 128° YX $LiNbO_3$ wafer.

Fabrication

The implant square spiral coil fabrication on a 3" 128° YX $LiNbO_3$ circular wafer is undertaken in this work using the same optical lithographic process employed for SAW device fabrication, outlined in Section 3.5. As the coil thickness is three times higher than the IDT thickness of the SAW devices, the gold layer deposition was carried out in three stages. Here, each stage comprised of a gold layer deposition of 1 μm and a 15 minute cooling off period in between stages. In the same way, the sputter etching of the gold, not covered by the photoresist, was performed by ion bombardment in three stages with a 15 minute cooling off period. The wafer is then sawed into square dies of 7.5 $\times$ 7.5 mm such that each die consists of one spiral coil and is conformal with the SAW correlator die size. The dies are then placed in the DIL carrier with dimensions of 38.5 $\times$ 38.8 mm and 54 pins, as shown in Fig 5.7. The pads of the coils are wire bonded to the pins of the package using a 25 μm diameter gold wire.

5.4.2 Handheld Coil/Antenna

As the transmitter coil is placed outside the body, there are fewer restrictions placed on its size and substrate material. However, an optimal handheld coil needs to address the issues of robustness, omnidirectional radiation pattern through small quality factor, and impedance matching with the implant coil for maximum power transfer. The

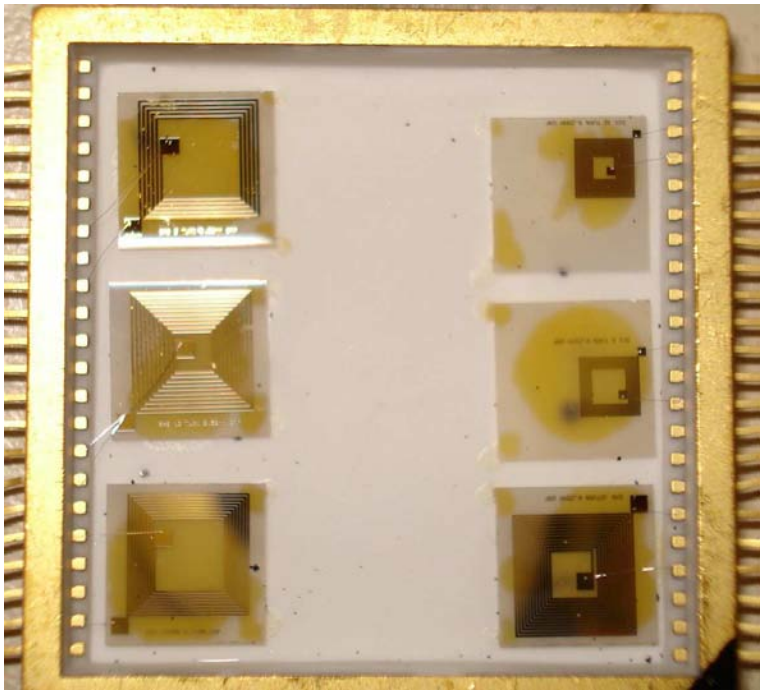

Figure 5.7. The fabricated miniature coils mounted on a 54 pin DIL carrier.

efficiency of the inductive link is determined by the mutual inductance between the coils, which in turn is a function of the self inductances of the individual coils. It was demonstrated by Arfin (2006) that for a system constrained to a fixed, small receiver coil the magnetic flux linkage between the coils would improve if the radius of the transmitter coil is close to the separating distance, which for the current application is considered to be 5 cm. However, as a result of the practical size constraint imposed on the transmitter coil, a 3-turn spiral pattern with an outer dimension of 8×5 cm ($l \times w$) was chosen. Copper, with a thickness of 20 μm, was used to model the coil on a FR-4 substrate with a relative permittivity of 4.7, as shown in the Fig. 5.8. Both the line width of the coil and the spacing between the turns was set to 1.5 mm. The expressions for inductance, sheet resistance and loss capacitance given in Eqns. (5.7) - (5.12) are also applicable to the handheld antenna.

5.4.3 Coupling in the Presence of Human Body Phantom

A complete equivalent circuit of the inductive link coupling the handheld and implant coils for spiral geometries is depicted in Fig. 5.9. The primary circuit/handheld controller comprises of an AC voltage source connected to a transmitter coil to deliver power to the implanted coil. The elements R_h, L_h represent the sheet resistance and

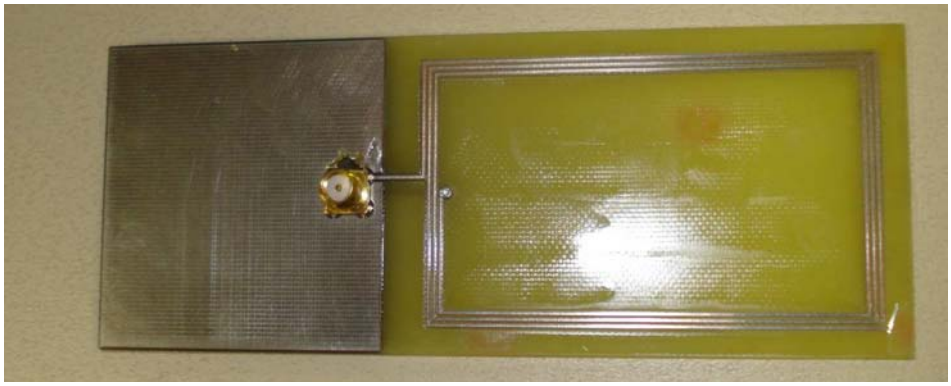

Figure 5.8. Snapshot of a 3-turn spiral handheld coil/antenna on a FR-4 substrate.

inductance of the handheld coil, respectively. The loss capacitance of the had-held coil, due to substrate coupling, is assumed to be negligible because of the high resistivity of the FR-4 substrate. Moreover, this assists in simplifying the equivalent circuit analysis. The capacitors C_1 and C_2 are the tuning capacitors employed to maximise the power transfer by matching the impedances of both the coils.

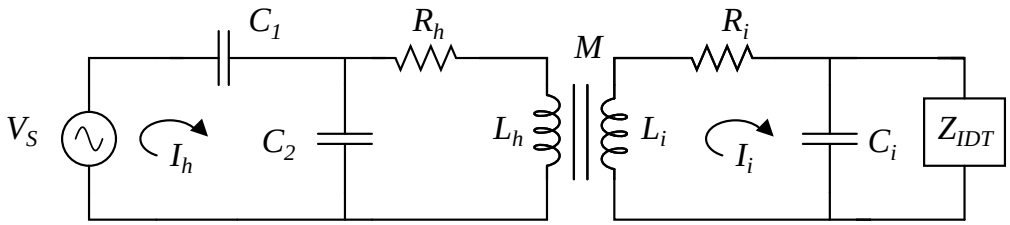

Figure 5.9. Equivalent circuit of the inductive link with spirals for both handheld and implant coils. The tuning capacitors C_1 and C_2 are employed to maximise the power transfer.

The admittance (Y_i) of the implanted coil when connected to a SAW correlator with an input impedance of Z_{IDT} (Eqn. (5.1)) is given by

$$Y_i = Z_{IDT} + j\omega C_i + \frac{1}{R_i + j\omega L_i}, \tag{5.13}$$

which can be rewritten as

$$Y_i = Z_{IDT} + \frac{R_i}{R_i^2 + \omega^2 L_i^2} + j\left(\omega C_i - \frac{\omega L_i}{R_i^2 + \omega^2 L_i^2}\right). \tag{5.14}$$

Similarly, the admittance of the handheld coil is by

$$Y_h = j\omega C_2 + \frac{1}{R_h + j\left(\omega L_h - \frac{1}{\omega C_1}\right)}, \tag{5.15}$$

which can be solved for conductance and susceptance as

$$Y_h = \frac{R_h}{R_h^2 + \left(\omega L_h - \frac{1}{\omega C_1}\right)^2} + j\left[\omega C_2 - \frac{\left(\omega L_h - \frac{1}{\omega C_1}\right)}{R_h^2 + \left(\omega L_h - \frac{1}{\omega C_1}\right)^2}\right]. \tag{5.16}$$

The mutual inductance M associated with the coils is given by

$$M = k\sqrt{L_h L_i}. \tag{5.17}$$

Here, k is the coupling coefficient depending on several factors such as operating medium, coil material and geometry, and operating frequency and distance. The induced current (I_i) and voltage (V_i) in the implant coil can be derived from the expression

$$V_s = \frac{I_h}{Y_h} - j\omega M I_i, \tag{5.18}$$

such that

$$I_i = \frac{1}{j\omega M}\left(\frac{I_h}{Y_h} - V_s\right), \tag{5.19}$$

and

$$V_i = \frac{I_i}{Y_i} = j\omega M I_h. \tag{5.20}$$

To find the optimal values of the tuning capacitors C_1 and C_2 for maximum power transfer, the handheld coil is excited at resonant frequency f_0. Thus, C_1 can be solved by equating the conductance of the handheld coil in Eqn. (5.16) to the admittance of the implant coil in Eqn. (5.14), such that

$$\frac{R_h}{R_h^2 + \left(\omega_0 L_h - \frac{1}{\omega_0 C_1}\right)^2} = Y_i. \tag{5.21}$$

The capacitance C_2 can be obtained by setting the susceptance of the handheld coil in Eqn. (5.16) to zero, such that

$$C_2 = \frac{\left(L_h - \frac{1}{\omega_0^2 C_1}\right)}{R_h^2 + \left(\omega_0 L_h - \frac{1}{\omega_0 C_1}\right)^2}. \tag{5.22}$$

As can be observed from the above analytical analysis, the accurate determination of the coupling coefficient k is crucial to ensure a realistic modelling of the body-centric communication system. This can be achieved by the application of the boundary conditions in FEM, which are discretized to a very low level of abstraction. Hence, to

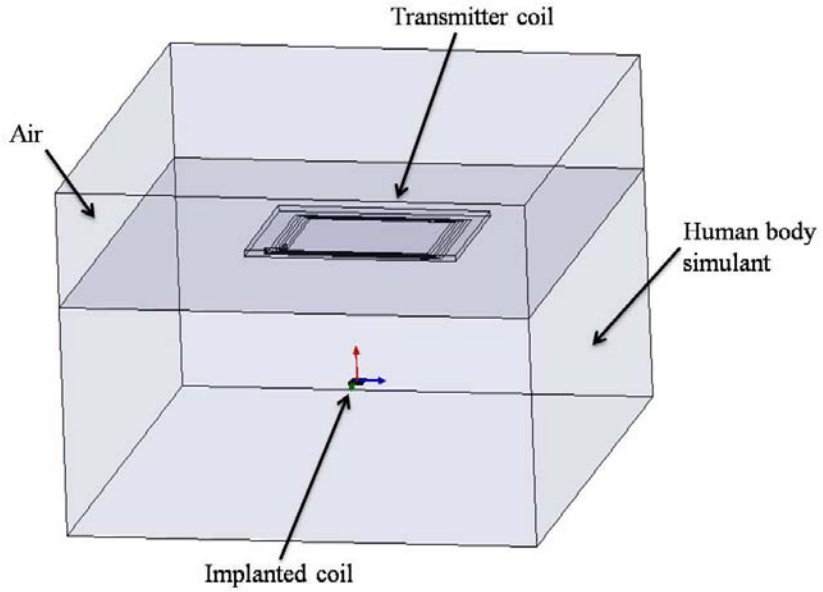

Figure 5.10. Simulation setup for the design of the inductive coupled telemetry system. The implant coil is encapsulated in a numerical human body phantom, where as the transmitter coil is surrounded by air medium.

capture the dynamic behavior of the implant and to account for the strong attenuation and multiple reflections of the electromagnetic waves in a biological environment the implanted coil is surrounded, and separated from the transmitter coil, by a human body simulant. The best practice to represent the average body properties, in numerical modelling, is to consider the electrical properties of the the human body simulant as $2/3^{rd}$ those of pure muscle (Soontornpipit *et al.* 2004, Izdebski *et al.* 2009). The dielectric properties of the human muscle for a wide range of frequencies are given in Table 5.2. As the operating frequency range of the implanted microvalve is between 10-100 MHz the dielectric properties of the muscle tissue are averaged over that range and the $2/3^{rd}$ of those values are used in the FEM model. The implant antenna is placed in a $16\times16\times80$ cm block with a permittivity of 70 and a conductivity of 0.496 S/m, as shown in the inductive link FEM model in Fig. 5.10. The outer surface of the handheld coil is enclosed by a block representing air. On the other hand, the measurements are carried out by employing a wet physical phantom, as described in Section 5.2, with dimensions identical to the numerical phantom. The simulation and measurement results of this inductive link, where the separation between the coils is 5 cm, are presented in the next section.

5.5 Results and Discussion

The 3-dimensional FEM simulations and experimental measurements of the body-centric communication system, the results of which are discussed in this section, are driven by the goal to optimise and validate the contactless powering transmission mechanism, between the handheld controller and the implanted microvalve, in the context of the operating environment. This was carried out by analysing the frequency dependent behaviour of the effective inductance, quality factor of the individual coils, and the S_{12} coupling response of the complete telemetry system.

5.5.1 Quality Factor and Effective Inductance

The main objective of this chapter is to model an inductive telemetry link with high coupling efficiency, that can power a miniature wireless microvalve in a secure manner, through the optimisation of design parameters. In the current system, due to the separation between coils, only a percentage of the energy transmitted by the handheld coil is received by the implant. This received energy is further attenuated in the implant due to the sheet resistance of the coil, and the rest is stored as electromagnetic energy in the self-inductance and capacitance of the coil. Hence, the two important design parameters that influence the power transfer capabilities of such a link are the quality factor and effective inductance of the coils. The quality factor (Q) is the ratio of the magnetic energy stored to the power dissipated and the effective inductance (L_{eff}) of the inductor along with the associated parasitic capacitance (Bahl 2003), is given by

$$Q = -\frac{\text{Im}(Y_{11})}{\text{Re}(Y_{11})}, \tag{5.23}$$

$$L_{\text{eff}} = -\frac{1}{\omega \text{Im}(Y_{11})}, \tag{5.24}$$

where Y_{11} is the short-circuit input admittance of the coils.

To improve the mutual coupling, it is desirable to have a high value of inductance for the two coils. Furthermore, the quality factor of the implanted coil should be high, to minimise the RF power losses, and the transmitter coil should be low, to compensate for the misalignment of coils.

The simulated and measured effective inductance and quality factor of the implanted coil was computed from the admittance using the Eqns. (5.23) and (5.24), as shown in the Fig. 5.11. The S-parameter, and subsequently the Y-parameter, measurements were

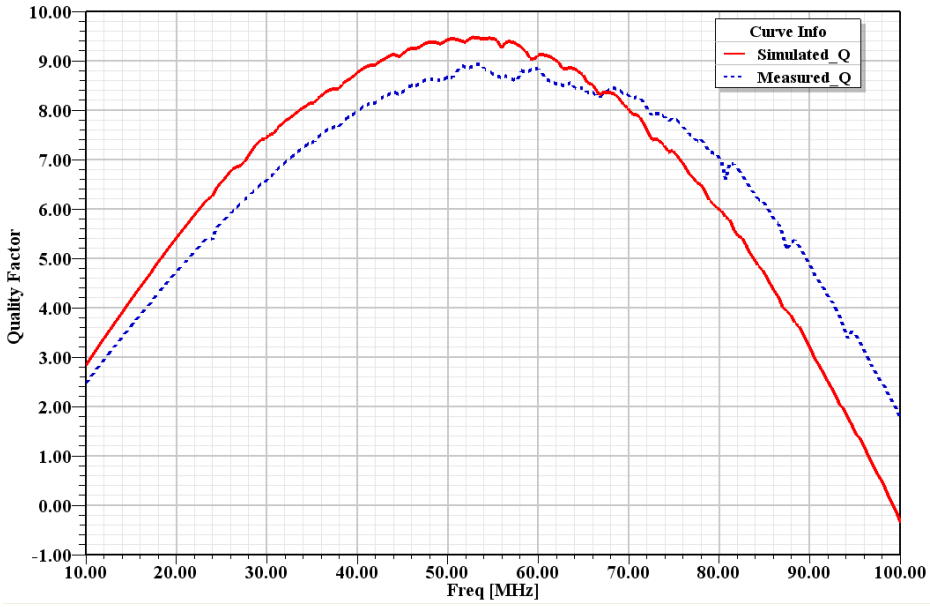

(a)

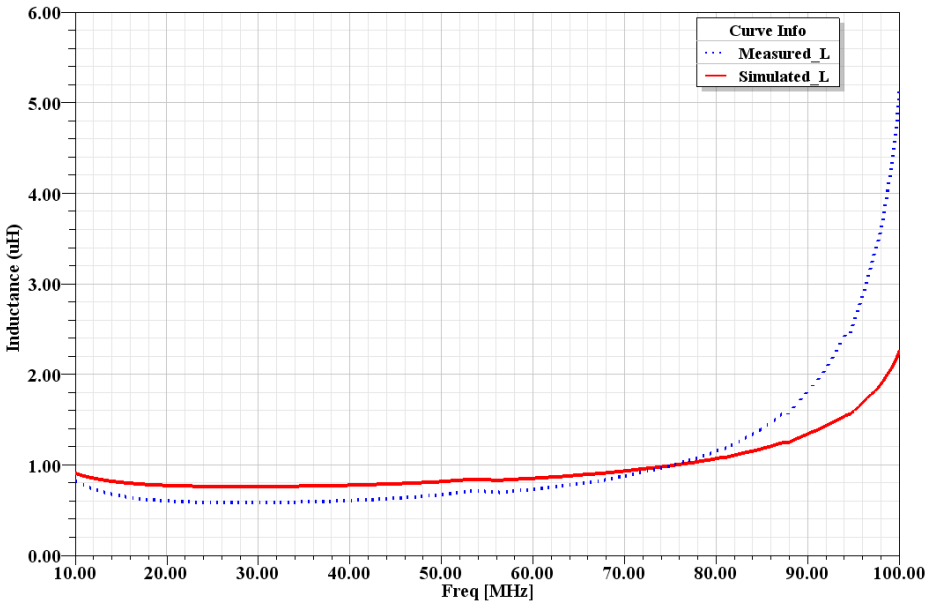

(b)

Figure 5.11. Implanted coil's (a) Quality factor (Q) and (b) inductance (L_{eff}). The maximum values of Q obtained from the simulation and measurement were 9.4 and 8.9, respectively. The simulated and measured inductance was in the vicinity of 0.8 μH and 0.7 μH, respectively, before it approaches self-resonance.

performed using a 2-port Agilent N5230A network analyzer. Between 30−90 MHz which is the operating frequency range of interest from a SAW correlator point of view, the maximum values obtained through simulation and through measurement of the receiver coil Q factor were 9.4 and 8.9, respectively.

The simulated and measured effective inductance were in the vicinity of 0.8 μH and 0.7 μH, respectively. Above the frequency of interest, the inductance value starts to raise due to proximity to the self-resonant frequency of the implanted coil. The differences in the simulation and experimental results can be attributed to the secondary parasitics associated with the packaging pads and wires. To analyse the inductive properties of the handheld coil, the measured reflection coefficient (S_{11}) is depicted in the Fig. 5.12. It was observed that the handheld coil's self-resonant frequency occurs at 60 MHz. This frequency could, however, be adjusted in accordance with the requirements of the microvalve operating frequency by varying the tuning capacitors C_1 and C_2 (Eqn. (5.21)−(5.22)).

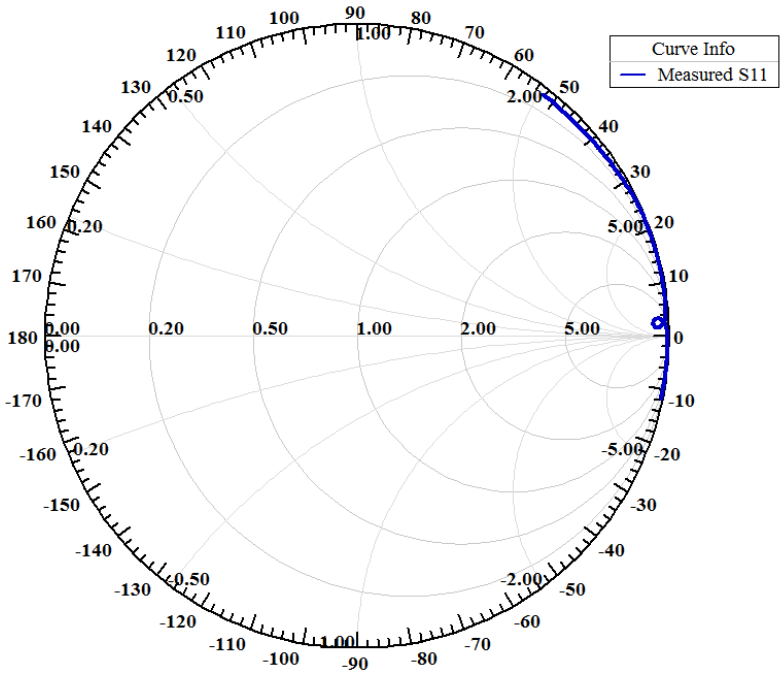

Figure 5.12. Measured S_{11} of the handheld coil with a self-resonant frequency of 60 MHz.

5.5.2 Received Relative Signal Strength

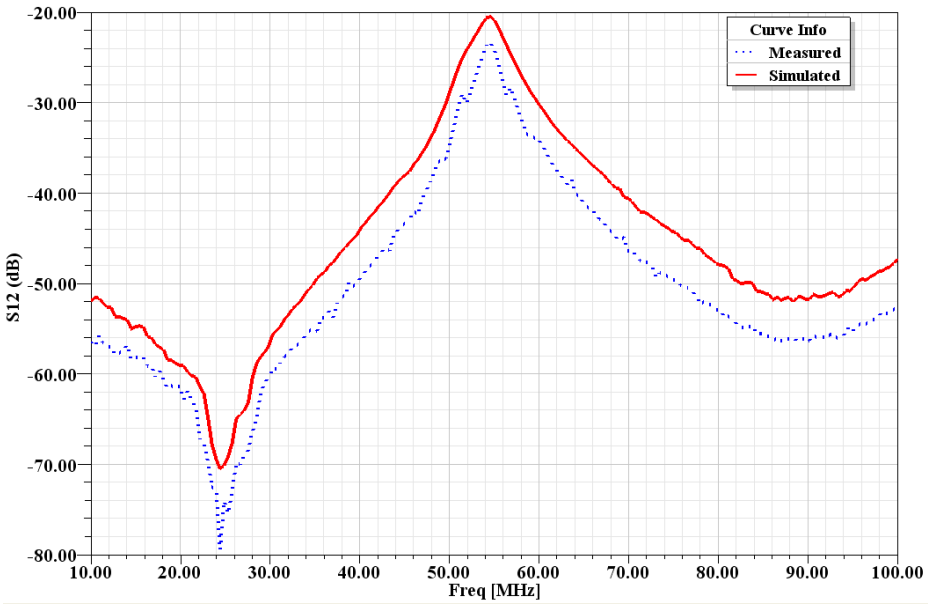

(a)

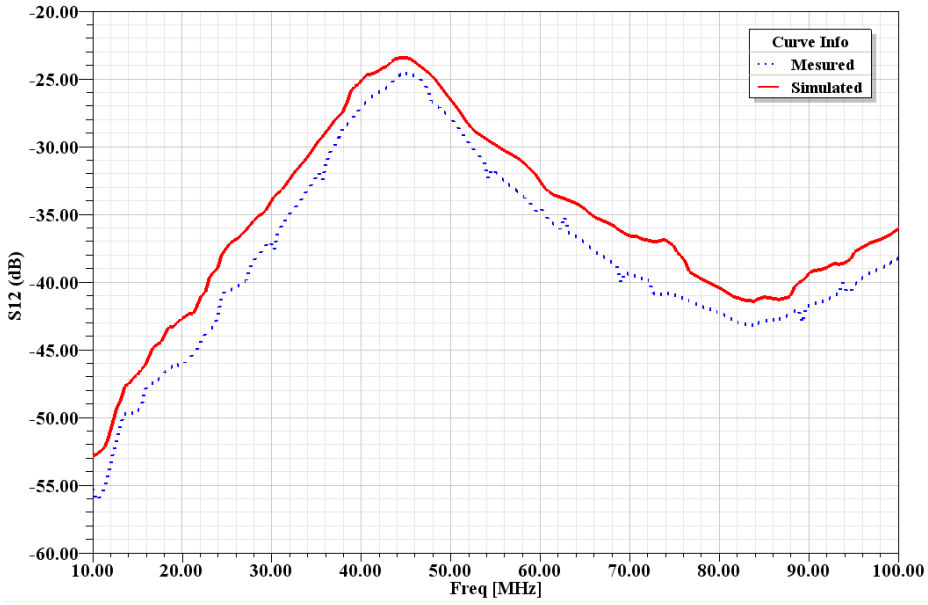

(b)

Figure 5.13. Simulated and measured coupling (S_{12}) between the implanted and transmitter coil separated by a distance of 5 cm by (a) air. (b) a human body phantom. There is a drop of 2.6 dB in measured signal strength and 9 MHz drop in the measured frequency of maximum power transfer for the instance when the medium is human body phantom when compared to air.

In this subsection, the emphasis is on the energy received by the implanted coil in the presence of air and human body phantoms. Depending on the type of inductive link, various methodologies can be used to analyse the coupling between the transmitter and receiver coils. The most frequently used ones are the transformer model and the mutual inductance model (Wang *et al.* 2000). The transformer model is ideal for closely coupled inductive link as the leakage inductance is ignored. Here, the ratio of the number of turns is employed to deduce the transformed voltage. On the other hand, the mutual inductance model considers both the coupling and leakage inductances and therefore is more suitable for weakly coupled inductive links. As the looses in the medium and the attenuation of the RF radiation are crucial for an accurate characterisation of the current telemetry system, so the mutual inductance model was employed. Mutual inductance provides a measure of the received signal strength of the implanted coil when the transmitter coil is excited by an alternating current. As a result of the high Q factor, a small variations in the resonant frequencies of the implanted and handheld coils would result in a large error. Hence, the implanted coil in this work was designed not to resonate in the operating frequency range of interest. This is because of the difficulties associated with calibrating a high Q device, such as the implanted coil.

Fig. 5.13 shows the simulated and measured S_{12} response, representing the received power, in the range of $10-100$ MHz, when the gap is 5 cm and the medium between the coils is one using air and another using the human body phantom. The S_{12} response is determined by the effect of the transmitter coil on the implanted coil, the intrinsic properties of the implanted coil, separation between the coils, transmitting medium and the frequency of operation. From Fig. 5.13.(a), it was observed that the maximum simulated and measured coupling of -20.2 dB and -23.4 dB, respectively, occurs at 54 MHz when air is the medium between the coils. Fig. 5.13.(b) shows the received relative signal strength when the medium between the coils is human body phantom. Due to the use of magnetic coupling there is a marginal drop, of 2.6 dB, in measured signal strength when compared to that in air medium. However, a shift in the frequency of maximum power transfer was observed at 45 MHz. This frequency shift and wide band behavior is caused by the dielectric properties of the conducting medium representing human body. The value of the induced signal strength may seem quite low but is considered normal for this type of weak coupling in the presence of human body simulants (Simons and Miranda 2006, Hall and Hao 2006). Fig. 5.14 depicts the measured S_{12} response of the system when the coils are separated by a gap of

10 cm with physical human body phantom. As is evident from the Fig. 5.14, there was a significant drop in mutual coupling response, both in terms of received signal strength (7.9 dB) and peak power operating frequency (8 MHz), compared to the instance when the separation was 5 cm in Fig. 5.13.(b).

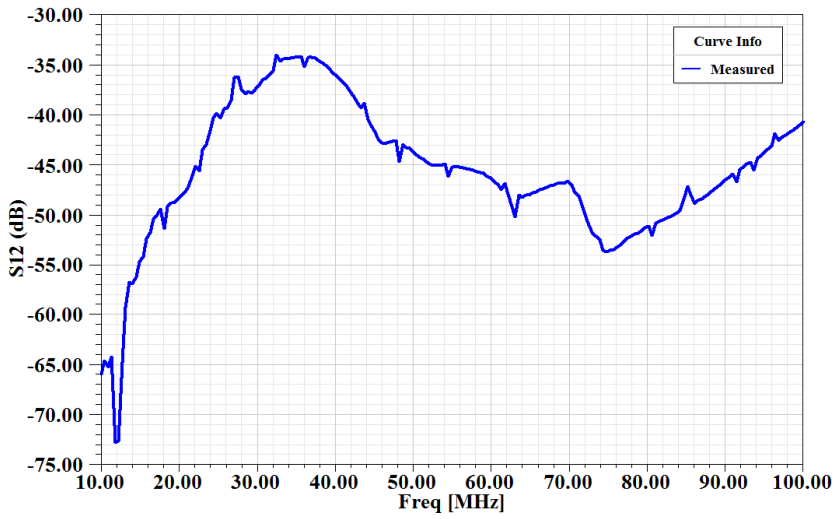

Figure 5.14. Measured S_{12} response when the distance between the implanted coil and the transmitter coil is 10 cm and the medium is human body phantom. There was a drop in received signal strength by 7.9 dB and peak power operating frequency by 8 MHz, compared to the instance when the separation was 5 cm.

The above results reflect the accuracy of the telemetry system designed for a given separation between the transmitter and the implanted antenna. Thus, the efficiency of using the FEM modelling approach for the simultaneous analysis of the transmitter and the handheld coils, and in gaining a deeper insight into the inductive link's response for various coil layouts, operating environments, and coupling conditions is established. The maximum received relative signal strength of -25 dB (Fig. 5.13.(b)) falls within the expected range for body centric implant communications (Hall and Hao 2006). Even though this results in a low diaphragm deflection in the order of few nano meters, the high frequency of operation ensures an optimal fluid flow rate for the microvalve (Kaajakari *et al.* 2001).

The effect of variable coil alignment positions on the transmitted power is outlined in the following subsection.

5.5.3 Coil Misalignment and Implant Tilting

A study of the wireless power transmission under varying coupling conditions is mandatory to accurately characterise the performance of the telemetry system. One such condition, which influences the efficiency of magnetic coupling in moving loads is the orientation of the coils. Any misalignment or tilting of coils results in a reduction in the received relative signal strength, as the rate of change of magnetic flux is directly proportional to the induced power. For the above discussed inductive link, the angle and radial distance of the implant from the handheld coil's geometric centre was varied to analyse the difference in the coupling resulting from coil misalignment. It was observed that the coupling was insensitive to coil misalignment, within the overlapping area of the coils, because of the relatively large size of the handheld coil compared to the implant. The uniformity of the generated magnetic field ensures a minimal impact of the coil misalignment on the magnetic flux linkage. Furthermore, the implanted antenna was tilted by 30^o and 60^o, and the variation in the power transfer capability was analysed. The response of the tilted inductive link is provided in the Fig. 5.15, while all other design parameters are kept the same. By comparing this response, with the signal strength response of the Fig. 5.13.(b), it was observed that there is a 3.1 dB and 5.9 dB drop in the measured peak signal strength and 2.5 MHz and 5.5 MHz drop in the corresponding operating frequency when the transmitter coil is tilted by 30^o and 60^o, respectively. Thus, the analysis of the coil tilting allows for the identification of the minimum driving power required to guarantee the operation of the microvalve. These measurements assist in testing the efficiency of the microvalve for variable operating conditions. The worst case scenario of 90^o tilting can be employed as the minimum threshold signal level to enable the actuation of the microvalve. This can be carried out by optimising other design parameters such as diaphragm length, thickness, material and type (eg: corrugated structures). On the other hand, to accurately account for the influence of the SAW correlator IDTs on the implant coil power reception capabilities, the IDTs were modelled on the bottom surface of the piezoelectric substrate in the FEM model. By comparing the simulated S_{12} response to the instance when the IDTs were neglected, it was observed that there was no significant difference.

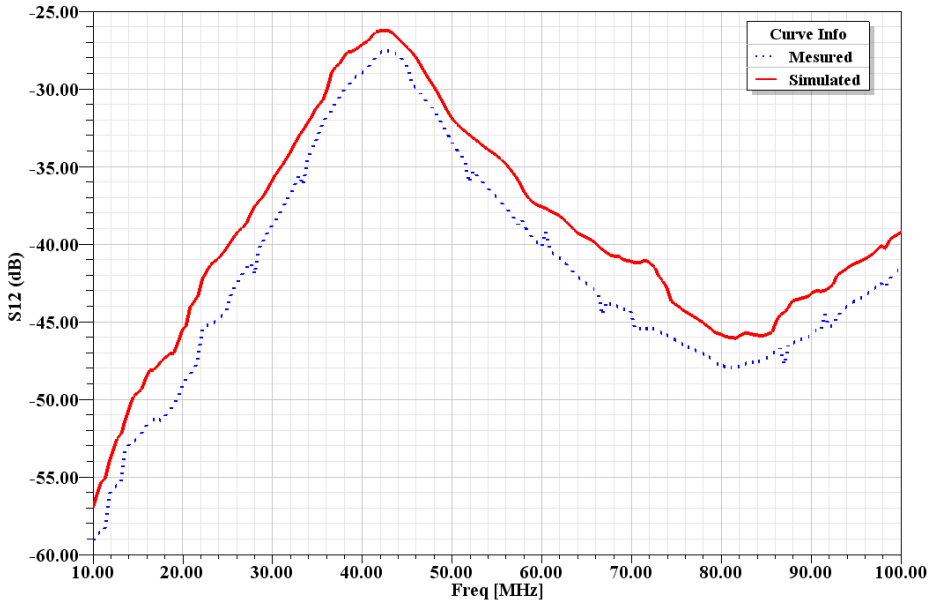

(a)

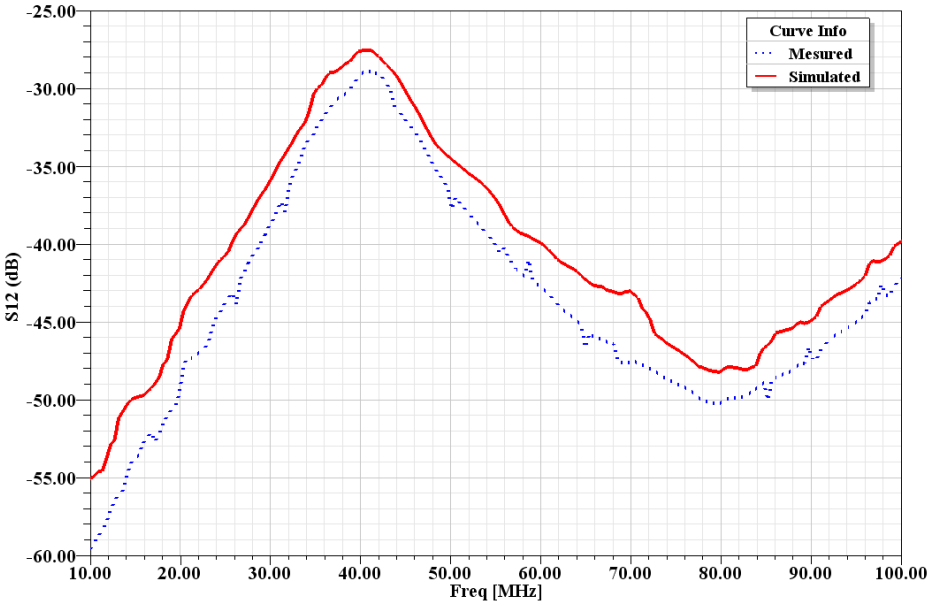

(b)

Figure 5.15. Simulated and measured S_{12} coupling when the distance between the coils is 5 cm and the transmitter coil is tilted by (a) 30^o. (b) 60^o. There was a drop of 3.1 dB and 5.9 dB in the measured peak signal strength and 2.5 MHz and 5.5 MHz in the operating frequency when the transmitter coil is tilted by 30^o and 60^o, respectively.

5.6 Conclusion

The development of novel and innovative biomedical devices, such as the wireless powered microvalve, would drive the next generation of implants. This implies that the power is at a premium in the implants and hence necessitates the design and development of a contactless powering system specific to the implant functionality. This chapter, using FEM modelling and experimental characterisation, addressed the issues of the microvalve structure conformal, implanted antenna miniaturisation on a piezoelectric substrate. Furthermore, the near-field coupling between the handheld controller and a wireless microvalve in the presence of a human body phantom was investigated. The results discussed in this work include: (i) Comprehensive 3-dimensional FEM modelling and physical validation of an inductively coupled link comprising a $6\times6\times0.5$ mm conformal spiral implanted antenna and a $8\times5\times0.2$ cm spiral transmitter antenna separated by a human body phantom (ii) analysis of the quality factor and inductance of individual coils (iii) observation of the received relative signal response of the implanted antenna (iv) analysis of the difference in induced power when there is coil misalignment and tilting. Hence, FEM modelling provides an effective way of gaining a deeper understanding of the inductive link response for various coupling conditions and ultimately in the full optimisation and experimental validation of the telemetry system for an implantable microvalve.

Chapter 6

Conclusion

With the ever increasing demand to access better health care and diagnosis facilities, both in the developed and developing countries, there is a unrelenting quest by the research community to address existing bottlenecks with emerging technologies. These innovations are aimed at either targeting novel applications or optimising the performance of existing designs. Being at the core of many scientific advances for the past few decades, miniaturisation has caused a minor shift in focus from electrical properties of silicon in semiconductor industry to electromechanical properties of micromachined structures in MEMS. Moreover, the evolution of MEMS compatible technologies such as sensor and actuators, wireless communications, electrochemical batteries, energy harvesting, and nano and biocompatible materials have paved the way for the development of novel and diverse biomedical implants. Even though, the clinical deployment of such implants is a time taking process, bound by several regulations and approvals, this hasn't dampened the spirits of researchers due to the sheer depth of market penetration these devices can attain, once commercialised. However, the lifetime and remote interrogability of one type of an implant, specifically used for drug delivery applications, have been an issue of contention, limited by the battery life and the device size. These shortcomings were addressed in this research by employing a SAW correlator to design a novel RF powered, secure coded, active microvalve with fully passive components. The deployment of such a device in a subject's body has the potential to revolutionise health care for long-term, controlled drug release applications such as insulin delivery for diabetes management and therapy for cancer treatment.

The multi-field nature of project and the expensive microfluidic fabrication process necessitated a comprehensive modelling approach for the critical investigation and refinement of the individual microvalve components. Through out the course of the thesis, a thorough review of existing modelling techniques for SAW devices, MEMS components, and biotelemetry systems was provided to reveal the prevalence of simplifying assumptions and approximations. Hence, a comprehensive finite element modelling approach, where the complete set of partial differential equations are solved, was employed both to design complex structures with low level of abstraction and to automatically include the majority of the second order effects. Furthermore, the availability of software packages with large node handling capabilities and relaxation of constraints on computing and memory resources, with each passing day, have complemented the viability of using FEM modelling approach for various stages of the project. The results of each stage are briefly outlined in the next section to draw up the conclusion for the thesis.

6.1 Summary

The thesis summarised the research towards a novel SAW correlator based RF powered, secure coded, active microvalve with fully passive components. Optimisation and verification of individual components of the microvalve was undertaken in order to estimate the performance of the integrated assembled system. This was carried out by taking a comprehensive design, modelling, optimisation and experimental validation approach for the majority of the research outcomes in the thesis. The results of the research presented in the preceding chapters are highlighted here to draw conclusions on the feasibility of such a microvalve. These results are a confirmation of the specific research contributions outlined in Chapter 1.

SAW Parameter Extraction Using FEM

The versatility, reliability, ease of modelling complex geometries, and automatic inclusion of second order effects, offered by finite element analysis have made it an optimal approach for modelling SAW devices. After a thorough review of existing parameter extraction techniques in Chapter 2, the extraction of the complete set of COM/P-matrix parameters from the FEM modelling for an infinitely long, synchronous, one-port resonator was demonstrated. Based on this modelling, a filter structure using 128° YX

$LiNbO_3$ piezoelectric substrate and Au electrode gratings was modelled by considering the complete set of partial differential equations governing the electro-mechanical properties, with and without excitation, it was possible to analyse the freely propagating eigenmodes, eigenvalues, electrically active waves and electrical admittance. The COM/P-matrix parameters were extracted from the simulation results using a curve fitting technique. Furthermore, experimental validation of these parameters was considered by fabricating a delayline filter with the same periodic dimensions and materials as that of the FEM modelled infinite periodic grating. The simulated frequency response of the delayline, designed using P-matrix model from the extracted parameters, was found to be in good agrement with the measured delayline filter response. Based on the presented direct FEM modelling approach, the extraction of SAW and LSAW parameters is demonstrated in a more rigorous, direct and realistic manner than any of the simulation techniques currently available. Furthermore, the developed versatile technique can be extended to layered SAW devices and other constantly evolving acoustic wave devices with novel repetitive electrode geometries.

SAW Correlator FEM Modelling

Contrary to the frequently used equivalent circuit or phenomenological SAW correlator modelling techniques outlined in the literature, where only an abstract insight into the analysis of selective designs aspects of the device is possible, a novel full scale FEM modelling approach was developed and presented in Chapter 3. Based on the developed modelling, the requirements placed by the current and emerging wireless interrogation applications on these devices such as low insertion loss and high selectivity can be taken into consideration and analysed in the frequency and time domain. This is demonstrated through a comprehensive FEM modelling of 2 and 3-dimensional, 5×2-bit Barker sequence encoded SAW correlator. The FEM results were validated by fabricating SAW correlators, using photolithographic techniques. The detailed study of the admittance, harmonic, transient responses of the correlator with a coded Au electrode gratings on 128° YX $LiNbO_3$ piezoelectric substrate, effect of the shear horizontal wave component, difference in electrical response when there is a code mismatch, and experimental validation of the simulation results with physical measurements were presented in that chapter. As the applicability of this method is not restricted by the design complexities or the material properties or the loading conditions, it provided an efficient way for gaining a deeper understanding of the correlator's response and ultimately in the optimisation of correlator design before indulging into expensive and

time consuming test structures fabrication. Backed by the experimental validation of developed SAW correlator FEM model, its application to the design and optimisation of a wireless powered microvalve was then discussed in the Chapter 4.

RF-Powered Microvalve

The Chapter 4 demonstrated the design and simulation of a novel wireless active microvalve by taking into account both the electroacoustic correlation and electrostatic actuation in a single finite element model. The novel implant specifications such as small size, passivity, and remote interrogability of the microvalve were imbibed in the novel FEM model. Based on the developed FEM formulation of 3-dimensional, 5×2-bit Barker sequence SAW correlator driven microchannel, and the results presented in that chapter, a thorough investigation of the multiple coupled physics phenomena at the process level was undertaken, before fabrication. A detailed study of the harmonic and transient microchannel deflection caused by electrostatically coupling the output IDT's of the SAW correlators to the microchannel and analysis of the difference in microchannel deflection when there is a code match and a code mismatch was illustrated. Furthermore, the dynamic response of the low leakage microvalve including the microchannel opening and closing movement, the driving energy, and the actuation time were presented. It was demonstrated that the model appropriately represented the interrogating signal code dependent, and the excited acoustic mode dependent operation of the microvalve and hence enabled a comprehensive analysis of the microchannel deflection. In consideration of such deflection analysis of the developed microvalve FEM model, a wireless telemetry system for the microvalve was presented in Chapter 5.

Wireless Telemetry System for the Implanted Microvalve

As the power is at a premium in a wireless powered microvalve, it necessitated the design and development of a contactless powering system specific to implant functionality. Chapter 5 presented a custom design and development of the telemetry system for the implanted microvalve, using FEM modelling and experimental characterisation, by taking into account the aspects of small device dimensions, surrounding environment (human body), piezoelectric substrate material, and electrical and mechanical conformity with the structure. The near-field coupling between the hand-held controller and a wireless microvalve was investigated in the presence of numerical and physical human body phantoms. A comprehensive 3-dimensional FEM modelling and physical validation of an inductively coupled link comprising a $6\times6\times0.5$ mm conformal spiral

implanted antenna and a $8\times5\times0.2$ cm spiral transmitter antenna, separated by a human body phantom, was demonstrated. In addition to the investigation of the quality factor and inductance of individual coils, an analysis of the received relative signal response of the implanted antenna was presented. Furthermore, a study of difference in induced power when there is coil misalignment and tilting was illustrated. Thus, the efficiency of using the FEM modelling approach for the simultaneous analysis of the transmitter and the handheld coils in gaining a deeper insight into the inductive link's response for various coil layouts, operating environments, and coupling conditions was established and demonstrated. As a result, it has facilitated the full scale optimisation and experimental validation of the telemetry system for an implantable microvalve.

6.2 Future Perspective

Finally, the future directions for the research presented in the thesis are outlined in this section. These suggestions are made in the same order as the research topics of the partially modular chapters of the thesis, which are all bounded together by the common use of FEM modelling approach.

To take full advantage of the demonstrated COM/P-matrix parameter extraction technique using FEM, it can be applied, with minimal modifications, to structures where the predominant propagation modes are as diverse as leaky surface acoustic wave (LSAW), longitudinal leaky surface acoustic wave (LLSAW), and surface transverse wave (STW). Furthermore, the same technique can be extended to the characterisation of the constantly evolving periodic acoustic structures with novel layered architectures, geometries, and electrode and piezoelectric substrate materials.

Though a 2-dimensional and a small aperture 3-dimensional SAW correlator FEM models were sufficient for the comprehensive evaluation of the SAW correlator's reponse, due to negligible shear particle displacement, it is envisaged that, with the advent of high bit computing and improving memory technology, it is a matter of time before a full scale modelling of acoustic correlator with actual aperture and even long codes is modelled to account for beam steering, busbar diffraction, and other predominant acoustic modes.

The challenging requirements placed on the novel microvalve such as wireless interrogability, secure actuation, low leakage and passivity, were addressed through the

design and expansive simulation of a structure that combines electroacoustic correlation and electrostatic actuation in a synergetic manner. The interrogating signal code dependent, and the excited acoustic mode dependent deflection analysis of the microvalve served as a convincing verification of the proposed technique. Even though the secure centre deflection of a diaphragm, placed above the output IDT of a single SAW correlator, was experimentally observed during the preliminary testing, the next step would be to integrate a microchannel with two SAW correlators and to perform device packaging with biocompatible coating (Dissanayake *et al.* 2009). On the simulation side, the microchannel centre deflection needs further analysis in the presence of a liquid to account for fluid damping and to estimate the fluid flow rate. This can be carried out using electrostatic-structural-fluid multi-field interactive analysis in FEM.

The designed and developed microvalve specific biotelemetry system served as a means to securely power the implanted device. However, the aspect of bi-direction communication where the response signal from the microvalve which is retransmitted back to the handheld controller, for interrogation, was not undertaken in the current research and can be considered as future work. Lastly, the developed miniature antenna needs to be integrated with the SAW correlator and the microchannel to perform a holistic experimental analysis of the microvalve deflection.

Appendix A

Appendix

Material Properties of 128° YX $LiNbO_3$ (Auld 1990 (2^{nd} Edition))

NOTE:
This appendix is included on pages 143-144 of the print copy of the thesis held in the University of Adelaide Library.

Bibliography

ABRAMOV-Y. (2005). Super-wideband high bit-rate SAW correlator, *Proc. of IEEE Ultrasonics Symposium*, Vol. 4, pp. 2206–2209. 3.2.2

AHMADIAN-M., FLYNN-B., MURRAY-A., AND CUMMING-D. (2003). Miniature transmitter for implantable micro systems, *Proc. of 25th Annual International Conference of the Engineering in Medicine and Biology Society*, Vol. 4, pp. 3028–3031. 5.2

AHMADIAN-M., FLYNN-B., MURRAY-A., AND CUMMING-D. (2005). Data transmission for implantable microsystems using magnetic coupling, *Proc. of IEE Communications*, Vol. 152, pp. 247–250. 5.3

AMER-S., AND BADAWY-W. (2005). An integrated platform for bio-analysis and drug delivery, *Current Pharmaceutical Biotechnology*, **6**(1), pp. 57–64. 1.2, 5.1

ANS (2008). *ANSYS 9.0 Training Manual*. 3.3.3, 4.3.3, 4.3.3

ARFIN-S. (2006). *A Miniature, Implantable Wireless Neural Simulation System*, Master's thesis, Massachusetts Institute of Technology. Ch. 2 and 3. 5.4.2

ARTHUR-J. (1996). Modern SAW-based pulse compression systems for radar applications, *Electronics and Communication Engineering Journal*, **8**(2), pp. 57–78. 3.1

ATASHBAR-M., BAZUIN-B., AND KRISHNAMURTHY-S. (2004). Performance evaluation of SAW devices by simulation, *International journal of modelling & simulation*, **24**(4), pp. 250–262. 1.3, 3.3.2

ATASHBAR-M., BAZUIN-B., AND SIMPEH, M. KRISHNAMURTHY-S. (2005). 3D FE simulation of H_2 SAW gas sensor, *Sensors and Actuators B*. 3.3.3

AULD-B. (1990 (2^{nd} Edition)). *Acoustic Fields and Waves in Solids*, Rober E. Krieger. Appendix. 2. 2.5.1, 3.4.1, A

AVDEEV-I. (2003). *New formulation for finite element modeling electrostatically driven microelectromechanical systems*, PhD thesis, University of Pittsburgh. Ch. 3. 4.3.3

BAE-B., HAN-J., MASEL-R., AND SHANNON-M. (2007). A bidirectional electrostatic microvalve with microsecond switching performance, *Journal of Microelectromechanical Systems*, **16**(6), pp. 1461–1471. 1.2

BAHL-I. (2003). *Lumped Elements for RF and Microwave Circuits*, Artech House. Ch. 2 and 3. 5.4.1, 5.5.1

BALDI-A., LEI-M., GU-Y., SIEGEL-R., AND ZIAIE-B. (2006). A microstructured silicon membrane with entrapped hydrogels for environmentally sensitive fluid gating, *Sensors and Actuators B: Chemical*, **114**(1), pp. 9–18. 1.2

BALLANDRAS-S., AND BIGLER-E. (1998). Precise modeling of complex SAW structures using a perturbation method hybridized with a finite element analysis, *IEEE Trans. on Ultrasonics, Ferroelectrics, and Frequency Control*, **45**(3), pp. 567–573. 1.3.1, 2.1

BALLANDRAS-S., WILM-M., EDOA-P.-F., AND SOUFYANE-A. (2003). Finite-element analysis of periodic piezoelectric transducers, *Journal of Applied Physics*, **93**(1), pp. 702–711. 1.3.2, 2.4.5

BARTH-P. (1995). Silicon microvalves for gas flow control, *Proc. of Transducers 95, the 8th International Conference on Solid-State Sensors and Actuators and Eurosensors IX*, Vol. 2, pp. 276–279. 1.2

BASSET-P., KAISER-A., LEGRAND-B., COLLARD-D., AND BUCHAILLOT-L. (2007). Complete system for wireless powering and remote control of electrostatic actuators by inductive coupling, *IEEE Trans. on Mechatronics*, **12**(1), pp. 23–31. 1.3.4, 5.1

BASTERMEIJER-J., JAKOBY-B., BOSSCHE-A., AND VELLEKOOP-M. (2002). A novel readout system for microacoustic viscosity sensors, *Proc. of 2002 IEEE Ultrasonics Synposium*, Vol. 1, pp. 489–492. 4.2

BATRA-R., PORFIRI-M., AND SPINELLO-D. (2007). Review of modeling electrostatically actuated microelectromechanical systems, *Smart Materials and Structures*, **16**(6), pp. R23–R31. 1.1.1, 4.3.3

BECK-K., WOHLFAHRT-R., RUGEMER-A., REISS-S., VON SCHICKFUS-I., AND HUNKLINGER-S. (1998). Inductively coupled surface acoustic wave device for sensor application, *IEEE Trans. on Ultrasonics, Ferroelectrics, and Frequency Control*, **45**(5), pp. 1140–1144. 5.2.1

BOSCH-D., HEIMHOFER-B., MUCK-G., SEIDEL-H., THUMSER-U., AND WELSER-W. (1993). A silicon microvalve with combined electromagnetic/electrostatic actuation, *Sensors and Actuators A: Physical*, **37-38**, pp. 684 – 692. 1.1.1

BRACATO-R. (2004). *Passive Microwave Tags*, Sandia National Laboratories, Available: http://www.sandia.gov/mstc/documents/saw2.pdf. Last accessed: October, 2006. 3.2.2

BROCATO-R. (2004). *Programmable SAW Development*, Sandia National Laboratories, http://www.sandia.gov/mstc /products/usystemsprod/rfandoptosystems/saw.html. Last accessed: Nov, 2007. 1.3.2, 3.1, 3.2, 3.2, 3.3, 3.3.1, 3.3.1, 3.3.2, 3.5

BROCATO-R., HELLER-E., ONIDAHL-G., WENDT-J., JONES-S., AND PALMER-D. (2003). High frequency SAW correlator module, *Proc. of 53rd Electronic Components and Technology Conference*, pp. 458–463. 1.1.2, 3.2

BUCHNER-M., RUILE-W., DIETZ-A., AND DILL-R. (1991). FEM analysis of the reflection coefficient of SAWs in an infinite periodic array, *Proc. of IEEE Ultrasonics Symposium*, pp. 371–375. 2.4.5

BUDINGER-T. (2003). Biomonitoring with wireless communications, *Annual Review of Biomedical Engineering*, **5**(1), pp. 383–412. 1.3.4

CAMPBELL-C. (1998). *Surface Acoustic Wave Devices for Mobile and Wireless Communications*, Academic Press: Boston. Ch. 4. 1.1.2, 1.3.2, 3.2.1, 3.2.1, 3.3, 3.3.1, 3.3.3

CAO-L., MANTELL-S., AND POLLA-D. (2000). Implantable medical drug delivery systems using microelectromechanical systems technology, *Proc. of 1st International Conference on Microtechnologies in Medicine and Biology*, pp. 487–490. 1.1, 4.1

CHAKRABORTY-I., TANG-W., BAME-D., AND TANG-T. (2000). MEMS micro-valve for space applications, *Sensors and Actuators A: Physical*, **83**(1-3), pp. 188–193. 1.1

CHANGLIANG-X., AND MENGLI-W. (2005). Stability analysis of the rotor of ultrasonic motor driving fluid directly, *Ultrasonics*, **43**(7), pp. 596–601. 4.2.1

COOK-CHENNAULT-K., THAMBI-N., AND SASTRY-A. (2008). Powering MEMS portable devices — a review of non-regenerative and regenerative power supply systems with special emphasis on piezoelectric energy harvesting systems, *Smart Materials and Structures*, **17**(4), p. 043001(33pp). 1.2, 5.1

DE JONG-J., LAMMERTINK-R., AND WESSLING-M. (2006). Membranes and microfluidics: a review, *Lab on a Chip*, **6**, pp. 1125–1139. 1.1

DEL MAR HERSHENSON-M., MOHAN-S., BOYD-S., AND LEE-T. (1999). Optimization of inductor circuits via geometric programming, *Proc. of 36th Design Automation Conference*, pp. 994–998. 5.4.1

DEMIRCI-U. (2006). Acoustic picoliter droplets for emerging applications in semiconductor industry and biotechnology, *Journal of Microelectromechanical Systems*, **15**(4), pp. 957–966. 1.3.3, 4.1

DEVOE-D. (2002). Thermal issues in MEMS and microscale systems, *IEEE Transactions on Components and Packaging Technologies*, **25**(4), pp. 576–583. 1.2

DISSANAYAKE-D., AL-SARAWI-F., LU-T., AND ABBOTT-D. (2009). Finite element modelling of surface acoustic wave device based corrugated microdiaphragms, *Smart Materials and Structures*, **18**(9), p. 095030. 4.5, 6.2

DRAFTS-B. (2001). Acoustic wave technology sensors, *IEEE Transactions on Microwave Theory and Techniques*, **49**(4), pp. 795 – 802. 1.1.2

DUGGIRALA-R., AND LAL-A. (2005). A hybrid PZT-silicon microvalve, *Journal of Microelectromechanical Systems*, **14**(3), pp. 488–497. 1.1.1

EDDINGTON-D., AND BEEBE-D. (2004). Flow control with hydrogels, *Advanced Drug Delivery Reviews*, **56**(2), pp. 199–210. 1.2

FELTON-M. (2003). The new generation of microvalves, *Analytical Chemistry*, **75**(19), pp. 429 A–432 A. 1.1.1, 4.1

FINKENZELLER-K. (2003). *RFID Handbook: Fundamentals and Applications in Contactless Smart Cards and Identification*, Wiley 2nd edition. Ch. 12 and 13. 1.1.2

FRAMPTON-K., MINOR-K., AND MARTIN-S. (2004). Acoustic streaming in micro-scale cylindrical channels, *Applied Acoustics*, **65**(11), pp. 1121–1129. 1.3.3, 4.2.1

FRECKER-M. (2003). Recent advances in optimization of smart structures and actuators, *Journal of Intelligent Material Systems and Structures*, **14**(4-5), pp. 207–216. 1.1.1, 4.1

FU-C., RUMMLER-Z., AND SCHOMBURG-W. (2003). Magnetically driven micro ball valves fabricated by multilayer adhesive film bonding, *Journal of Micromechanics and Microengineering*, **13**(4), pp. S96–S102. 1.2

FU-Y. (2005). *Design of a Hybrid Magnetic and Piezoelectric Polymer Microactuator*, PhD thesis, Swinburne University of Technology. Ch. 1 and 2. 1.1.1

GABRIEL-S., LAU-R. W., AND GABRIEL-C. (1996). The dielectric properties of biological tissues: II. Measurements in the frequency range 10 Hz to 20 GHz, *Physics in Medicine and Biology*, **41**(11), pp. 2251–2269. 5.2.3

GALAMBOS-P., CZAPLEWSKI-D., GIVLER-R., POHL-K., LUCK-D., BENAVIDES-G., AND JOKIEL-B. (2008). Drop ejection utilizing sideways actuation of a MEMS piston, *Sensors and Actuators. A*, **141**(1), pp. 182–191. 4.4

GARDNER-J., VARADAN-V., AND AWADELKARIM-O. (2001). *Microsensors, MEMS, and Smart Devices*, John Wiley & Sons. Ch. 9 and 10. 1.1.2, 1.2, 2.1, 3.5

GEIPEL-A., DOLL-A., GOLDSCHMIDTBÖING-F., MÜLLER-B., JANTSCHEFF-P., ESSER-N., MASSING-U., AND WOIAS-P. (2006). Design of an implantable active microport system for patient specific drug release, *BioMed'06: Proceedings of the 24th IASTED International Conference on Biomedical Engineering*, pp. 161–166. 1.1, 4.1

GEIPEL-A., GOLDSCHMIDTBONG-F., DOLL-A., NADIR-S., JANTSCHEFF-P., ESSER-N., MASSING-U., AND WOIAS-P. (2007). An implantable active microport based on a self-priming high-performance two-stage micropump, *Proc. of Solid-State Sensors, Actuators and Microsystems Conference*, pp. 1943–1946. 1.2, 5.1

GOETTSCHE-T., KOHNLE-J., WILLMANN-M., ERNST-H., SPIETH-S., TISCHLER-R., MESSNER-S., ZENGERLE-R., AND SANDMAIER-H. (2005). Novel approaches to particle tolerant valves for use in drug delivery systems, *Sensors and Actuators A: Physical*, **118**(1), pp. 70–77. 1.1

GOMEZ-F. (2008). *Biological Applications of Microfluidics*, Wiley. Ch. 4, 22, and 23. 1.1, 4.1

GRAVESEN-P., BRANEBJERG-J., AND JENSEN-O. (1993). Microfluidics-a review, *Journal of Micromechanics and Microengineering*, **3**(4), pp. 168–182. 1.1

GRAYSON-A., SHAWGO-R., LI-Y., AND CIMA-M. (2004). Electronic MEMS for triggered delivery, *Advanced Drug Delivery Reviews*, **56**(2), pp. 173 – 184. 1.2, 5.1

HALL-S., AND HAO-Y. (2006). *Antennas and Propagation for Body-Centric Wireless Communications*, Artech House. Ch. 2,7, and 9. 5.2.2, 5.2.3, 5.2.3, 5.4.1, 5.5.2, 5.5.2

HARALDSSON-K. (2005). *Fabrication of Polymeric Microfluidic Devices via Photocurable Liquid Monomers*, PhD thesis, KTH - Royal Institute of Technology. Ch. 2. 1.1

HARTSGROVE-G., KRASZEWSKI-A., AND SUROWIEC-A. (1987). Simulated biological materials for electromagnetic radiation absorption studies, *Bioelectromagnetics*, **8**(1), pp. 29–36. 5.2.3

HASEGAWA-K., AND KOSHIBA-M. (2003). Coupled-mode equations for interdigital transducers for leaky surface acoustic waves, *Japanese Journal of Applied Physics*, **42**, pp. 3157–3160. 2.4.3

HASEGAWA-K., INAGAWA-K., AND KOSHIBA-M. (2001). Extraction of all coefficients of coupled-mode equations for natural, single phase by hybrid finite element method, *IEEE Trans. on Ultrasonics, Ferroelectrics, and Frequency Control*, **48**(5), pp. 1341–1350. 1.3, 1.3.1, 2.1, 2.4.2, 3.3.3

HASHIMOTO-K. (2000). *Surface Acoustic Wave Devices in Telecommunications Modelling and Simulation*, Springer. 1.1.2, 1.3.2, 3.3, 3.3.3

HASHIMOTO-K.-Y., KOSKELA-J., AND SALOMAA-M. (1999). Fast determination of coupling-of-modes parameters based on strip admittance approach, *Proc. of IEEE Ultrasonics Symposium*, Vol. 1, pp. 93–96. 1.3.1, 2.1

HASHIMOTO-K.-Y., TATSUYA-O., AND YAMAGUCHI-M. (2000). Analysis of SAW excitation and propagation under periodic metallic grating structures, *International Journal of High Speed Electronics and Systems*, **10**(3), pp. 685–734. 2.4.3

HENNING-A. (2006). Comprehensive model for thermopneumatic actuators and microvalves, *Journal of Microelectromechanical Systems*, **15**(5), pp. 1308–1318. 1.2

HESKETH-P., BINTORO-J., AND LUHARUKA-R. (2003). Microvalve for fuel cells and miniature gas chromatographic system, *Sensors Update*, **13**(1), pp. 233–302. 1.1.1, 4.1

HOFER-M., FINGER-N., KOVACS-G., SCHÖLMER-J., LANGER-U., AND LERCH-R. (2002). Finite element simulation of bulk and surface acoustic wave (SAW) interaction in SAW devices, *Proc. of IEEE Ultrasonics Symposium*, pp. 53–56. 1.3.1, 1.3.2, 2.1, 2.4.5, 2.5.2, 2.8, 3.1

HOFER-M., FINGER-N., KOVACS-G., SCHöLMER-J., ZAGLMAYR-S., LANGER-U., AND LERCH-R. (2006). Finite-element simulation of wave propagation in periodic piezoelectric SAW structures, *IEEE Transactions on Ultrasonics, Ferroelectrics, and Frequency Control*, **53**(6), pp. 1192–1201. 2.4.5, 2.6.2, 2.7, 3.1, 3.3.3

IEEE standard for safety levels with respect to human exposure to radio frequency electromagnetic fields, 3 kHz to 300 GHz (1999). *IEEE Std C95.1991*. 5.2.2, 5.1

IPPOLITO-S., KALANTAR-ZADEH-K., POWELL-D., AND WLODARSKI-W. (2003). A 3-dimensional finite element approach for simulating acoustic wave propagation in layered SAW devices, *Proc. of IEEE Ultrasonics Symposium*, pp. 303–306. 3.1, 3.3.3, 3.4.1

IRIARTE-G., ENGELMARK-F., KATARDJIEV-I., PLESSKY-V., AND YANTCHEV-V. (2003). SAW COM-parameter extraction in AlN/diamond layered structures, *IEEE Trans. on Ultrasonics, Ferroelectrics, and Frequency Control*, **50**(11), pp. 1542–1547. 2.4.1

IZDEBSKI-P., RAJAGOPALAN-H., AND RAHMAT-SAMII-Y. (2009). Conformal ingestible capsule antenna: A novel chandelier meandered design, *IEEE Transactions on Antennas and Propagation*, **57**(4), pp. 900–909. 5.2.3, 5.4.3

JOHANSSON-A. (2004). *Wireless Communication with Medical Implants: Antennas and Propagation*, PhD thesis, Lunds Universitet. Ch. 5. 5.2.3

JOVANOV-E., AND RASKOVIC-D. (2006). Wireless intelligent sensors, *M-Health Emerging Mobile Health Systems*, **1**, pp. 33–49. 1.3.4

KAAJAKARI-V., SATHAYE-A., AND LAL-A. (2001). A frequency addressable ultrasonic microfluidic actuator array, *Proc. of 11th International Conference on Solid State Sensors and Actuators Transducers01/Eurosensors XV*, pp. 958–961. 4.5, 5.5.2

KANNAN-T. (2006). *Finite element analysis of surface acoustic wave resonators*, Master's thesis, University of Saskatchewan. Ch. 3 and 4. 2.6.1

KEMP-J. (2002). *Theoretical and experimental study of wave propagation in brass musical instruments*, PhD thesis, University of Edinburgh. Ch. 2 and 3. 3.2.1

KIM-J., AND RAHAMAT-SAMII-Y. (2006). Planar inverted-F antennas on implantable medical devices: Meandered type versus spiral type, *Microwave and Optical Technology Letters*, **48**(3), pp. 567–572. 1.3.4, 5.4

KINO-G. (1987). *Acoustic Waves Devices, Imaging & Analog Signal Processing*, Prentice-Hall. Ch. 2. 3.3.1

KOHL-M., DITTMANN-D., QUANDT-E., AND WINZEK-B. (2000). Thin film shape memory microvalves with adjustable operation temperature, *Sensors and Actuators A: Physical*, **83**(1-3), pp. 214–219. 1.2

KONDOH-J., SHIMIZU-N., MATSUI-Y., AND SHIOKAWA-S. (2005). Liquid heating effects by saw streaming on the piezoelectric substrate, *IEEE Trans. on Ultrasonics, Ferroelectrics, and Frequency Control*, **52**(10), pp. 1881–1883. 4.2.1

KONDRATIEV-S., THORVALDSSON-T., SAKHAROV-S., BUZANOV-O., AND MEDVEDEV-A. (2001). Extraction of COM parameters on langasite substrates and the application to design of a SAW filter, *Proc. of IEEE Ultrasonics Symposium*, Vol. 1, pp. 53–56. 2.1, 2.4.1, 2.5

KOSHIBA-M., SHICHISHIMA-N., OHBUCHI-K., AND TSUJI-Y. (1997). Software for a multilayered surface acoustic wave device based on the finite element method and coupling-of-modes theory, *Japanese Journal of Applied Physics*, **36**, pp. 3060–3063. 2.4.5

KOSINSKI-J. (2000). New piezoelectric substrates for SAW devices, *Journal of High Speed Electronics and Systems*, **10**(4), pp. 1017–1068. 1.1.2, 3.2

KOSKELA-J., PLESSKY-V., AND SALOMAA-M. (1999). SAW/LSAW COM parameter extraction from computer experiments with harmonic admittance of a periodic array of electrodes, *IEEE Trans. on Ultrasonics, Ferroelectrics, and Frequency Control*, **46**(4), pp. 806–816. 2.1, 2.4.4, 2.7

LAI-Z. (2007). *Finite element analysis of electrostatic coupled systems using geometrically nonlinear mixed assumed stress finite elements*, Master's thesis, University of Pretoria. Ch. 4. 4.3.3

LAUDE-V., REINHARDT-A., WILM-M., KHELIF-A., AND BALLANDRAS-S. (2004). Fast FEM/BEM simulation of SAW devices via asymptotic waveform evaluation, *IEEE Trans. on Ultrasonics, Ferroelectrics, and Frequency Control*, **51**(3), pp. 359–363. 2.4.4

LAUD-V., AND BALLANDRAS-S. (2003). Slowness curves and characteristics of surface acoustic waves propagating obliquely in periodic finite-thickness electrode gratings, *Japanese Journal of Applied Physics*, **93**, pp. 10084–10088. 2.4.4

LE BRIZOUAL-L., SARRY-F., MOREIRA-F., AND ELMAZRIA-O. (2006). FEM modelling of surface acoustic wave in diamond layered structure, *Physica Status Solidi (a)*, **203**, pp. 3179–3184. 2.4.5, 3.1

LEE-Y., LEE-S., AND ROH-Y. (2002). Design of withdrawal-weighted SAW filters, *IEEE Trans. on Ultrasonics, Ferroelectrics, and Frequency Control*, **49**(3), pp. 337–344. 1.3.2, 3.1

LEHTONEN-S., PLESSKY-V., AND SALOMAA-M. (2004). Short reflectors operating at the fundamental and second harmonics on 128° $LiNbO_3$, *IEEE Trans. on Ultrasonics, Ferroelectrics, and Frequency Control*, **51**(3), pp. 343–351. 3.6.1

LIM-Y.-H. (2003). Finite-element simulation of closed loop vibration control of a smart plate under transient loading, *Smart Materials and Structures*, **22**, pp. 272–286. 3.3.3

LI-P., SHIH-J., LO-R., ADAM-B., AGARWAL-R., AND SAATI-S. (2007a). An electrochemical intraocular drug delivery device, *Proc. of 20th IEEE International Conference on Micro Electro Mechanical Systems*, pp. 15–18. 1.2, 5.1

LI-T., ZHENG, L. LIU-T., AND HU-H. (2008). Design and analysis of a novel wireless passive microsensor based on the SAW theory, *Proc. of 2nd International Conference on Sensor Technologies and Applications*, pp. 407–412. 1.3.1, 2.1

LIU-C., AND BAR-COHEN-Y. (1999). Scaling laws of microactuators and potential applications of electroactive polymers in MEMS, Vol. 3669, pp. 345–354. 1.1

LI-Y., YANG-M., LING-M., AND ZHU-Y. (2007b). Surface acoustic wave humidity sensors based on poly(p-diethynylbenzene) and sodium polysulfonesulfonate, *Sensors and Actuators. B*, **122**(2), pp. 560–563. 4.2

LOIZOU-P. (1999). Introduction to cochlear implants, *IEEE Engineering in Medicine and Biology Magazine*, **18**(1), pp. 32–42. 1.2, 5.1

LU-H., GOLDSMITH-C., CAULLER-L., AND LEE-J. (2007). MEMS-Based inductively coupled RFID transponder for implantable wireless sensor applications, *IEEE Trans. on Magnetics*, **43**(6), pp. 2412–2414. 1.3.4, 5.1

LUO-C.-P. (2004). *Detection of antibody-antigen reactions using surface acoustic wave and electrochemical immunosensors*, PhD thesis, Ruperto-Carola University of Heidelberg. Ch. 4 and 6. 4.2, 5.2.1

MAKKONEN-T., PLESSKY-V., GRIGORIEVSKI-V., KOPP-L., SOLAL-M., STEICHEN-W., AND SALOMAA-M. (2002). FEM/BEM simulation and experimental study of LLSAW resonator characteristics on YZ-$LiNbO_3$, *Proc. of IEEE Ultrasonics Symposium*, Vol. 1, pp. 317–320. 2.4.4

MAKKONEN-T., PLESSKY-V., STEICHEN-W., GRIGORIEVSKI-V., SOLAL-M., AND SALOMAA-M. (2006). Longitudinal leaky SAW resonators and filters on YZ-$LiNbO_3$, *IEEE Trans. on Ultrasonics, Ferroelectrics, and Frequency Control*, **53**, pp. 393–401. 1.3.2, 3.1

MALOCHA-D., PUCCIO-D., AND GALLAGHER-D. (2004). Orthogonal frequency coding for SAW device applications, *Proc. of IEEE Ultrasonics Symposium*, Vol. 2, pp. 1082–1085. 1.1, 3.1

MAMISHEV-A., SUNDARA-RAJAN-K., YANG-F., DU-Y., AND ZAHN-M. (2004). Interdigital sensors and transducers, *Proceedings of the IEEE*, Vol. 92, pp. 808–845. 1.1.2, 2.1

MATTHEWS-G. (2007). *Investigation of flexural plate wave devices for sensing applications in liquid media*, PhD thesis, RMIT University. Ch. 2, 5 and 6. 1.3, 1.3.2, 3.1

MERCANZINI-A., BACHMANN-M., JORDAN-A., AMSTUTZ-Y., AND DE ROOIJ, N. STERGIOPULOS-N. (2005). A low power, polyimide valved micropump for precision drug delivery, *Proc. of 3rd IEEE/EMBS Special Topic Conference on Microtechnology in Medicine and Biology*, pp. 146–149. 1.2, 5.1

MESSNER-S., SCHAIBLE-J., SANDMAIER-H., AND ZENGERLE-R. (2006). Three-way silicon microvalve for pneumatic applications with electrostatic actuation principle, *Microfluidics and Nanofluidics*, **2**(2), pp. 89–96. 1.1

MITSAKAKIS-K., TSEREPI-A., AND GIZELI-E. (2009). SAW device integrated with microfluidics for array-type biosensing, *Microelectronic Engineering*. 4.2

MOAVENI-S. (2007 (3^{rd} Edition)). *Finite Element Analysis: Theory and Applications with ANSYS*, Prentice Hall. Ch. 7, 13, 14, and 15. 3.3.3, 3.6.1, 4.3.3, 4.3.3

MOELLER-F., ENDERLEIN-J., BELKERDID-M., MALOCHA-D., AND BUFF-W. (1999). Direct sequence spread spectrum differential phase shift keying SAW correlator on GaAs, *IEEE Trans. on Ultrasonics, Ferroelectrics, and Frequency Control*, **46**(4), pp. 842–848. 1.1, 3.1

MOHAN-S., DEL MAR HERSHENSON-M., BOYD-S., AND LEE-T. (1999). Simple accurate expressions for planar spiral inductances, *IEEE Journal of Solid-State Circuits*, **34**(10), pp. 1419–1424. 5.4.1

MOKWA-W. (2007). Medical implants based on microsystems, *Measurement Science and Technology*, **18**(5), pp. R47–R57. 1.2, 5.1

NEAGU-C., JANSEN-H., SMITH-A., GARDENIERS-J., AND ELWENSPOEK-M. (1997). Characterization of a planar microcoil for implantable microsystems, *Sensors and Actuators A*, **62**(1-3), pp. 599–611. 1.3.4, 5.1

NGUYEN-N., HUANG-X., AND CHUAN-T. (2002). MEMS-Micropumps: A Review, *Journal of Fluids Engineering*, **124**(4), pp. 384–392. 1.1.1, 4.1

NGUYEN-N.-T., AND WERELEY-S. (2002). *Fundamentals and Applications of Microfluidics*, Artech House. Ch. 4, 6, 7, and 8. 1.1, 4.1

NGUYEN-N.-T., AND WHITE-R. (2000). Acoustic streaming in micromachined flexural plate wave devices: numerical simulation and experimental verification, *IEEE Trans. on Ultrasonics, Ferroelectrics, and Frequency Control*, **47**(6), pp. 1463–1471. 4.2.1

NOWICKI-A., SECOMSKI-W., TROTS-I., AND LITNIEWSKI-J. (2004). Extending penetration depth using coded ultrasonography, *Bulletin of the Polish Academy of Sciences Technical Sciences*. 3.2.1

OH-K., AND AHN-C. (2006). A review of microvalves, *Journal of Micromechanics and Microengineering*, **16**, pp. 13–39. 1.1.1, 1.1.1, 4.1

OH-K., RONG-R., AND AHN-C. (2005). Miniaturization of pinch-type valves and pumps for practical micro total analysis system integration, *Journal of Micromechanics and Microengineering*, **15**(12), pp. 2449–2455. 1.1

OHORI-T., SHOJI-S., MIURA-K., AND YOTSUMOTO-A. (1998). Partly disposable three-way microvalve for a medical micro total analysis system, *Sensors and Actuators A: Physical*, **64**(1), pp. 57–62. 1.1

OSEPCHUK-J., AND PETERSEN-R. (2001). Safety standards for exposure to RF electromagnetic fields, *IEEE Microwave Magazine*, **2**(2), pp. 57–69. 5.2.2, 5.2.3

OSTERMAYER-G. (2001). Correlative signal processing in wireless SAW sensor applications to provide multiple-access capability, *IEEE Transactions on Microwave Theory and Techniques*, **49**(4), pp. 809–816. 1.1, 3.1

PICCINI-M., AND TOWE-B. (2006). A shape memory alloy microvalve with flow sensing, *Sensors and Actuators A: Physical*, **128**(2), pp. 344–349. 1.2

PLESSKY-V., AND KOSKELA-J. (2000). Coupling-of-modes analysis of SAW devices, *International Journal of High Speed Electronics and Systems*, **10**(4), pp. 867–947. 2.2, 2.2, 2.2, 2.2, 2.3, 2.4, 2.4.4, 2.6.1, 2.8

POHL-A. (2000). A Review of Wireless SAW Sensors, *IEEE Trans. on Ultrasonics, Ferroelectrics, and Frequency Control*, **47**(2), pp. 317–332. 1.1.2, 2.1

POTKAY-J. (2008). Long term, implantable blood pressure monitoring systems , *Biomedical Microdevices*, **10**(3), pp. 379–392. 5.2.2

QI-Q., AND BRERETON-G. (1995). Mechanisms of removal of micron-sized particles by high-frequency ultrasonic waves, *IEEE Trans. on Ultrasonics, Ferroelectrics, and Frequency Control*, **42**(4), pp. 619 – 629. 4.2.1

Radiocommunications (Electromagnetic Radiation - Human Exposure) Standard (2003). Office of Legislative Drafting and Publishing (OLDP), http://www.comlaw.gov.au/comlaw/Legislation/LegislativeInstrumentCompilation1.nsf/0/064C496C9CABFCC6CA2572AD0009A681?OpenDocument. Last accessed: June, 2009. 5.2.3, 5.2.3

REINDL-L., SCHOLL-G., OSTERTAG-T., SCHERR-H., WOLFF-U., AND SCHMIDT-F. (1998). Theory and application of passive SAW radio transponders as sensors, *IEEE Transactions on Ultrasonics, Ferroelectrics, and Frequency Control*, **45**(5), pp. 1281–1292. 1.1.2, 1.1.2

RENAUDA-L., ARMENEANB-M., BERRYA-L., KLEIMANNA-P., MORINA-P., PITAVALA-M., OBRIENC-J., BRUNETC-M., AND SAINT-JALMES-H. (2002). Implantable planar RF microcoils for NMR microspectroscopy, *Sensors and Actuators A*, **99**(3), pp. 244–248. 1.3.4, 5.1

REYNAERTS-D., PEIRS-J., AND VAN BRUSSEL-H. (1997). An implantable drug-delivery system based on shape memory alloy micro-actuation, *Sensors and Actuators A: Physical*, **61**(1-3), pp. 455–462. 1.1

RICH-C., AND WISE-K. (2003). A high-flow thermopneumatic microvalve with improved efficiency and integrated state sensing, *Journal of Microelectromechanical Systems*, **12**(2), pp. 201–208. 1.2

RIFE-J., BELL-M., HORWITZ-J., KABLER-R., AUYEUNG-R., AND KIM-J. (2000). Miniature valveless ultrasonic pumps and mixers, *Sensors and Actuators. A*. 4.2.1

ROBERT-P., SAIAS-D., BILLARD-C., BORET-S., SILLON-N., MAEDER-PACHURKA-C., CHARVET-P., BOUCHE-G., ANCEY-P., AND BERRUYER-P. (2003). Integrated RF-MEMS switch based on a combination of thermal and electrostatic actuation, *Proc. of 12th International Conference on TRANSDUCERS, Solid-State Sensors, Actuators and Microsystems*, Vol. 2, pp. 1714–1717. 1.1.1

ROBERTS-D., LI-H., STEYN-J., YAGLIOGLU-O., SPEARING-S., SCHMIDT-M., AND HAGOOD-N. (2003). A piezoelectric microvalve for compact high-frequency, high-differential pressure hydraulic micropumping systems, *Journal of Microelectromechanical Systems*, **12**(1), pp. 81–92. 1.2

ROSLER-U., COHRS-D., DIETZ-A., FISCHERAUER-G., RUILE-W., RUSSER-P., AND WEIGEL-R. (1995). Determination of leaky SAW propagation, reflection and coupling on $LiTaO_3$, *Proc. of IEEE Ultrasonics Symposium*, Vol. 1, pp. 247–250. 1.3.1, 2.4.5

RUSSOLD-M., AND JARVIS-J. (2007). Implantable stimulator featuring multiple programs, adjustable stimulation amplitude and bi-directional communication for implantation in mice, *Proc. of World Congress on Medical Physics and Biomedical Engineering*, Vol. 14, pp. 618–621. 1.2, 5.1

SAKONG-J., ROH-Y., AND ROH-H. (2006). Saw sensor system with micro-fluidic channels to detect dna molecules, *Proc. of IEEE Ultrasonics Synposium*, pp. 548–551. 4.2

SANKARANARAYANAN-S., BHETHANABOTLA-V., AND JOSEPH-B. (2007). Finite element modeling of hexagonal surface acoustic wave device in $LiNbO_3$, *Proc. of IEEE Sensors*, pp. 353–356. 1.3, 1.3.2, 3.1, 3.3.3

SATO-R., AND SHINRIKI-M. (2000). Time sidelobe reduction technique for binary phase coded pulsecompression, *Proc. of IEEE International Radar Conference*, pp. 809–814. 3.2.1

SCHMIDT-F., AND SCHOLL-G. (2000). Wireless SAW identification and sensor systems, *International Journal of High Speed Electronics and Systems*, **10**(4), pp. 1143–1191. 3.1

SCHOLL-G., KORDEN-C., RIHA-E., RUPPEL-C., WOLFF-U., RIHA-G., REINDL-L., AND WEIGEL-R. (2003). SAW-based radio sensor systems for short-range applications, *IEEE Microwave Magazine*, **4**(4), pp. 68–76. 1.1.2

SIMONS-R., AND MIRANDA-F. (2006). Modeling of the near field coupling between an external loop and an implantable spiral chip antenna in biosensor systems, *Proc. of IEEE Antennas and Propagation Society International Symposium*, pp. 1099–1102. 5.5.2

SI-P., HU-A., MALPAS-S., AND BUDGETT-D. (2008). A frequency control method for regulating wireless power to implantable devices, *IEEE Trans. on Biomedical Circuits and Systems*, **2**(1), pp. 22–29. 1.3.4, 5.1

SOLAL-M., ABBOUD-T., BALLANDRAS-S., CHAMALY1-S., LAUDE-V., LARDAT-R., PASTUREAUD-T., RIBBE-J., STEICHEN-W., AND VENTURA-P. (2004). FEM/BEM analysis for SAW devices, *Proc. of 2nd International Symposium on Acoustic Wave Devices for Future Mobile Communication Systems*, pp. 185–202. 2.1

SOLAL-M., LAUDE-V., AND BALLANDRAS-S. (2003). A P-matrix-based model for the analysis of SAW transversely coupled resonator filters, including guided modes and a continuum of radiated waves, *IEEE Trans. on Ultrasonics, Ferroelectrics, and Frequency Control*, **50**(12), pp. 1729–1741. 1.3.1, 2.1

SONG-F., HUANG-G., KIM-J., AND HARAN-S. (2008). On the study of surface wave propagation in concrete structures using a piezoelectric actuator/sensor system, *Smart Materials and Structures*, **17**(5), p. 055024 (8pp). 3.3.3, 3.4.2

SOONTORNPIPIT-P., FURSE-M., AND CHUNG-Y. (2004). Design of implantable microstrip antenna for communication with medical implants, *IEEE Trans. on Microwave Theory and Techniques*, **52**(8), pp. 1944–1951. 5.4.3

SOUNART-T., MICHALSKE-T., AND ZAVADIL-K. (2005). Frequency-dependent electrostatic actuation in microfluidic MEMS, *Journal of Microelectromechanical Systems*, **14**(1), pp. 125–133. 1.1.1, 4.3.3

SPRINGER-A., WEIGEL-R., POHL-A., AND SEIFERT-F. (1999). Wireless identification and sensing using surface acoustic wave devices, *Mechatronics*, **9**(7), pp. 745–756. 1.1.2

STELZER-A., SCHEIBLHOFER-S., SCHUSTER-S., AND TEICHMANN-R. (2008). Wireless sensor marking and temperature measurement with SAW-identification tags, *Measurment*, **41**(5), pp. 579–588. 1.1.2

STELZER-A., SCHUSTER-S., AND SCHEIBLHOFER-S. (2004). Readout unit for wireless SAW sensors and ID-tags, *Proc. of 2nd International Symposium on Acoustic Wave Devices for Future Mobile Communication Systems*, pp. 37–44. 1.1.2

STROBL-C., VON GUTTENBERG-Z., AND WIXFORTH-A. (2004). Nano- and pico-dispensing of fluids on planar substrates using SAW, *IEEE Trans. on Ultrasonics, Ferroelectrics, and Frequency Control*, **51**(11), pp. 1432–1436. 4.2.1

SUTANTO-J., HESKETH-P., AND BERTHELOT-Y. (2006). Design, microfabrication and testing of a CMOS compatible bistable electromagnetic microvalve with latching/unlatching mechanism on a single wafer, *Journal of Micromechanics and Microengineering*, **16**(2), pp. 266–275. 1.2

TAKEUCHI-Y., AND YAMANOUCHI-K. (1995). A low loss SAW matched filter using unidirectional transducers under the compensation method of temperature deviations, *Proc. of IEEE Ultrasonics Symposium*, Vol. 1, pp. 7–12. 3.1

THEODORIDIS-M., AND MOLLOV-S. (2005). Distant energy transfer for artificial human implants, *IEEE Trans. on Biomedical Engineering*, **52**(11), pp. 1931–1938. 1.3.4, 5.4

THIELE-J., AND DA CUNHA-M. (2003). High temperature SAW gas sensor on langasite, *Proc. of IEEE Sensors*, Vol. 2, pp. 769–772. 4.2

THIELICKE-E., AND OBERMEIER-E. (2000). Microactuators and their technologies, *Mechatronics*, **10**(4-5), pp. 431 – 455. 1.1, 1.1.1

THOMA-C. (1999). Fast COM parameter extraction from theoretically derived dispersion relations for SAWs propagating in periodic metallic gratings, *Proc. of IEEE Ultrasonics Symposium*, Vol. 1, pp. 151–154. 1.3.1, 2.1

VAN DER WIJNGAART-W., ASK-H., ENOKSSON-P., AND STEMME-G. (2002). A high-stroke, high-pressure electrostatic actuator for valve applications, *Sensors and Actuators A: Physical*, **100**(2-3), pp. 264–271. 1.2

VENTURA-P., HODE-J., SOLAL-M., DESBOIS-J., AND RIBBE-J. (1998). Numerical methods for SAW propagation characterization, *Proc. of IEEE Ultrasonics Symposium*, pp. 175–186. 1.3.1, 2.1

VERGARA-A., LLOBET-E., RAMIREZ-J., IVANOVA-P., FONSECA-L., ZAMPOLLI-S., SCORZONI-A., BECKER-T., MARCOE-S., AND WOLLENSTEIN-S. (2007). An RFID reader with onboard sensing capability for monitoring fruit quality, *Sensors and Actuators B*, **127**, pp. 143–149. 1.3.4, 5.1

WAGNER-J., AND VON SCHICKFUS-M. (2001). Inductively coupled, polymer coated surface acoustic wave sensor for organic vapors, *Sensors and Actuators B*, **76**(1-3), pp. 58–63. 5.2.1

WANG-C., STIELAU-O., AND COVIC-G. (2000). Load models and their application in the design of loosely coupled inductive power transfer systems, *Proc. of International Conference on Power System Technology*, Vol. 2, pp. 1053–1058. 5.5.2

WANG-G., LIU-W., BASHIRULLAH-R., SIVAPRAKASAM-M., KENDIR-G., JI-Y., HUMAYUN-M., AND WEILAND-J. (2004). A closed loop transcutaneous power transfer system for implantable devices with enhanced stability, *Proc. of International Symposium on Circuits and Systems*, Vol. 4, pp. IV–17–20. 1.3.4, 5.1

WANG-W., HE-S., LI-S., AND PAN-Y. (2006). High frequency stability oscillator for surface acoustic wave-based gas sensor, *Smart Materials and Structures*, **15**(6), pp. 1525–1530. 2.8

WANG-W., LEE-K., WOO-I., PARK-I., AND YANG-S. (2007). Optimal design on SAW sensor for wireless pressure measurement based on reflective delayline, *Sensors and Actuators. A*, **139**, pp. 2–6. 1.3.1, 2.1

WANG-Z., CHEEKE-J., AND JEN-C. (1996). Perturbation method for analyzing mass sensitivity of planar multilayer acoustic sensors, *IEEE Trans. on Ultrasonics, Ferroelectrics, and Frequency Control*, **43**(5), pp. 844–851. 2.4.2

WHITESIDES-G. (2006). The origins and the future of microfluidics, *Nature*, **442**, pp. 368–373. 1.1

WIXFORTH-A. (2004). Acoustically driven planar microfluidics, *Superlattices and Microstructures*. 1.3.3, 4.1, 4.2.1, 4.2.1

WU-D., AND CHEN-H. (2005). Application of taguchi robust design method to SAW mass sensing device, *IEEE Trans. on Ultrasonics, Ferroelectrics, and Frequency Control*, **52**(12), pp. 2403–2410. 3.1

XU-G. (2000). Finite element analysis of second order effects on the frequency response of a SAW device, *Proc. of IEEE Ultrasonics Symposium*, pp. 187–190. 1.3, 1.3.1, 1.3.2, 2.1, 3.1, 3.3.3, 3.3.3, 3.4.1

YANG-E.-H., LEE-C., MUELLER-J., AND GEORGE-T. (2004). Leak-tight piezoelectric microvalve for high-pressure gas micropropulsion, *Journal of Microelectromechanical Systems*, **13**(5), pp. 799–807. 1.1

YOBAS-L., DURAND-D., SKEBE-G., LISY-F., AND HUFF-M. (2003). A novel integrable microvalve for refreshable Braille display system, *Journal of Microelectromechanical Systems*, **12**(3), pp. 252–263. 1.1

YONG-Y.-K. (2001). Analysis of periodic structures for BAW and SAW resonators, *Proc. of IEEE Ultrasonics Symposium*, Vol. 1, pp. 781–790. 1.3.1, 2.1, 2.4.5, 2.5.1, 2.5.2, 2.6.1, 3.4.2

YU-H., KWON-J., AND KIM-E. (2006). Microfluidic mixer and transporter based on PZT self-focusing acoustic transducers, *IEEE Trans. on Ultrasonics, Ferroelectrics, and Frequency Control*, **15**(4), pp. 1015–1024. 1.3.3, 4.2.1

YU-S. (2004). Simulation of surface acoustic wave devices, *IEEE Trans. on Ultrasonics, Ferroelectrics, and Frequency Control*, **51**(5), pp. 616–623. 1.3.2, 3.1, 3.3.2

ZHAO-H., STANLEY-K., WU-J., AND CZYZEWSKA-E. (2005). Structure and characterization of a planar normally closed bulk-micromachined piezoelectric valve for fuel cell applications, *Sensors and Actuators A: Physical*, **120**(1), pp. 134–141. 1.2

This page is blank

Index

This page is blank

Résumé

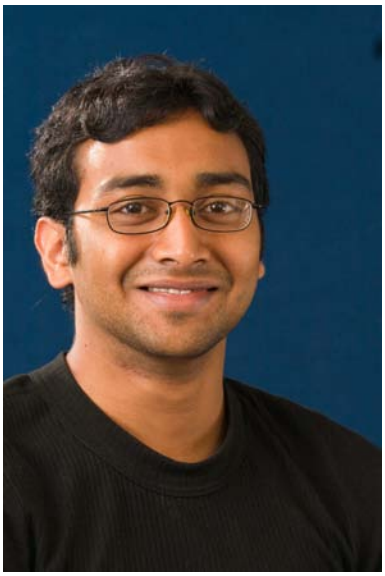

Ajay Tikka graduated from JNT University (India) with a Bachelor of Technology (Electronics & communication Engineering) in 2003. Later, he has completed Master of Engineering (Microelectronic Engineering) and Master of Engineering Science in Computer and Microelectronic Engineering from RMIT University and Victoria University in 2004 and 2005, respectively. He commenced his PhD on June, 2006 at The University of Adelaide under the supervision of Dr. Said Al-Sarawi (Centre for High Performance Integrated Technologies and Systems) and Professors Derek Abbott (The Centre for Biomedical Engineering).

In 2006 he was awarded a Divisional Scholarship to undertake research on the Australian Research Council (ARC) Discovery sponsored multi-disciplinary project, "RF Controlled microvalve for biomedical applications". He has authored and co-authored 13 peer-reviewed publications and given more than ten conference presentations, including an invited presentation on "Passive Wireless Sensors and Actuators" at the Defence Science and Technology Organisation, Australia. He also paid a visit to The High Density Electronics Centre (HiDEC), University of Arkansas, USA to interact with Professor. Vijay K. Varadan's research group in 2008.

Ajay Tikka is a member of SPIE, Australian Health & Medical Research Congress (AHMRC), and Australian Microscopy & Microanalysis Research Facility (AMMRF). His research interests include smart structures and RF systems.

This page is blank

Ajay Tikka's Scientific Genealogy